

2010

A FEEDBACK-BASED DYNAMIC INSTRUMENT FOR MEASURING THE MECHANICAL PROPERTIES OF SOFT TISSUES

Morteza Heydari Araghi

Follow this and additional works at: <https://ir.lib.uwo.ca/digitizedtheses>

Recommended Citation

Araghi, Morteza Heydari, "A FEEDBACK-BASED DYNAMIC INSTRUMENT FOR MEASURING THE MECHANICAL PROPERTIES OF SOFT TISSUES" (2010). *Digitized Theses*. 3679.
<https://ir.lib.uwo.ca/digitizedtheses/3679>

This Thesis is brought to you for free and open access by the Digitized Special Collections at Scholarship@Western. It has been accepted for inclusion in Digitized Theses by an authorized administrator of Scholarship@Western. For more information, please contact wlsadmin@uwo.ca.

**A FEEDBACK-BASED DYNAMIC INSTRUMENT FOR MEASURING
THE MECHANICAL PROPERTIES OF SOFT TISSUES**

(Spine title: An Instrument for Measuring Soft Tissue Properties)

(Thesis format: Monograph)

by

Morteza Heydari Araghi



**Faculty of Engineering
Department of Electrical and Computer Engineering**

**Submitted in partial fulfillment
of the requirements for the degree of
Master of Engineering Science**

**School of Graduate and Postdoctoral Studies
The University of Western Ontario
London, Ontario, Canada**

© Morteza Heydari Araghi 2010

Abstract

In this paper, a novel feedback-based dynamic instrument integrated into a Minimally-Invasive-Surgery (MIS) tool to evaluate the mechanical impedance of soft tissues is presented. This instrument is capable of measuring viscoelasticity of tissues if specific boundary conditions are known. Some important advantages of the proposed instrument are that it is robust and simple in comparison to other similar instruments as it does not require magnitude information of plant's displacement output and no force sensor is used. The precision and accuracy of the measurements of the proposed instrument for soft tissues is noticeably higher than similar instruments, which are not optimized to work with soft tissues.

The proposed dynamic instrument is designed to detect the frequency shifts caused by contacting a soft tissue using an improved phase-locked loop feedback system (closed loop). These frequency shifts can then be used to evaluate the mechanical properties of the tissue. The closed-loop method works fast (with an approximate resonance-frequency-shift rate of 15 Hz per second), and is capable of measuring dynamic mechanical properties of viscoelastic tissues, while previous focus was mostly on static/quasi-static elastic modulus.

The instrument is used to evaluate the equivalent stiffness of several springs and cantilever beams, mass of reference samples, and also the frequency shifts of several phantoms with injected tumors, noting that these frequency shifts can be used to measure the viscoelasticity of the tissues. It is also shown that the instrument can be used for tumor localization in these phantoms.

KEYWORDS: Soft tissue tactile sensing, resonator, phase-locked loop, viscoelasticity measurement

Acknowledgements

First and foremost, it is a pleasure for me to thank my supervisor, Prof. Shaun Salisbury, who supported me throughout my thesis with his patience, knowledge and sparkling ideas while allowing me the room to work in my own way. One simply could not wish for a better or friendlier supervisor.

I would like to thank many people who directly or indirectly helped me throughout my Masters as my teachers, Mehrdad R. Kermani, Kenneth McIsaac, Micheal D. Naish, and my colleague, Khaled el Bannan, also the professors at Amirkabir University of Technology who taught me a lot, and many fellow students.

Special thanks to all my friends who made life pleasant to me and also helped me professionally, Reza Parseh, Mohammad Mohammadian, Farzad Hessar, Mansoor Alghooneh, Amir Beygi, Hassan Nikopour, Arash Hariri, and many others.

Lastly, and most importantly, I wish to thank my parents, Manijeh and Mohammad, who raised me, supported me, and taught me, and loved me, and my brother, Mojtaba. I dedicate this thesis to them.

Contents

Certificate of Examination	ii
Abstract	iii
Acknowledgements	iv
Contents	v
List of Tables	viii
List of Figures	ix
Nomenclature	xii
1 Introduction	1
1.1 Motivation	1
1.2 Techniques for measuring soft tissue mechanical characteristics	3
1.2.1 Palpation	4
1.2.2 Imaging techniques	4
1.2.3 Tactile sensors	5
1.2.3.1 Graspers	6
1.2.3.2 Indenters	7
1.2.3.3 Stress-strain based sensors	7
1.2.3.4 Resonators	10
1.2.3.5 Free-form vs. robotic measurement	14
1.3 The proposed instrument	15
1.4 Contributions	16
2 Mechanical system design	18
2.1 Principles	18

2.1.1	Principles of viscoelastic materials	18
2.1.2	Basic tissue models	21
2.1.3	Resonance frequency shift of a mechanical impedance	23
2.2	Instrument layout	25
2.3	Transducer selection	26
2.3.1	Displacement sensors	26
2.3.2	System actuator	29
2.3.2.1	Piezo stack actuators	31
2.3.2.2	Piezo bending actuators	32
2.3.2.3	Piezoelectric tubes	32
2.3.2.4	Amplified piezoelectric actuators	32
3	System modeling and optimization	34
3.1	State-space modeling	34
3.1.1	Piezoelectric stack actuator modeling	34
3.1.2	Non-contact setup	35
3.1.3	In-contact with a VMM model with mass	36
3.1.4	In-contact with a SLS model	37
3.1.5	In-contact with other tissue models	38
3.1.6	Discretization	39
3.2	Parametric model analysis	39
3.3	Numerical considerations	44
3.3.1	Nominal tissue/phantom parameters	44
3.3.2	Numerical model analysis & system parameters optimization	47
3.3.3	Estimation of the viscous damping	48
3.3.4	Actuator and sensor selection	51
4	Frequency Shift Detection	53
5	Simulation	62
5.1	Finite element analysis	62
5.1.1	Semi-infinite media	62
5.1.2	Indentation of a semi-infinite medium	65
5.2	Lumped parameter system simulation	67
5.2.1	Open-loop instrument	68
5.2.2	Linear and nonlinear phased-locked loop	68
5.2.3	Linear and nonlinear PLL-based feedback system	72

5.2.4	Nonlinear instrument and linear time-varying tissue	75
5.2.5	Tissue dynamic contact as a nonlinear behaviour	79
5.2.6	Stiffness follows a periodic pattern	79
6	Experimental Results	83
6.1	The instrument setup	83
6.1.1	Mechanical setup	83
6.1.2	Control and monitoring	85
6.2	Non-contact instrument	85
6.3	Validation	86
6.3.1	Validation of mass measurements	86
6.3.2	Validation of stiffness measurements	86
6.4	Testing on springs & system response analysis	91
6.5	Testing on gels & tumor localization	92
7	Conclusion and future work	95
	Bibliography	98
	Vita	109

List of Tables

2.1	Simple soft tissue models	22
2.2	Summary of non-contact displacement sensors	28
2.3	Summary of linear actuators	30
3.1	Damping ratio results for 20 experiments	51
5.1	Formulation of E for Indentation to semi-infinite bodies	64
5.2	Comparison of κ values for $\nu = 0.5$ obtained by the present model and the data of Ming et al [1].	66
6.1	Experimental validation of mass measurements	86
6.2	Experimental validation of stiffness measurement using cantilever beams	89
6.3	Measured rate (in N/m) of different springs	92
6.4	Measured Δf_r (in Hz) for a phantom with an injected tumor	93
6.5	Results for different areas of the gelatin-based phantom	93

List of Figures

1.1	Low-frequency resonance mechanical resonator	13
2.1	(Left) Storage modulus of a SLS material (Right) Loss modulus of a SLS material	23
2.2	Design layout for MIS instrument	26
3.1	Lumped-parameter system model	36
3.2	Plot of the components of the complex modulus of a generic SLS model versus ωT . E_1 , E_2 , and T are tissue parameters [2].	38
3.3	Simulation procedure for generic tissue models	39
3.4	Contours of Δf_{r1} (Hz) with respect to the instrument's mass and spring parameters.	49
3.5	Plots of Δf_r with respect to parameters of a mechanical impedance load.	50
4.1	Block diagram of a PLL system.	54
4.2	Output of an XOR gate.	56
4.3	Calculating the phase difference of the plant's input/output.	57
4.4	A nonlinear PLL-based feedback system for the proposed MIS instrument	61
4.5	A simplified and linearized system model for the instrument	61
5.1	Mechanical simulations of applying an indenter on a soft viscoelastic tissue: (a) a cylindrical indenter (b) A cylindrical indenter with a surrounding ring (c) A spherical indenter (d) A spherical indenter with a rounded ring. (both structured and non-structured (shown here) tissue samples have been employed)	66
5.2	Response of the system (x_1 and x_2 measured in μm for a highly damped system) to sinusoidal input voltage. Sample the time-domain response applying a sinusoidal with a frequency equal to the first resonance frequency.	69

5.3	Bode plot of the system outputs with/without contacting a material with a mechanical impedance of $k_m = 70\text{N/m}$, $c_m = 0.5\text{N}\cdot\text{s/m}$ and $m_m = 0.02\text{g}$	69
5.4	linear frequency shift output response to a step input phase change.	70
5.5	Nonlinear generic PLL system.	71
5.6	Linear (top) and nonlinear (bottom) frequency shift output response to a step input frequency change.	71
5.7	The critical area of the Rootlocus diagram for the linear system.	72
5.8	An overview of a PLL-based feedback system with a simplified instrument model as a constant.	73
5.9	An overview of a PLL-based feedback system with a simplified instrument model as a constant and ignoring the integration component from both inputs.	73
5.10	A linearized PLL-based feedback system with a simplified instrument model as a constant.	74
5.11	Step response of nonlinear and linear PLL-based feedback systems.	74
5.12	PLL-based detection of the first and second Δf_r in simulation while changing k_m up to 70N/m	76
5.13	PLL-based detection of the first and second Δf_r in simulation while changing m_m up to 0.2g	77
5.14	PLL-based detection of the first and second Δf_r in simulation while changing c_m up to $0.2\text{N}\cdot\text{s/m}$	78
5.15	The x_2 output of the instrument in-contact with a nonlinear tissue when a sinusoidal input is applied to the actuator. (left) response when working at a frequency far enough from the resonance. (right) response when working at resonance.	80
5.16	Frequency shift detection error for a periodic tissue stiffness value. (Left) full view (right) zoomed-in	82
6.1	Instrument setup: (a) the proposed instrument (b) the stand used for the experiments (c) performing an experiment by hand (d) sample under experiment (e) the sample, the tip, and the surrounding ring are shown (f) conditioning modules	84
6.2	Experimental validation of mass measurements	87
6.3	Experimental validation of stiffness measurement using cantilever beams	90

6.4	Experimental frequency response of the system outputs with/without contacting a spring	91
6.5	A gelatin phantom for tumor localization	94
6.6	A sample experiment on a soft rubber phantom with an injected tumor	94

List of Acronyms

δ	Loss angle
η	Newtonian viscosity (Pa.s)
κ_0, κ_1	Nonlinear correction factor for semi-infinite material correlation.
ν	Poisson's ratio
ω	Angular frequency (rad/s)
ρ	Density
ρ_l	Mass per length of cantilever
ρ_v	Density
σ	Stress (Pa)
Δf_r	Resonance frequency shift (Hz)
$\Delta \omega_r$	Resonance frequency shift (rad/s)
ε	Strain
ε^σ	Piezoelectric permittivity matrix
ζ	Damping ratio
A	The in-contact state-space model matrix
a	Radius of the indenter tip
A_0, B_0	Matrices representing the non-contact instrument
B	Bulk modulus

c	Viscous damping coefficient (N.s/m)
c_m	Damping factor of the tissue (n.s/m)
c_p	Damping factor of the piezo cactuatoer (N.s/m)
E'	Storage modulus (Pa)
E''	Loss modulus (Pa)
E^*	Dynamic modulus (Pa)
f_{n_i}	i-th natural frequency of the system
F_{p0}	Piezo actuator block force (N)
f_r	Resonance frequency (Hz)
G^*, G', G''	Shear modulus parameters
h	Thickness of the sample
I	Area moment of inertia
k_b	Stiffness od a cantilever beam (N/m)
k_p	Stiffness of the piezo cactuatoer (N/m)
k_m	Stiffness of the tissue
L	Length of cantilever
m_b	mass of a cantilever beam
m_p	Effective tip mass of the piezo cactuatoer (kg)
m_m	Effective tip mass of the tissue
N_p, α, β	Piezo actuator parameters
Q	Quality factor
s_E	Piezoelectric compliance matrix
T	Thickness of cantilever
V_{pm}	Maximum voltage of piezo actuator (V)

W	Width of cantilever
Z_0, Z_m	Mechanical impedance of the instrument and the material respectively
AM	Amplitude Modulation
FFT	Fast Fourier Transform
FM	Frequency Modulation
LC	Loop Controller
LVDT	Linear Variable Differential Transformer
MIS	Minimally-Invasive Surgery
MRE	Magnetic Resonance Elastography
PD	Phase Difference Block
PLL	Phase-locked loop
SD	Standard Deviation
SLS	Standard linear solid material
TRD	Torsional Resonator Device
VCO	Voltage-Controlled Oscillator
VM	Voigt model
VMM	Voigt model with mass, or a mechanical impedance

Chapter 1

Introduction

1.1 Motivation

Tissue composition and consequently some of its characteristics, such as tissue compliance, viscoelasticity, and surface texture, are changed by disease. Cancers are the most significant classes of such diseases, and are responsible for about 13% of all deaths accounting for 7.4 million death in the world during 2004 [3].

Tumors are generally harder than normal tissues making them possible to be detected by tactile feedback. In other words, tactile feedback is necessary to discriminate between healthy and diseased tissue. For example, breast cancer is usually a harder region surrounded by normal regions, and prostate cancer is generally a firm nodule that is sometimes possible to be detected by rectal palpation [4, 5, 6]. It should be noted that a tactile feedback does not necessarily guarantee the detection of an abnormal tissue characteristics, and the abnormality is not necessarily cancerous.

Detecting the tumours accurately is still a challenge, and many researchers are trying to improve the existing methods. Palpation cannot give quantitative measurements of the detected features and is difficult to administer as it only relies on the surgeon's expertise that can be erroneous or subjective [7]. Measuring the mechanical

properties of biological tissues is also required for many medical applications, such as surgery simulation and diagnostics [8, 9, 10, 11]. In order to diagnose some parts of the human body, surgeons sometimes need to obtain a tactile feedback either during an open surgery or using a special tool adapted for Minimally-Invasive Surgery (MIS) and therapy.

MIS, where the surgeon operates through one or more small incisions, has become popular due to its improved patient recovery as compared to open surgery. MIS procedures are designed to allow mechanical access to the interior of the body with the least possible perturbation of the patient's physiology and are sometimes grouped under the term *minimal access surgery* because it is the injury of access that is specifically minimized [12]. This may result in shorter hospital stays, or allow outpatient treatment, reducing trauma, risk of inflammation, and postoperative complications [12, 13, 14, 15, 16, 17].

However, MIS has several disadvantages including loss of tactile feedback. Performing the surgery with such impaired haptic information can lead to an increase in tissue trauma and vital organic tissue damage, and a reduced chance of detecting expected or unexpected tissue abnormalities, e.g. tumors. The surgeon does not have direct tactile feedback but only indirect sensation through the tools, which generally does not offer a "sense of touch" adequate for the surgeon, e.g. to correctly sense tissue stiffness, or the presence of blood vessels and ducts during the procedure [13]. To restore this loss of information, instruments have been developed providing a sense of touch to the surgeon. The size, motion, and fabrication of these instruments are limited due to MIS compatibility. They need to fit inside a cavity with a maximum diameter of 12 mm, and be sterilizable [10, 15, 18, 19].

1.2 Techniques for measuring soft tissue mechanical characteristics

Measuring the mechanical properties of biological soft tissues is required for many medical applications, such as surgery simulation and diagnostics [8, 2, 9, 16]. Different approaches can be used in testing biomaterials, divided to non-destructive and destructive methods which are not of interest. Nondestructive techniques can be used in open, MIS, and Non-Invasive surgeries and provide tissue information in-vivo.

It should be noted that soft tissues exhibit complex nonlinear, anisotropic, non-homogeneous, time, and rate dependent behaviour, which are extremely challenging to measure and simulate [20]. Fung [2] showed that, although the characteristics are different for different tissues, soft tissues exhibit a nonlinear stress-strain relationship. Since soft organs are composed of different materials in different combinations, their properties are both coordinate and direction dependent. Time and rate dependent behaviour is also common and explained by the theory of viscoelasticity.

Ongoing studies are improving soft tissue modeling and measurement techniques under different conditions, such as small or large deformation and linear, quasi-linear, or nonlinear mechanical behaviours, mainly to provide better equipment for surgical and medical purposes. This section provides the necessary background and literature review related to the measurement of mechanical properties of soft tissues, the most important of which is the elasticity of tissues, as a widely targeted characteristic. This paper, however, is not intended to cover all the relevant measurement techniques and developed instruments.

One of the simplest medical diagnosis procedures to distinguish between diseased and healthy tissues is palpation. Several other methods have been reported for measuring tissue viscoelasticity associated with minimally invasive surgery, where typically local loads are applied to tissue and the force/displacement response is exam-

ined, and non-invasive surgery methods, which apply an external load to the tissue and measure the internal strain or vibrations using imaging techniques.

1.2.1 Palpation

Palpation provides a qualitative and easy method to detect the low-frequency stiffness difference between healthy and diseased tissues, e.g. tumors since they usually have a higher Young's modulus than the surrounding tissue. Surgeons still widely rely on their natural senses. Usually, tumors overlooked by imaging techniques are discovered during surgery by palpation [21]. A reliable quantitative in-vivo method, however, for measuring tissue elasticity during a MIS can greatly enhance the diagnosis efficiency of this method.

1.2.2 Imaging techniques

The majority of elasticity measurement techniques are non-invasive methods that adopt elasticity scanning, such as Magnetic Resonance Elastography (MRE) and Ultrasonic imaging. In MRE, a phase-contrast MRI technique is used to spatially measure displacement patterns corresponding to harmonic shear waves [22]. Unlike MRE which uses propagating mechanical waves, major ultrasonic methods use, for example a quasi-static or dynamic stress as a probe [22, 23].

Acquired elasticity images have been shown to provide informative qualitative depiction of the elasticity of materials, but not quantitative data. This is because the applied strain field is not known or there exists no material within the strain field with a known elasticity. One solution is to add a known material to the field so that its strain serves as a reference to the tissue under investigation [24]. Other known problems of imaging techniques are inability of directly capturing out-of-plane deformations and unsatisfactory handling of high-contrast elasticity changes [25, 26]. Imaging techniques are, also, not suitable to be used inside a body cavity and to

measure the local properties of tissue. In addition, MRI and CT machines are very expensive, and CT requires tissues to be exposed to X-rays.

As a trade-off, a number of mechanical devices have been developed to perform measurements directly on tissues and compensate imaging drawbacks. Generally speaking, these instruments apply a mechanical load to the tissue and capture the tissue response (e.g. force/displacement response), from which material properties are determined.

1.2.3 Tactile sensors

Nicholls and Lee [11] define a tactile sensor to be “a device or system that can measure a given property of an object or contact event through physical contact between the sensor and the object”. Many tactile sensors are instruments that measure one or more features including displacement, temperature, pressure, force, and their corresponding position, and measure material properties based on the gathered data. Tactile sensing is also referred to the perception of surface texture or pressure profile distributed across the contacting surface or continuous-variable sensing of forces in an array, while the movement and bulk forces acting at the joints of either a human or a mechanical arm is sometimes distinguished as kinesthetic sensing [27, 28, 29, 30, 31]. We comply with Nicholls and Lee representing tactile sensing as a general definition and will refer to sub-categorizes as e.g. pressure-based or force-based.

These tactile-sensing instruments are mainly distinguished as stretching, shearing, and indentation devices, graspers, and robot skins, which incorporate single sensors, 1-D, or 2-D array of small sensors [9, 32, 33, 34, 35, 36, 37, 38, 39, 40, 41]. Tactile sensors can use different methods to interpret the gathered information, e.g., from an array of force sensors. Signal and image processing tools has been used to evaluate the response of a tissue (noting that an array is essentially an image). These tools incorporate time-domain and frequency-domain analysis of the captured information,

and are used to interpret the results as the desired properties of the tissue under experiment.

We introduce some of the more advanced instruments, whose fundamentals cover almost all the proposed instruments published in literature and becomes easy to follow. For this purpose, these instruments are categorized as indenters and graspers.

1.2.3.1 Graspers

As previously mentioned, researchers integrated sensory channels, i.e. pressure or force into conventional MIS graspers to restore the impaired tactile information to the surgeon. The developed hand-held graspers can be categorized into two groups: so-called force-based graspers employing force sensors providing local information about a single contact point [42, 43, 44, 45], and so-called pressure-based graspers employing pressure sensory elements providing local information associated with a pressure profile distributed over an array of the touching elements [46, 47, 48]. These elements have been mounted on the jaws of a grasper in 1D or 2D pattern.

It should be noted that tissue stiffness can be evaluated by measuring force over a surface that causes a roughly constant deformation on the tissue or by measuring both displacement and force related data. In the former, a connection can be constructed between the stiffness of the tissue and the force distribution using experimental and statistical data. It is worth mentioning that as the tissue samples become stiffer, the required force to achieve the same compression increases. For example, some studies [46, 49] categorized tissues as soft (for normal tissues) and hard (for tumorous tissues) based on a threshold on the measured force or pressure data. In the latter case, the grasper can be used to track changes in the stiffness distribution over the tissue and consequently to localize tumors by measuring rheological properties of tissues, and yet experimental and statistical data [15, 42, 50].

In graspers, the main focus is on the fabrication of small and accurate sensors

on the surface of the grasping section in a 1-D or 2-D array. A tactile array may consist of discrete sensors or a continuous sensor material. Some known problems of the former are the manufacture difficulties of interconnecting wires, and cross-talking error [33]. Some other issues in graspers are appropriate dimensions for MIS, required high-accurate deformation/force measurement, backlash, etc.

1.2.3.2 Indenters

Previously, indenters for measuring the consistency, hardness, or stiffness of soft tissues by measuring the displacement/force (strain/stress) correlation in the tissue have been proposed [10, 16, 51, 52]. A number of studies suggest techniques based on frequency response analysis to detect tissue mechanical characteristics. These methods have been proposed incorporating open-loop or closed-loop vibration amplitude, frequency shift, and bandwidth analysis [6, 8, 53, 54, 55, 56, 57, 58, 59, 60] to be discussed in Section 1.2.3.4, which are the focus of this work. A number of available indenting instruments are reviewed, categorized as stress-strain based sensors, and resonators.

1.2.3.3 Stress-strain based sensors

The mechanical behavior of biological tissues is governed by some stress-strain (or displacement-force, not to be mentioned later for simplicity) relationship and related parameters e.g. strain rate. In order to determine the mechanical properties of tissues and/or developing suitable mathematical tissue models, one may capture the strain-stress responses. Stress-strain curves obtained from experiments performed on biological tissues have several applications including medical diagnosis, more optimized surgical instrument design, tissue modeling, and the production of realistic computer-based simulators for training in minimally-invasive surgery.

In earlier works, Leveque et al. [32] proposed an apparatus for measuring the

consistency or hardness of skin tissue by measuring the displacement in the tissue, able to avoid the need to be carefully positioned using a control circuit. Hechtenberg et al. [9] proposed a method that uses one or more sensor arrays which are sensitive to force, pressure, or travel, and an actuator array in such manner that one controls the other to form a “feeling” or “tactile” unit.

Ottensmeyer et al. [10, 16] introduced an MIS instrument, TeMPeST 1-D. This instrument is capable of measuring the small-strain (0 – 5%) stiffness of solid organ tissues in a range of frequencies of 0 – 200 Hz by applying a sinusoidal translational indentation. The 12 mm-diameter tool is driven to vibrate by an open-loop voice coil motor. It collects the applied force of up to 300 mN using a high-precision piezoresistive force sensor and the relative displacement data using an LVDT sensor. It then provides tissue properties based on the captured force/displacement curves and FFT analysis. Capability of measuring the frequency response of a tissue has made TeMPeST 1-D of interest for many researchers [16, 51, 61]. It, however, requires high sampling intervals of up to 30 s to provide the results. For proper measurements, the indentation should be applied perpendicular to the tissue, and the tissue should remain without motion during the acquisition time. Moreover, significant noise may be introduced to the measured frequency-domain response using the ratio of force and position [16].

Kalanovic et al. [51] designed a rotary shear device, ROSA-2. similar to TeMPeST 1-D. A galvanometer is used to apply torque, and a non-contact analog optical sensor captures the relative rotations up to $\pm 15^\circ$ with a resolution of approximately 0.004° . A closed-loop positioning system is also used later to improve the bandwidth of the system. ROSA-2, however, requires high sampling intervals of up to 100 s to provide the results, and it is sensitive to tissue motion. Requiring accurate fabrication, the device becomes relatively expensive. ROSA-2 and TeMPeST 1-D have been compared in [51] and the results are compatible for the common range of frequencies they can

provide.

Carter et al. [52] performs two sets of indentation tests using a stationary probe, and a hand-held probe. For static measurement, the probe is clamped vertically over the tissue specimen, and applies a force on the round-ended tip against the tissue at a constant rate. The force and displacement outputs are captured by NI LABVIEW at a sampling rate of 15 Hz. In-vivo experiments on human liver are also performed using a hand-held compliance probe during open surgery. The instruments collect stress-strain data for an indentation depth of 5mm. The hand-held instrument can provide stress-strain data for a wide range of deformations; however, the amount of the deformation needs to be limited not to damage the tissue. Moreover, the device needs to be accurately positioned for reliable measurements.

Aoki et al. [19] introduced the pipette aspiration technique as a simple method of identifying Young's modulus of a soft tissue. Suction is used to deform the tissue instead of indentation, and an optical sensor is used to record the produced displacement. For conducting experiments, one end of the pipette is placed perpendicularly on the surface of the material. The pressure inside the pipette is, then, gradually decreases so the surface of the material is aspirated into the pipette. The maximum displacement of the material, happening at the center of the pipette cross-section is measured, and employed to calculate the modulus of the tissue. One of the main issues in this work is to establish a connection between the data and the complex behavior of the tissue thereby calculating the elasticity of the tissue. Numerical simulations under the assumption of isotropic, incompressible, homogeneous, and linearly elastic material by the linear finite element method were performed to do so. The implementation of this method and its analysis in finite element method is later extended to broader applications and more general tissue mechanical behaviors [62, 63, 64].

Other similar procedures are also presented in literature. Miller et al. [65] used an indenter with a spherical tip to apply a rate-controlled indentation and capture

the force response. Kassner et al. [66] employed a laparoscopic tool, INKOMAN. The feedback is provided by a force signal from a 3-DOF force sensor mounted at the tip of the instrument. Naish et al. [27] used a Gamma force/torque sensor and a handheld MIS probe to evaluate the effect of velocity control on kinesthetic tumor localization based on tissue stiffness variations.

A number of robotic-based devices are also proposed. For example, Trejos et al. [28, 29] presented employing capacitive-based pressure sensors on an MIS tool. A robotic manipulator then holds the probe to maintain either constant depth or constant force on the tissue under experiment, and a 2D map of the pressure profile of the whole tissue is then created, and analyzed to evaluate tissue stiffness.

1.2.3.4 Resonators

A set of other techniques are categorized as resonators, also sometimes called vibrotactile sensors. These instruments generally measure properties of a tissue by vibrating in specific frequencies and analyzing the frequency response. These instruments take advantage of frequency-domain analysis near their resonance modes to measure the mechanical properties of soft tissues. Many of these methods inspect the principles of viscoelasticity and/or mechanical resonators, or spectral analysis to measure tissue properties. The frequency and phase characteristics of the output signal (usually the displacement of the contact point) of these instruments will change when in contact with soft tissues. Generally, the mechanical behaviour of the instrument changes when in-contact with another mechanical system, which is a tissue in this purpose. The resonance frequency shifts are shown to be related to tissue elasticity, while the change in the bandwidth of the frequency response is related to viscosity [18, 67, 68, 69, 70].

Resonators eliminate the use of force sensors in order to capture stress-strain data. On the other hand, these methods only provide information of the tissues

excited by a periodic signal with a range of frequencies near the resonance of the instrument. These methods have been used in a wide variety of applications from surgical diagnosis and robotics to food control. Ohtsuka et al. [71] have applied this technique to thoracoscopic operations for the localization of small invisible nodules in the lung, while Hasegawa et al. [72] introduced an active tactile sensor working in both quasi-static and vibrating modes to provide a tactile skin for robot arms. Matsumoto et al. [73] used the proposed resonating tactile sensor to ascertain the presence of a gallstone in the gall bladder or cholecystic duct during laparoscopic cholecystectomy and also to be able to discriminate between a stone and an air bubble during intraoperative cholangiography. In [6], the modified resonator device is used in an 8x8 array haptic sensor for breast cancer detection. Wang et al. [74] used frequency domain characteristics to evaluate the firmness of a fruit.

- Mechanical design

A set of studies based on phase shift circuit in a feedback network (discussed later) [5, 6, 8, 35, 75, 76, 77, 78] suggest a tactile sensor consisting of driving and detecting piezoelectric stack elements, mainly PZT ceramics. The actuator then oscillates along the longitudinal axis of the instrument. The proposed instruments may suffer from high sensitivity to the effective mass of the tissue depending on the radius of the indenter tip. To overcome this problem, the tip of the instrument has to be built with very small radius, which is more difficult and expensive, or becomes useful for detecting the stiffness of cells instead of macroscopic tissue behaviours.

In [6], a modified device is used in an 8×8 array haptic sensor for stiffness measurement with an elastic cover working with a digital phase-shift circuit and a PC. Experiments have been conducted on silicones with different elasticity, and a calibration equation is derived. Each probe has an outer diameter of 6 mm, and length of about 15 mm. It takes about 45 ms to complete one set of measurements, each performed with an approximate period of 7 ms. Some advantages of this method

are the capability of using image processing techniques to compensate for the errors of each probes used in the array. The size, shape, and sensitivity are a number of drawbacks of the device [6].

Other instruments applying translational indentation at their resonance frequencies are also introduced [56, 57]. Harb et al. [58] proposed a probe consisting of a stiff cantilever beam vibrated axially by a PZT element cemented on one side, and a strain pick-up PZT element on the other side of the beam.

Valtorta and Mazza [59, 79] proposed a torsional resonator device (TRD) measuring the shear modulus of tissue samples in a frequency range of 1 – 10 kHz. Electromagnetic transducers are used to excite the system at its resonances and also for measuring the motion of the tip. Typically 20s of operation time is necessary to extract material properties in this method. For providing a more accurate analytical model, any sliding between the resonator and the tissue should be avoided. Therefore, a crystal silicone with micro opening is used at the tip where the body of the instrument is a tube, and the tissue is clamped to the tip by reducing the internal pressure of the tube. With this structure, the tissue is not damaged. Due to the small contact area, a local characterization is achieved. It is, however, relatively costly in comparison to the instruments that do not require a fabrication accuracy in the order of microns.

Mechanical resonators working based on the same principles but having the resonance frequencies of the system lie in a lower range are also proposed [18, 54]. As shown in Fig. 1.1, extra spring-mass systems are incorporated into the instrument. The resonance frequency of the instrument is kept low enough to filter out the effective mass of the tissues, and to make tissues exhibit more informative behaviors (e.g. viscoelastic behaviors); at very high excitation frequencies, tissues begin to behave linearly thus exhibiting only their elasticity [2, 18, 54]. Other advantages of using a more compliant instrument are that it allows the tool to conform to a wider range



Figure 1.1: Low-frequency resonance mechanical resonator

of tissue stiffness values while minimizing the contact forces. In case of poor control over contact forces, it is also beneficial in smoothing the mechanical impacts [80].

- Detection of frequency-domain characteristics

Now that the mechanical instrument is designed, the desired frequency-domain characteristics need to be determined. Vidic et al. [53] has analyzed the response of a resonator using a spherical indentation tip in two modes: monitoring the frequency at constant phase, and monitoring the phase at constant frequency. Relationships have been derived for the equivalent mass-spring-dashpot model of the semi-infinite material, and have been verified by several experiments.

Another method of resonance frequency shift detection is a Phase-Locked Loop (PLL) system [54, 57, 58, 67]. Barthod et al. [57] used a PLL with a resonator in an open-loop system. The VCO generates a sinusoidal wave in a range of frequencies between a minimum and a maximum desired frequency, where the signal is modulated by a triangular wave. When the system reaches to a desired state, i.e. the resonance, the resulting frequency is displayed. A fairly generalized closed-loop PLL system for a resonator is presented in this project. The most significant advantages of a PLL system are its robustness and noise rejection capabilities. A PLL system, however, is a very nonlinear system, so it is hard to be analyzed using linear control theory [81].

In 1992, Omata et al. [35] introduced automatic near-resonance shift detection based on a phase shift circuit in a feedback network. The feedback network consists of the sensor element, amplifier, and a phase-shift circuit. When the sensor makes contact with a material such as a tissue, the phase of the output signal shifts ($\Delta\theta_1$). As a result, the feedback circuit, which has the necessary phase shift, makes the oscillating system adjustments by shifting the input signal ($\Delta\theta_2$) and satisfying a

phase zero condition, $\Delta\theta_1 + \Delta\theta_2 = 0$. Lindahl et al. [68] states that this method of excitation can provide higher sensitivity and linearity since it works at slightly higher or lower frequency than the resonance frequency and achieves higher signal-to-noise ratio than standard oscillation circuits. It should be noted that a PLL can also be designed to work at near-resonance modes [54, 58, 81].

The generic proposed method as it works at very high frequencies, however, may lead to high elasticity measurement errors. This issue is discussed based on Murayama 2008 [6] with an example. In their results, the in-contact Δf_r with elastic modulus of 0 can be read approximately -4500 Hz, while in-contact with a tissue having a modulus of 50KPa, it reads about -3500 Hz. Now assume a $\pm 10\%$ deviation in the density of tissue from an expected density; it leads to a Δf_r of ± 450 Hz, which leads to about 50% error in measurement of tissue elasticity. To filter out the inertial parameter of the tissue, Murayama [6] has conducted experiments on silicones with different elasticity, and calculated a calibration equation. One can see that this equation itself produces error in the correct measurement of Young's modulus.

1.2.3.5 Free-form vs. robotic measurement

Measuring soft tissue properties using mechanical tools during a minimum invasive surgery can be performed using (a) a free-form measurement, which typically involves the use of a hand-held probe, or (b) a robotic measurement, where the probe is attached to a robot arm [20]. The major advantage of a free-form probe is that unexpected and risky movements are unlikely to happen and better control over the instrument is available in case a simultaneous decision were required since the surgeon manually controls the probe. Hand-held probes, obviously, are cheaper than a robotic system. The disadvantages include non-repeatability and lack of an exact reference point for displacement measurements [52]. In the case of static or quasi-static indentation devices, it is not easy to keep the probe stationary during the

measurements and hence the reference point changes as the probe moves, but this problem can be solved using devices that work at high frequencies thereby reducing the effects of low frequency disturbances mainly made by surgeon's hand. As mentioned before, robot arms are also used to provide a precisely controlled positioning system for the attached indenter. Using a robotic arm, the problems related to actuation and positioning is solved. The experiments are repeatable, automatic, and with no reference point problem, as the indenter tip coordinates can be acquired with respect to a fixed coordinate frame [20].

1.3 The proposed instrument

Until now, the features of a human skin and its connection to tissue properties have not been fully researched. It is still an open research to investigate to what degree the hardness, softness and/or other properties of tissue depends on the contact area, the contact pressure, the thickness of the contacted material, the structure of tissue, etc. While there are currently many types of tactile sensors in use in a variety of fields, sensors fulfilling the above conditions have not yet been fully developed. Moreover, tactile sensors do not directly measure viscoelasticity [18] as an important property for understanding the conditions of tissue. Nevertheless, these sensors still gather informative data that can be used in several applications such as endoscopic graspers [13], MIS tools, and robot tactile skin.

The proposed resonators, presented above, either are not capable of being MIS, or are only based on simulations, or may lead to big errors depending on the effective mass of the tissue and the relevant assumptions. Another issue that applies to many of the studies over tactile sensors is capability of and optimization for measuring tissue properties in-vivo, i.e. performing the measurement on the patient's tissue during the surgery. Recent experimental studies report that mechanical properties of soft

tissues obtained through in vivo measurements are different from properties obtained through measurements under other conditions such as in-vitro, in-situ, and ex-vivo [16, 64, 82]. In vitro or ex vivo measurements are performed outside the body under well-defined boundary conditions.

Furthermore, resonators that are optimized for measuring the mechanical properties of soft and very soft tissues have not been considered in literature, and the feedback system is not studied properly.

In this thesis,

1. The relevant principles are described, and the mechanical design of the dynamic MIS instrument integrated into an MIS tool is introduced.
2. A state-space model is constructed for the system. The model is then analyzed parametrically and numerically, and the affecting criteria and conditions on the design of the instrument are discussed, and used to optimize the system.
3. The PLL-based feedback system is described.
4. A number of finite-element and lumped-parameter simulations are performed to ensure satisfactory performance of the instrument and to understand and analyze the behaviour of the proposed system.
5. Experiments have been performed to validate the performance of the instrument, to measure the mechanical properties of cantilever beams and springs, and localize the tumours in soft phantoms.
6. Conclusions and future work are discussed.

1.4 Contributions

A list of contributions and advantages of the proposed system are as follows:

1. The proposed instrument is designed to provide mechanical properties of the tissues in a low range of frequencies in contrast to other resonators used for the same application. Both elastic and viscous properties are present at lower frequencies, while viscous properties become negligible at very high frequencies. Moreover, working at lower frequencies the effect of the density of the tissue is minimized.
2. An optimization procedure is introduced for measuring the properties of soft tissues, and consequently the precision and accuracy are highly improved in comparison to similar instruments.
3. The instrument can be easily disassembled, and it is sterilizable, so it is appropriate for surgical environments.
4. A PLL-Based feedback system, incorporating an extra feedback loop (comparing to common PLL systems) is employed to detect the resonance or near-resonance frequency shifts of the dynamic low-frequency instrument. A generalized feedback system is introduced and described.
5. A novel numerical method for correlating the tissue parameters and the changes in eigenvalues of the system is also presented. This formulation can consider for an n th-order approximation. It is later shown that the 2nd-order approximation improves the accuracy of the measurements up to 12%, while all other studies consider a linear correlation.

Chapter 2

Mechanical system design

2.1 Principles

2.1.1 Principles of viscoelastic materials

Soft tissues can be modeled as viscoelastic materials. These materials themselves are characterized by their viscous and elastic properties. For a slice of material with cross-sectional area, A , and thickness, T , subject to a sinusoidal load, $F(t)$, the corresponding displacement function, $x(t)$, is given. The cyclic stress, σ on the sample material is found by dividing the input load by the cross-section area, and the resulting cyclic strain, ϵ is found by dividing the displacement by the thickness.

In a material possessing purely elastic behaviour, all the energy stored in the sample by applying a load is returned when the load is removed. Therefore, Hooke's law (2.1) applies where the modulus is defined as the ratio of stress to strain and the stress is proportional to strain. In other words, the stress and strain curves in time domain move completely in phase. Stiffness is then defined as the resistance of an elastic body to deformation by applied force [69]. This is one of the most important characteristics of a soft tissue.

$$E = \frac{\sigma}{\epsilon}, k = \frac{F}{x} \quad (2.1)$$

On the other hand, in a purely viscous material, all the energy is lost in the form of damping when the load is removed. In this case, the stress is proportional to the strain rate, and this ratio (2.2) is known as Newtonian viscosity or simply the viscosity, η . Damping is any effect that tends to reduce the amplitude of oscillations of an oscillatory system. For a purely viscous material, the force applied to the material is proportional to the velocity by viscous damping coefficient, c .

$$\eta = \frac{\sigma}{\dot{\epsilon}}, c = \frac{F}{\dot{x}} \quad (2.2)$$

For all others that do not fall into one of the above extreme classifications, some of the energy stored is recovered upon removal of the load, and the remainder is dissipated in the form of heat. The cyclic stress at a loading frequency is out-of-phase with the strain by the loss angle δ ($0 < \delta < \pi/2$). The angle δ is a measure of the materials damping level; the larger the angle the greater the damping [69].

For a viscoelastic material, the dynamic modulus, E^* is represented by a complex number, where the real component is called storage modulus (usually shown by E_1 or E') which relates to elastic behaviour of the material, and the imaginary component is called loss modulus (E_2 or E'') which relates to viscous behaviour of the material. This complex modulus can now be used in Hooke's law [69].

$$\epsilon = \epsilon_0 \sin(\omega t) \quad (2.3)$$

$$\sigma = \sigma_0 \sin(\omega t + \delta) \quad (2.4)$$

$$E^* = E' + iE'' = E' + i\omega\eta_e = E'(1 + i2\zeta_e) = \frac{\sigma_0}{\epsilon_0} e^{i\delta} \quad (2.5)$$

$$\tan \delta = \frac{E''}{E'} \quad (2.6)$$

where η_e is the equivalent viscosity of the tissue (defined in Pa.s), or essentially a non-viscous viscosity for mathematical convenience, and ζ_e is the equivalent damping ratio of the tissue. A similar term is also defined for shear modulus of tissue material.

$$G^* = G' + iG'' = G' + i\omega\eta_g = G'(1 + i2\zeta_g) = \frac{\tau_0}{\gamma_0} e^{i\delta} \quad (2.7)$$

noting that E , G , and bulk modulus, B are interconnected as below.

$$E = 3B(1 - 2\nu) = 2G(1 + \nu) \quad (2.8)$$

where ν is Poisson's ratio. Since for biological soft tissues, ν is about .5, it is very hard to estimate E from B though.

The properties of viscoelastic materials are influenced by many parameters, including frequency, temperature, dynamic strain rate, static pre-loads, boundary conditions, time effects such as creep and relaxation, aging, etc [2, 69]. In other words, the complex modulus needs to be defined as a function of these parameters, most important of which is frequency and temperature effects. As this study is focused on soft tissue viscoelasticity measurement on environment and/or in-vivo temperature, the effect of temperature can be neglected, and a simple yet effective tissue model can be employed, i.e. a viscoelastic material.

The design of the instrument is significantly related to the damping factor of the tissue. Unfortunately, damping parameters vary enormously, and authors often do not provide the information related to damping. Therefore, it is necessary to recognize methods of estimating damping factors to be able to extract them from the literature. below, a brief description of standard methods is presented.

The viscous damping is most often represented by a damping ratio ζ , given below.

$$\zeta = \frac{c}{c_0} \quad (2.9)$$

where for a simple spring-dashpot-mass system,

$$c_0 = 2\sqrt{mk} \quad (2.10)$$

A quantitative measure of damping is achieved by estimating the bandwidth of stiffness transfer function of the material. In this case, the material damping, μ , equals the ratio of the system's bandwidth to the resonance frequency, f_r . Another representation of damping for this system is the quality factor, Q as the ratio of the response magnitude at resonance to the static magnitude. The quality factor is also defined as

$$Q = \frac{df}{f_r} \quad (2.11)$$

The damping is then defined by the following equations.

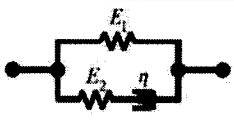
$$\mu = \frac{1}{Q} = 2\zeta = \frac{\Delta f_{3dB}}{f_r} = \frac{\Delta \omega_{3dB}}{\omega_r} \quad (2.12)$$

where Δf_{3dB} and $\Delta \omega_{3dB}$ represent the bandwidth corresponding to the cutoff frequencies above or below the peak frequency where the output signal is attenuated by 3dB.

2.1.2 Basic tissue models

Some simple rheological models for solids include Hookean material, Voigt material (VM), and standard linear solid material (SLS) [69]. The structure and laws for these material models are summarized in Table 2.1. There also exists modified versions of the described models in the literature, and generalized models are also incorporated.

Table 2.1: Simple soft tissue models

	Structure	Formulation
Hookean model		$\sigma = E\varepsilon$
Voigt model		$\sigma = E\varepsilon + \eta\dot{\varepsilon}$
SLS model		$\dot{\sigma} + \frac{\sigma}{T} = (E_1 + E_2)(\dot{\varepsilon} + \frac{\varepsilon}{T^*})$ $T = \frac{\eta}{E_2}, T^* = T(1 + \frac{E_2}{E_1})$

These simple models can be modified to have extra components. For example, a VM model with mass (VMM), also called a mechanical impedance, includes an effective mass on the surface contacting an indenter.

Several common responds of a tissue model are briefly described.

During a relaxation test, the strain history is prescribed as a step function. From the numerous existing mechanics literature, one calculates the so-called relaxation curve $E(t)$ [2, 69]. One can see that for a SLS model, the stress decreases exponentially from the initial value to the asymptotic value. This phenomenon is generally denoted stress relaxation [69].

In a creep test, the stress is assumed to be a step function, and the so-called creep curve is calculated. The ratio of the creep curve $\varepsilon(t)$ to σ_0 is called the creep compliance $J(t)$. From the derived equation, one sees that for a SLS material, the strain increases exponentially. This phenomenon is called creep or stretch retardation [69].

Previously, the material behaviour of a linearly viscoelastic solid was considered under oscillating load in terms of complex modulus. A SLS material yields the following relations for the complex modulus. The frequency-dependent behaviour of complex modulus of a SLS material is visualized in Fig. 2.1.

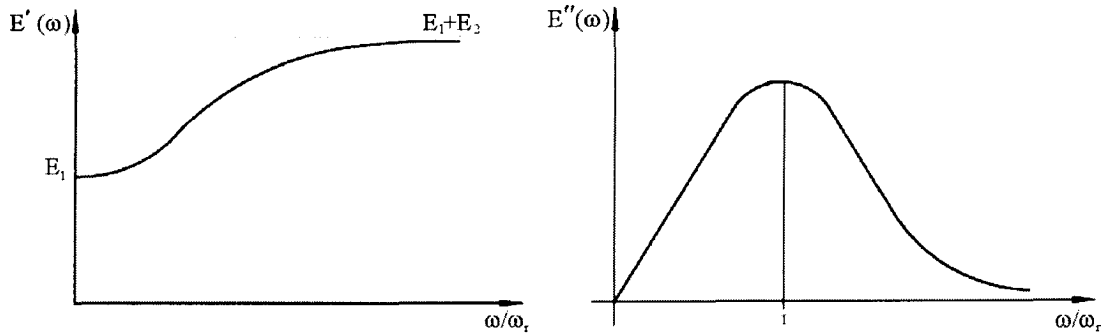


Figure 2.1: (Left) Storage modulus of a SLS material (Right) Loss modulus of a SLS material

$$E' = \frac{E_2 + (E_1 + E_2)\tau_e^2\omega^2}{1 + \tau_e^2\omega^2}, \quad E'' = E_1 \frac{\tau_e\omega}{1 + \tau_e^2\omega^2} \quad (2.13)$$

It can be seen that with increasing frequency the stiffness also increases. This behaviour is called dynamic stiffening. One can also see that the loss modulus disappears at very low and very high frequencies, that is the material behaves purely elastic.

2.1.3 Resonance frequency shift of a mechanical impedance

A number of studies measure the stiffness of biological or non-biological tissues using the resonance frequency shift (Δf_r) phenomenon as described before. Ideally, the effective stiffness of the material increases Δf_r , while the effective mass reduces Δf_r . The effective damping of the material increases the bandwidth of the system, Δf_{3dB} , so the damping factor can be determined as prescribed in Section 2.1.1.

A number of studies measure Δf_r at very high frequencies using a PZT transducer [8, 6, 35, 76]. Since they are working at very high frequencies, the damping of the material is completely negligible, so Δf_r is only affected by the effective mass and the stiffness of the material. However, if the transducer is resonating at very high frequencies, the effective mass will dominate the changes in Δf_r of the system. In

their studies, they have categorized $\Delta f_r = \frac{\Delta\omega_r}{2\pi}$ in two different equations as follows.

$$\Delta\omega_r = \begin{cases} -\frac{k_0 m_m}{\pi Z_0 m_0} & (a \gg 1, k_m \text{ small}) \\ \frac{k_m}{\pi Z_0} & (a \ll 1, k_m \text{ big}) \end{cases} \quad (2.14)$$

where m_0, k_0, Z_0 are the instrument's effective mass, stiffness, and mechanical impedance respectively, and m_m, k_m are the material's effective mass and stiffness in a lumped parameter spring-mass system. Equation (2.14) implies that for a soft tissue (small k_m) the effective mass of the tissue dominates the stiffness of the tissue as expected.

The mechanical impedance of a spring-dashpot-mass system is defined as the transfer function between the applied force and velocity. The above equations hold for a system with an effective mechanical impedance, and can be written in the closed form below when employing a quartz resonator [83].

$$\Delta\gamma - i\Delta f = \frac{f_0 Z_l}{\pi Z_0} \quad (2.15)$$

where Z_0 is the effective impedance of the sensor at the initial resonance frequency, f_0 is the non-contact (initial) resonance frequency, Δf is the resonance frequency shift, $\Delta\gamma$ reflects the half-width of the resonance, and Z_l is the load mechanical impedance, defined in (2.16). It should be noted that $\Delta\gamma$ directly relates to the change in the real component of the corresponding eigenvalue of the system, and thus the change in damping. One may refer to [83] for detailed formulation.

$$Z_l = m_m \omega i + c_m - \frac{k_m}{\omega} i \quad (2.16)$$

At very high frequencies, as said before, the effective mass of the material dominates in the mechanical impedance. Therefore, the Δf becomes negative when the instrument is in contact with a soft tissues, and positive when in contact with a very stiff material [35, 8, 76, 77, 6]. This means that as far as the instrument is used to

measure elasticity of soft tissues quantitatively, they need to determine a value for the effective mass. This can be done by assuming an average effective density for the tissue about that of water, but this assumption may lead to high errors in detection of stiffness. A discussion of this was conducted in Section 1.2.3.4.

The resonance frequency shift phenomenon can also be interpreted using a lumped parameter state-space system model. In later chapters, a complete state-space model of the system will be designed, and the frequency shift and bandwidth of the system is found through numerical approximations.

2.2 Instrument layout

The proposed instrument, shown in Fig. 2.2, consists of two springs and masses combined together to form two resonance frequencies below 100Hz as explained in Section 3.3. The springs and masses, actuator, and the sensors can be placed in different layouts each have their own benefits, while it is still theoretically possible to reach the same performance from this layout with different design parameters from another design. Practical mechanical design issues, however, dictates the simplicity of the instrument's physical design, i.e. the placement of sensors and actuator, their wires and other electrical components [54]. The instrument fits into an MIS tool with an diameter of 11.5 mm, and it weights about 100 g. Some of these issues are listed as follows:

1. Easy implementation and safe wiring, and possibility of easy shielding.
2. Commercially available and cheaper components that best fit for the design.
3. Easy assembly and dis-assembly, thereby being easily sterilizable.

Therefore, a design layout that corresponds to a simple prototyping is selected, shown in Fig. 2.2, where the actuator is placed at the end of the instrument. The actuator

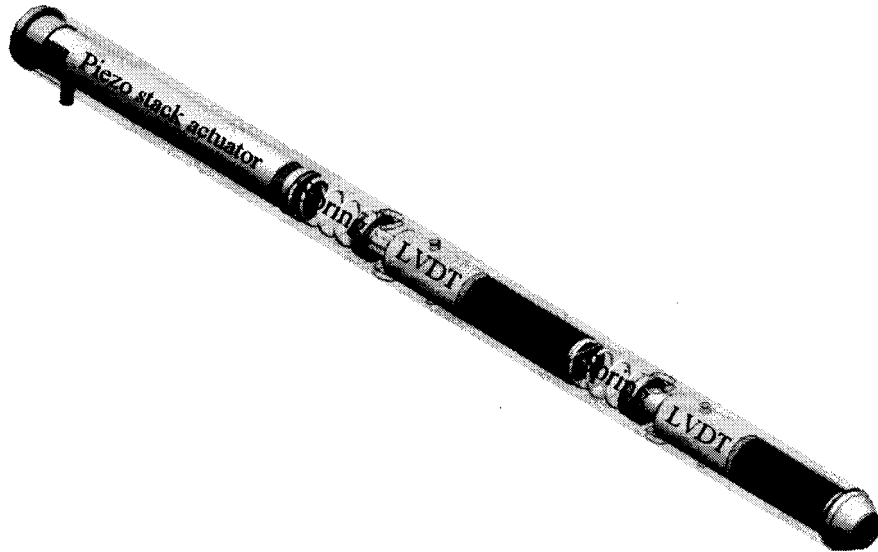


Figure 2.2: Design layout for MIS instrument

can be placed at both ends of the instrument or at the middle of the instrument; however, the wiring of the actuator complicates the design of the device due to MIS size limitations. To form two resonance frequencies, two mechanical resonance modes need to be created using springs and masses.

2.3 Transducer selection

2.3.1 Displacement sensors

To measure the displacement of the tip mass and proof mass of the tool, which are dependent to the deformation of the tissue, two displacement sensors are employed. In order to capture the resonance frequency shifts (to be explained more later), it is only necessary to measure one of the aforementioned displacements, however, both are employed, so it is possible to study the behaviour of the instrument more thoroughly.

To avoid introducing extra friction to the system (such as would be present in

a potentiometer), non-contact position sensors were considered for the design. A summary of advantages and disadvantages of these types of sensors is provided in Table (2.2). Non-contact displacement technologies are increasingly being used for precision measurement, most of which are Linear Variable Differential Transformers (LVDT), capacitive sensors, inductive (Eddy current) sensors, laser sensors, and optical encoders. It is considered that the instrument should remain as less expensive as possible as opposed to using a laser interferometry. The sensor is also required to fit within the confines of a 12mm MIS tool shaft. Many displacement sensors, such as commercially available optical encoders [16], satisfying a reasonable range and resolution fail to maintain this criterion. Moreover, the structure and wiring of the commercially available capacitive and inductive sensors does not allow for an easy layout of the system i.e. easy to assemble, and they become relatively expensive.

As the instrument is supposed to work at room/body temperature, maybe in some wet or polluted environment, but in a non-magnetic environment as in a surgery room, an LVDT sensor is the best choice. The LVDT sensor is required to provide enough accuracy and a proper frequency response. It should be able to work with enough high frequency modulated signal, so that the delay caused by the sensor is minimized. It should be noted that this delay can directly show itself in the measurement of resonance frequency shift Δf_r . The shape of the LVDT is also important. It should fit within the tool shaft, and have its wires come out from the sides of the LVDT in order for them not to touch the moving parts. In this case, the LVDT body is fixed to the shaft of the instrument, while the core is moving. Schaevitz 050-MHR is selected for the purpose of this work. Numerical criteria for this selection is presented in Section 3.3.

Table 2.2: Summary of non-contact displacement sensors

	Advantages	Disadvantages
Eddy Current	Can be used on all metals. It is small size. High temperature range. Highly accurate. Immune to changes in measuring gap.	Output and linearity depends on the target. The diameter increases as the measuring range increases. Moderately expensive. Improper structure for the design for commercial sensors.
Capacitive	High linearity and resolution against metal targets. high thermal stability.	Sensitive to the sensor gap, only clean and dry applications. Metallic parts must be insulated, complicating the design. Sensitive to temperature. Comparably large. Improper structure for the design for commercial sensors.
LVDT	Highly linear. High resolution. Simple in structure. Light. Easy to assemble and design for our case.	Sensitive to a magnetic field. Low in output power. Temperature sensitive.
Laser interferometry	Small beam spot. Long measuring ranges. Independent of the target material.	Large. relatively clean optical path is required. specific sensor alignment/calibration is required. Very expensive. The structure of the sensor is not appropriate.

2.3.2 System actuator

One of the main components for the instrument design is its actuator. The selection of the actuator has direct relationship with the performance of the designed system. Therefore, different actuation types have been studied, and the best choice is selected. An overview of the advantages and disadvantages of several considered actuation systems is shown in 2.3.

Mechanical actuators typically convert rotary motion of a control knob or handle into linear displacement via screws and/or gears to which the knob or handle is attached. They are mostly not as accurate as what it is required for this design. Extra circuitry, mechanical components and feedback system design may be required in comparison to other available actuators.

It is possible and also cost and complexity-efficient to achieve a direct linear actuation. The available moving coils that could produce high enough stroke were not as small as required in MIS, and their response is also not as robust and reliable as piezoelectric actuators. A feedback system would have been necessary for controlling the position of the coil for the proposed system.

A piezoelectric actuator, on the other hand, can produce small enough motions, is proper in size, and improves positioning performance of the proposed instrument. Very high voltages correspond to only tiny expansions. As a result, piezoelectric actuators can achieve extremely fine positioning resolution, but also have a very short range of motion. In addition, piezoelectric materials exhibit hysteresis which makes it difficult to control their expansion in a repeatable manner. These issues are, however, not problematic for our case. A brief review of piezoelectric materials and actuators is hereby presented.

A piezoelectric actuator works based on the phenomenon called the piezoelectric effect. The piezoelectric effect is a property of certain materials in which applying a voltage to the material causes it to expand. Piezoelectric materials are crystalline

Table 2.3: Summary of linear actuators

	Advantages	Disadvantages
Electro-mechanical	Cheap. Repeatable. Self contained. Identical behaviour extending or retracting. DC or Stepping motors.	Many moving parts prone to wear. Relatively big. Relatively low resolution.
Linear motor	Simple design. Minimum of moving parts. High speeds possible. Self contained. Identical behaviour extending or retracting.	Low force. Size. Bad structure. Needs a feedback control.
Piezoelectric	Very small motions possible. Robust. High power capabilities.	Short travel. High voltages required. Expensive.
Moving coil	Force, position and speed are controllable and repeatable. Capable of high speeds and precise positioning.	Requires position feedback to be repeatable. Relatively big.

solids with an electric dipole moment sensitive to both elastic strain and applied electrical field. Stresses and strains in a piezoelectric material are related to each other by the Young's modulus of the material. Moreover, an electrical field is generated by material's stresses through the inverse piezoelectric effect. This electrical field itself is related to the material's electrical displacement since these materials are dielectric. The governing equations of a piezoelectric material are described in four equivalent types of consecutive equations. Equation (2.17) is used in this project everywhere for consistency.

$$\begin{aligned}\varepsilon &= s^E \sigma + d^T E \\ D &= d \sigma + \varepsilon^\sigma E\end{aligned}\tag{2.17}$$

where s^E is the compliance matrix (compliance data was measured under a constant electric field), d is piezoelectric coupling terms matrix, and ε^σ is the permittivity matrix (permittivity data was measured under a constant stress field).

Most of piezoelectric actuator manufacturers provide compliance and permittivity matrices tested under constant fields, so these equations are best described for static and quasi-static applications. For dynamic applications some changes may occur, for example, the dynamic stiffness of the piezoelectric actuator may become larger than static stiffness. There exist a number of piezoelectric actuator types commercially available. These types are described in brief below, where based on the requirements of our application and the existing trade-offs, a stack actuator is selected for the prototype.

2.3.2.1 Piezo stack actuators

The easiest way to produce a linear motion using piezoelectric materials is to use a stack actuator in a multilayer construction. Stack actuators are composed of several piezoelectric layers, and are produced in different dimensions based on the require-

ments of the application. The height of the stack is chosen to provide the required displacement, and the cross-sectional area is selected to provide the force capabilities.

2.3.2.2 Piezo bending actuators

Piezoelectric benders act similar to bimetallic benders. An electrical field applied across the two layers of a bender results in one layer to expand and the other to contract. The net result is a curvature in the structure leading to desired displacement. Piezoelectric benders produce relatively high displacements, but act at lower speeds, and provide very low force.

So-called disk translators also belong to the group of bi-morph piezo actuators, and provide faster response and higher force than benders for both static and dynamic applications. Compared to stacks, disk translators provide relatively large travel range in an extremely small package. The only limiting option is the large diameter of the commercially available actuators.

2.3.2.3 Piezoelectric tubes

Tube actuators are hollow actuators that produce axial and/or radial deformations while the electrical field is applied to radial axis. These actuators have larger diameter and shorter length in comparison to stack actuators. Because of the dimensional requirements of the proposed system, the fact that only axial deformation is required for the purposed of this project, and the nominal deformation and force specifications of the tubes, these type of piezoelectric actuators are not desirable.

2.3.2.4 Amplified piezoelectric actuators

Amplified piezoelectric actuators are long-stroke linear actuators working based on the expansion of the active material and a mechanism for amplifying the displacement. These actuators provide an interestingly higher range for comparable force and

displacement specifications, but the direction of the produced displacement and their shape is a big disadvantage for this application.

Chapter 3

System modeling and optimization

3.1 State-space modeling

3.1.1 Mass-spring-damper system modeling

The procedure is almost identical to the one described in the previous chapter. The only difference is that the input is now a force $F(t)$ instead of a displacement $x(t)$. The output is still the displacement $x(t)$. The transfer function is now $G(s) = \frac{1}{ms^2 + ds + k}$. The state-space representation is $\dot{x} = -\frac{d}{m}x - \frac{k}{m}x + \frac{1}{m}F(t)$ and $y = x$. The state-space representation is $\dot{x} = -\frac{d}{m}x - \frac{k}{m}x + \frac{1}{m}F(t)$ and $y = x$. The state-space representation is $\dot{x} = -\frac{d}{m}x - \frac{k}{m}x + \frac{1}{m}F(t)$ and $y = x$.

$$\dot{x} = -\frac{d}{m}x - \frac{k}{m}x + \frac{1}{m}F(t)$$

with

$$x = \begin{bmatrix} x \\ \dot{x} \end{bmatrix}$$

and

Chapter 3

System modeling and optimization

3.1 State-space modeling

3.1.1 Piezoelectric stack actuator modeling

The piezoelectric actuator integrated in the instrument helps to minimize the size and to improve positioning performance. It provides accurate and strong actuation, allowing the instrument to capture the results more reliably. In order to analyze the behaviour of the instrument more accurately and optimize the system parameters, a simple model for the piezoelectric actuator is considered. The first governing equation of a piezoelectric material can be simplified to be used in a stack actuator, which essentially is composed of n layers of a single-layer actuator. Ideally, a stack actuator only deforms in the axial direction, so a one dimensional governing equation can be used to define stack actuator's behaviour.

$$\Delta L = -\alpha F_{produced} + \beta V, \quad (3.1)$$

where

$$\alpha = 1/k_p = s_{33}^E L/A, \quad (3.2)$$

$$\beta = \frac{F_{p0}}{V_{pm}k_p} = \frac{N_p}{k_p} = nd_{33}, \quad (3.3)$$

L is the length of actuator, A is the cross-section of actuator, V_{pm} is maximum possible voltage applied to actuator. F_{p0} is maximum blocked force, and k_p is piezo actuator's stiffness. A static model of the stack actuator is equivalent to an active spring whose displacement is linearly dependent on the applied force and voltage. For a dynamic response, the mass of the stack, m_p , and a damping coefficient, c_p , are also considered.

3.1.2 Non-contact setup

The lumped-parameter model of the system is represented in Fig. 3.1. If the displacement of actuator, proof mass, and tip mass are x_p , x_1 , and x_2 respectively, then the state vector of the system is defined as

$$x = (x_1, x_2, x_p, \dot{x}_1, \dot{x}_2, \dot{x}_p)^T \quad (3.4)$$

Putting together the equations of motions of the proposed system, the following state-space model is derived for the instrument in non-contact setup. When $k_m = m_m = c_m = 0$, the instrument is working in non-contact.

$$\dot{x} = A_0x + B_0u \quad (3.5)$$

where

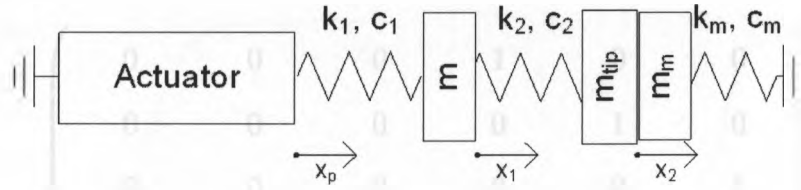


Figure 3.1: Lumped-parameter system model

$$A_0 = \begin{pmatrix} 0 & 0 & 0 & 1 & 0 & 0 \\ 0 & 0 & 0 & 0 & 1 & 0 \\ 0 & 0 & 0 & 0 & 0 & 1 \\ -\frac{k_1+k_2}{m} & \frac{k_2}{m} & \frac{k_1}{m} & -\frac{c_1+c_2}{m} & \frac{c_2}{m} & \frac{c_1}{m} \\ \frac{k_2}{m_{tip}} & -\frac{k_2}{m_{tip}} & 0 & \frac{c_2}{m_{tip}} & -\frac{c_2}{m_{tip}} & 0 \\ \frac{k_1}{m_p} & 0 & -\frac{k_1+k_p}{m_p} & \frac{c_1}{m_p} & 0 & -\frac{c_1+c_p}{m_p} \end{pmatrix},$$

$$B_0 = \begin{pmatrix} 0 & 0 & 0 & 0 & 0 & \frac{F_{p0}}{V_{pm}m_p} \end{pmatrix}^T,$$

and u equals the input voltage to actuator from amplifier.

3.1.3 In-contact with a VMM model with mass

When in contact with a tissue, the instrument has a different state-space model generating the RFS. It is desirable to be able to apply these changes into the model in a way that the tissue components are distinguishable. This is met using a Voigt model [2] with mass (VMM), also referred to as the mechanical impedance. The state-space model in this case becomes

$$\dot{x} = Ax + B_0u, \quad (3.6)$$

where

$$A = \begin{pmatrix} 0 & 0 & 0 & 1 & 0 & 0 \\ 0 & 0 & 0 & 0 & 1 & 0 \\ 0 & 0 & 0 & 0 & 0 & 1 \\ -\frac{k_1+k_2}{m} & \frac{k_2}{m} & \frac{k_1}{m} & -\frac{c_1+c_2}{m} & \frac{c_2}{m} & \frac{c_1}{m} \\ \frac{k_2}{m_0} & -\frac{k_2+k_m}{m_0} & 0 & \frac{c_2}{m_0} & -\frac{c_2+c_m}{m_0} & 0 \\ \frac{k_1}{m_p} & 0 & -\frac{k_1+k_p}{m_p} & \frac{c_1}{m_p} & 0 & -\frac{c_1+c_p}{m_p} \end{pmatrix},$$

$$m_0 = m_{tip} + m_m$$

3.1.4 In-contact with a SLS model

A state-space based on a SLS model requires an extra state in the system, i.e. between the dashpot and spring in series in the model. The complex modulus of a SLS model changes according to Fig 3.2. The state-space equations are provided as follows. Note that a SLS model with mass can also be implemented using the same concept using VMM.

$$A = \begin{pmatrix} 0 & 0 & 0 & 1 & 0 & 0 & 0 \\ 0 & 0 & 0 & 0 & 1 & 0 & 0 \\ 0 & 0 & 0 & 0 & 0 & 1 & 0 \\ -\frac{k_1+k_2}{m} & \frac{k_2}{m} & \frac{k_1}{m} & -\frac{c_1+c_2}{m} & \frac{c_2}{m} & \frac{c_1}{m} & 0 \\ \frac{k_2}{m_0} & -\frac{k_2+k_m}{m_0} & 0 & \frac{c_2}{m_0} & -\frac{c_2+c_m}{m_0} & 0 & \frac{k_{m1}}{m_0} \\ \frac{k_1}{m_p} & 0 & -\frac{k_1+k_p}{m_p} & \frac{c_1}{m_p} & 0 & -\frac{c_1+c_p}{m_p} & 0 \\ 0 & \frac{k_{m1}}{c_{m1}} & 0 & 0 & 0 & 0 & -\frac{k_{m1}}{c_{m1}} \end{pmatrix}$$

In this model, c_{m1} should always remain nonzero. Moreover, both VMM and SLS models provide a 3-DOF mechanical impedance model. Therefore, VMM is preferred

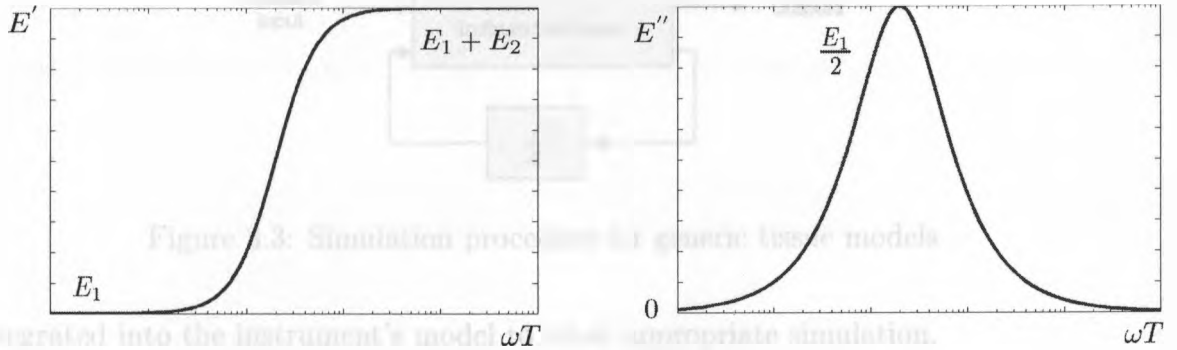


Figure 3.2: Plot of the components of the complex modulus of a generic SLS model versus ωT . E_1 , E_2 , and T are tissue parameters [2].

for resonators [2, 8, 10, 16, 52, 60, 67, 69, 84] as it satisfies the same DOF, is easier to implement and has no numerical limitations. It should be noted that for having a better time-domain response for the tissue SLS is preferred.

3.1.5 In-contact with other tissue models

Any other tissue model can be simulated numerically using a feedback system shown in Fig. 3.3. The instrument model is given below.

$$\dot{x} = A_0 x + B_1 \begin{pmatrix} V \\ F \end{pmatrix} \quad (3.7)$$

where

$$B_1 = \begin{pmatrix} 0 & 0 & 0 & 0 & 0 & \frac{F_{p0}}{V_{pm} m_p} \\ 0 & 0 & 0 & 0 & \frac{1}{m_{tip}} & 0 \end{pmatrix}^T$$

For an improper tissue model, it is necessary to integrate the tissue model into the instrument state-space model thereby constructing a larger state-space model. The SLS with/without mass model transfer functions, for example, can be used as given below, while the improper transfer function of SLS with mass model has to be

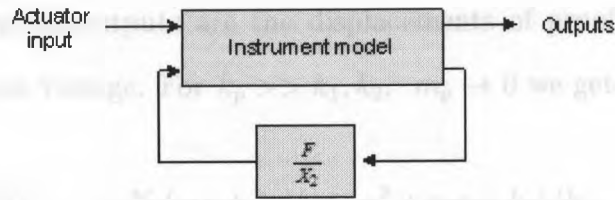


Figure 3.3: Simulation procedure for generic tissue models

integrated into the instrument's model to allow appropriate simulation.

$$\frac{F}{X_2} = -\frac{c_{m1}m_m s^3 + k_{m1}m_m s^2 + c_{m1}(k_{m0} + k_{m1})s + k_{m0}k_{m1}}{c_{m1}s + k_{m1}} \quad (3.8)$$

$$\left. \frac{F}{X_2} \right|_{m_m=0} = -\frac{c_{m1}(k_{m0} + k_{m1})s + k_{m0}k_{m1}}{c_{m1}s + k_{m1}} \quad (3.9)$$

3.1.6 Discretization

In digital control of continuous-time systems, it is required to convert the continuous-time state space to discrete-time state space equations. Such conversion can be done by introducing fictitious input and holding devices using the following equations [85]; the error caused by discretization is negligible using a sufficiently small sampling time, T .

$$\Phi = e^{AT}, \Gamma = A^{-1}(A - I)B \quad (3.10)$$

$$\begin{aligned} x[k+1] &= \Phi x[k] + \Gamma u[k] \\ y[k] &= Cx[k] + Du[k] \end{aligned} \quad (3.11)$$

3.2 Parametric model analysis

In order to identify system parameters in the non-contact setup based on experimental frequency response of the system, we need to derive the transfer function of the system

parametrically. System outputs are the displacements of proof and tip mass, and system input is input voltage. For $k_p \gg k_1, k_2$, $m_p \rightarrow 0$ we get

$$\frac{X_1}{V} = \frac{N_p(c_1s + k_1)(m_{tip}s^2 + c_2s + k_2)/k_p}{den_0s^4 + den_1s^3 + den_2s^2 + den_3s + den_4} \quad (3.12)$$

$$\frac{X_2}{V} = \frac{N_p(c_1s + k_1)(c_2s + k_2)/k_p}{den_0s^4 + den_1s^3 + den_2s^2 + den_3s + den_4} \quad (3.13)$$

where

$$den_0 = m_{tip}m \quad (3.14)$$

$$den_1 = mc_2 + m_{tip}(c_1 + c_2) \quad (3.15)$$

$$den_2 = c_1c_2 + mk_2 + m_{tip}(k_1 + k_2) \quad (3.16)$$

$$den_3 = k_2c_1 + k_1c_2 \quad (3.17)$$

$$den_4 = k_1k_2 \quad (3.18)$$

We also have

$$\frac{X_p}{V} = \frac{1}{N_p(m_p s^2 + k_p)} \quad (3.19)$$

The system's transfer functions when in-contact with a tissue can also be derived, but it is not necessary to have them parametrically as they are not to be used for calibration of the instrument.

Based on the system's state-space model, the resonant frequencies of the system are found analytically based on eigenvalues of system matrix A [86]. Formulating all the eigenvalues of A is unnecessary as the resonant frequencies of the piezoelectric actuator and damping factors in the model do not really interfere with the other resonance frequencies. A generalized formulation can be found in mechanical vibrations literature [86]. Therefore, applying the following conditions which essentially ground

the actuator, one can find system resonant frequencies as follows.

$$m_p \rightarrow 0, k_p \gg k_1, k_2$$

$$\omega_{n_{1,2}}^2 = \frac{mk_2 + m_{tip}(k_1 + k_2) \pm \sqrt{\Delta_k}}{2m_{tip}m}, \quad (3.20)$$

where

$$\Delta_k = (mk_2 + m_{tip}(k_1 + k_2))^2 - 4m_{tip}mk_1k_2$$

With a similar procedure, one can find the following equations for system damping ratios.

$$2(\zeta\omega_n)_{1,2} = \frac{mc_2 + m_{tip}(c_1 + c_2) \pm \sqrt{\Delta_c}}{2m_{tip}m}, \quad (3.21)$$

where

$$\Delta_c = (mc_2 + m_{tip}(c_1 + c_2))^2 - 4m_{tip}mc_1c_2$$

Finally, the system's damped natural frequencies are calculated below.

$$\omega_{d_{1,2}} = \omega_{n_{1,2}} \sqrt{1 - \zeta_{1,2}^2} \quad (3.22)$$

In order to correlate the frequency shifts and bandwidth changes to the parameters of a viscoelastic material, an approximate linear method is used to estimate the shifts in the eigenvalues of the system model, where the eigenvalues are directly correlated to the frequency shifts and bandwidth changes. Vidic et al. [53] previously illustrated monitoring frequency at constant phase and monitoring phase at constant frequency in a general form without solving the equations for the system model. In this work, an approximate linear relationship between the tissue parameters and the eigenvalues of the instrument (to be used within the PLL system described in the next section) is

derived. Accordingly, the eigenvalue shifts can be measured by the feedback system, and the mechanical impedance can be calculated based on this approximation.

Assume that we have (3.23) for non-contact condition, and (3.24) when instrument touches a tissue, and note that the eigenvalues of the system are distinct.

$$H_0(\lambda, P) \triangleq |\lambda I - A(P)| \quad (3.23)$$

$$\begin{aligned} H(\lambda, P) &\triangleq |(\lambda + \Delta\lambda)I - (A(P) + \Delta A(P))| \\ &\approx H_0(\lambda, P) + \Delta H_0(\lambda, P) \end{aligned} \quad (3.24)$$

where $A(P)$ is the system's P -varying matrix in (3.6), λ is the eigenvalues of the system, and $P = \{p_i\}$ represents a vector of tissue parameters (e.g. mass m_m , spring rate k_m , and damping coefficient c_m).

Working at resonance modes, (3.23) and (3.24) are made equal to zero. Employing Taylor series, we also have,

$$\Delta H_{ik}^{(j)} \triangleq \left. \frac{\partial^j H_0}{\partial p_i^j} \right|_{\lambda_{k0}, P_0} \frac{(\Delta p_i)^j}{j!} \quad (3.25)$$

$$\Delta H_{\lambda_k}^{(j)} \triangleq \left. \frac{\partial^j H_0}{\partial \lambda^j} \right|_{\lambda_{k0}, P_0} \frac{(\Delta \lambda_k)^j}{j!} \quad (3.26)$$

thereby

$$\Delta H_0(\lambda, P) \approx \sum_j \Delta H_{\lambda_k}^{(j)} + \sum_j \sum_i \Delta H_{ik}^{(j)} \quad (3.27)$$

$$H = H_0 + \sum_j \Delta H_{\lambda_k}^{(j)} + \sum_j \sum_i \Delta H_{ik}^{(j)} = 0 \quad (3.28)$$

Although the generalized higher order approximation can be easily used, For small tissue parameters, a linear approximation of the error caused by the tissue parameters, and a 2nd order approximation of the error caused by the changes in eigenvalues proved to be the most both cost-efficient and accurate approximation by experimental

results. Therefore, we get,

$$b_{\lambda 1} \Delta \lambda_k + b_{\lambda 2} (\Delta \lambda_k)^2 = - \sum_i \Delta H_{ik}^{(1)}, \quad (3.29)$$

where

$$b_{\lambda 1} = \left. \frac{\partial H_0}{\partial \lambda} \right|_{\lambda_{k0}, P_0} \quad (3.30)$$

$$b_{\lambda 2} = \left. \frac{1}{2} \frac{\partial^2 H_0}{\partial \lambda^2} \right|_{\lambda_{k0}, P_0} \quad (3.31)$$

Solving at non-contact nominal condition for a VMM model by numerically calculating the partial differentiations, we get,

$$b_{\lambda 1} \Delta \lambda_k + b_{\lambda 2} (\Delta \lambda_k)^2 = b_{k1} \Delta k_m + b_{c1} \Delta c_m + b_{m1} \Delta m_m \quad (3.32)$$

$$b_{\lambda 1} \Delta \lambda_k + b_{\lambda 2} (\Delta \lambda_k)^2 = b_{k2} \Delta k_m + b_{c2} \Delta c_m + b_{m2} \Delta m_m, \quad (3.33)$$

where

$$b_{k1} = c_0 + c_1 i, \quad b_{c1} = -c_2 - c_3 i, \quad b_{m1} = c_4 - c_5 i,$$

$$b_{k2} = c_6 + c_7 i, \quad b_{c2} = -c_8 - c_9 i, \quad b_{m2} = c_{10} - c_{11} i,$$

and c_i is some positive real value. Assuming that the instrument is initially working at non-contact ($k_{m0} = c_{m0} = m_{m0} = 0$) and small change in the bandwidth of the resonance modes, we have

$$\Delta \lambda \approx -2\pi f_r \Delta \zeta_o + \Delta f_r \quad (3.34)$$

Replacing (3.34) into the linearized (3.32) and (3.33), the mechanical impedance of the tissue under indentation is linearly calculated. Also note that the eigenvalues

with a positive imaginary part have been taken into consideration. therefore,

$$2\pi f_{r1} \Delta \zeta_{o1} \approx c_2 c_m \quad (3.35)$$

$$2\pi f_{r2} \Delta \zeta_{o2} \approx c_8 c_m \quad (3.36)$$

$$\Delta f_{r1} \approx c_1 k_m - c_5 m_m \quad (3.37)$$

$$\Delta f_{r2} \approx c_7 k_m - c_{11} m_m \quad (3.38)$$

It should be noted that assuming $b_{\lambda 2} = 0$, a linear approximation is derived that should be equal to (2.15), while employing $b_{\lambda 2}$, equations (3.35)-(3.38) become 2nd-order.

3.3 Numerical considerations

3.3.1 Nominal tissue/phantom parameters

Unfortunately, there does not exist a complete and consistent set of parameters even for a basic soft tissue model. Most of the papers are only focused on the Young's modulus of the tissue, and do not provide any other information. Some of the studies work on extensive parameters, while other work on intensive parameters. It is also the case that the tissue model/parameters are affected by the pre-load, frequency, etc.

The goal of this research is to design a dynamic instrument to measure dynamic mechanical properties of biological soft tissues at specific frequencies. For that purpose, all tissue parameters including effective stiffness, mass, and damping, are needed. Moreover, to be able to design the lumped system parameters more efficiently, the nominal range of tissue extensive parameters is required. To be able to come up with nominal values of soft tissues/phantoms to be experimented, a study

has been made hereby to summarize the mechanical properties of soft materials.

Ottensmeyer et al. [16, 51, 87, 88] performed several tests on phantoms and living tissue. The samples are tested in MIT's ARES parallel plate rheometer standard measurement for polymer properties. The size of the samples and their density is available, so it possible to calculate the intensive and extensive properties of the tissues. The samples are tested from 0.1 Hz to 100 Hz. The calculated shear modulus increased at higher frequencies, which shows the complex behaviour of the samples. Kerdok et al. [61] provide information for in-vivo, ex-vivo perfused, ex-vivo post perfused, and in-vitro examination of porcine liver. TeMPeST 1-D is used to measure mechanical properties of tissues for small tissue deformation. A typical bode plot of compliance and phase versus frequency for an ex-vivo perfused test under a 24.7 mN preload (very low) is captured, shown in Fig. ??, and a Voigt model is fit to the data. A summary of the Voigt model parameters for small-strain frequency response is gathered by TeMPeST [16]. This summary suggests a stiffness range of 40 to 100 N/m, and damping constant of .1 to .6 Ns/m for liver tissue.

Ahn [89] has tested a phantom and an in-situ and in-vitro porcine liver using rounded and flat indenters with radius 3 and 10 mm. The relaxation test is performed on the tissues and the displacement-force curve is captured. Young's modulus of the tissue phantom is calculated as 5.63 and 6.24 kPa, providing that the measurement carried out by round indenters become bigger. The tests on porcine liver are performed using ramp, sine, and linear chirp wave, all under 2.5 Hz; this means the tissue will behave linearly elastic. The Young's modulus is then calculated as 8.32 and 9.51 kPa. The experiment with a linear chirp input displays stiffness values of 80 and 67 N/m. Finally, the relaxation profile is fit to a SLS model using a nonlinear mean square method.

Kassner et al. [66] chose the mechanical impedance of an extended Kelvin model as a measure of quality for INKOMAN's interface. A calibration is also carried out

to be able to measure tissue's mechanical impedance.

Brown et al. [82] and Rosen et al. [39] have also performed a set of in-vivo and in-situ studies using controlled endoscopic graspers. Calculated stress-strain data are fit to the exponential function below. The results of this study essentially illustrates that the elasticity of the biological soft tissues is nonlinear in respect to different indentation depths. There is also a big difference calculated between in-vivo and in-situ liver measurement. It is possible to estimate a Young's modulus based on specific strain values, and the parameters reflected in [82].

$$\sigma = \beta(e^{\alpha\epsilon} - 1) \quad (3.39)$$

Samur [20] estimates pig liver elastic modulus to be 10 – 15 kPa, while Kim estimated the Young modulus of pig liver about 3 kPa based on the semi-infinite medium assumption. Samur's work also gives an insight over the changes of elastic modulus for different indentation depths.

Sarvazyan et al. [67] indicates that the resonance frequency of human soft tissues mostly lies in a range of 3-5KHz.

Tay et al. [90] provided a soft tissue range of 5 – 25 kPa. Moreover, Based on the available literature [52, 67, 61, 91, 92, 90], cancerous tissues usually are 3 or 4 times stiffer than normal tissues. Other related data exist in [6, 27, 47, 48, 62, 93].

Based on the observed data, the elasticity of targeted soft tissues varies between 1 to 15 kPa, and the damping ratio is roughly below 0.2. The density of some soft tissues is roughly assumed to be around 1000 kg/m^3 which is that of water.

3.3.2 Numerical model analysis & system parameters optimization

Based on the study in the last section, the goal of this section is to optimize the instrument's sensitivity, precision and accuracy for the range of the mechanical properties of the targeted soft tissues. It is worth mentioning that the instrument also provides a high performance in high range of tissue stiffness values outside the targeted range.

The operating frequency range of the device is selected to approximately lie within 25 to 100 Hz. Firstly, based on the performed simulations based on the proposed system, as a rule of thumb, in order for the resonance of the instrument to be different in in-contact and non-contact conditions, the resonance frequencies of the instrument has to lie in a different range. By this hypothesis, the instrument should have either very small or very large resonance frequencies in comparison to the resonance frequencies of human soft tissues. At very high excitation frequencies, some tissues tend to act more like an elastic solid. Moreover, using a high-frequency resonator, e.g. [6], requires the tip mass of the instrument to be very small in order not to be influenced by the effect of the mass of the tissue for stiffness measurement. The magnitude of oscillations should, also, be very small not to damage the tissue under indentation. On the other hand, at very low frequencies, it is hard to filter out disturbances especially surgeon's hand tremor. The normal hand tremor is assumed to be less than 0.5 mm for a range of frequencies below 10 Hz [94]. The tip radius is selected to be 2.5 mm to minimize the amount of biological soft tissue damage resulting from contact stresses [95].

A number of criteria and constraints are used to select the value of the system parameters for best performance. The resonance frequency shifts should be big enough to be detectable by the feedback system, and the ratio of the frequency shifts to the resonance frequencies should be as high as possible. The relationship between Δf_{r1}

and the instrument's mass and spring parameters is shown in Fig. 3.4. The relationship between Δf_r and the tissue's mechanical impedance is also shown in Fig. 3.5. Moreover, fortunately, the resonance frequency shifts are almost linearly proportional to tissue stiffness.

Full phase information should be available for both resonance frequencies; i.e., the phase of the transfer functions of the system, $G_i(j\omega)$, should span R_ϕ , where,

$$R_\phi = \left(\angle G_i(j\omega_r) - \frac{\pi}{4}, \angle G_i(j\omega_r) + \frac{\pi}{4} \right), \quad (3.40)$$

and i represents either the first or second resonance of the system. The aforementioned conditions and criteria were fed into a Monte-Carlo algorithm to reach to a sub-optimal design.

3.3.3 Estimation of the viscous damping

One of the critical parameters of the instrument is the viscous damping coefficient. This damping factor influences the dynamic response of the system such that the phase corresponding to the resonance frequency changes. The general damping of the system also affects the amount of the displacement of the masses of the system. Therefore, bench-top experiments have been conducted to measure these factors in the springs. Fast Fourier Transform (FFT) method was used to find the total damping ratio of a second-order system, while the viscous and coulomb damping coefficients of the springs were separated in a time-domain analysis. The frequency-domain analysis is based on the measurement of the quality factor. For the time-domain analysis, the signal was filtered using a bandpass filter. The overlapping curve to the signal is derived, and fit to the following curve by linear least squares problem.

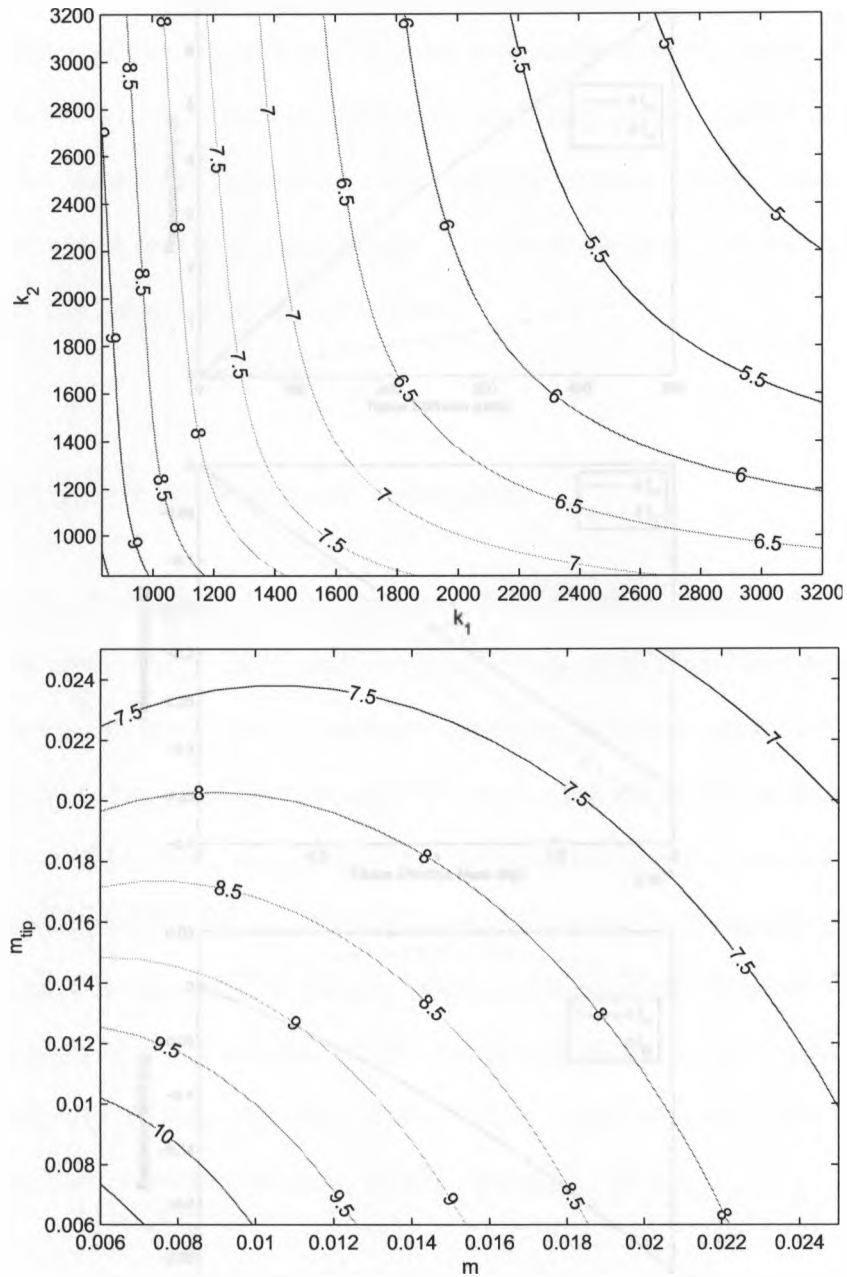


Figure 3.4: Contours of Δf_{r1} (Hz) with respect to the instrument's mass and spring parameters.

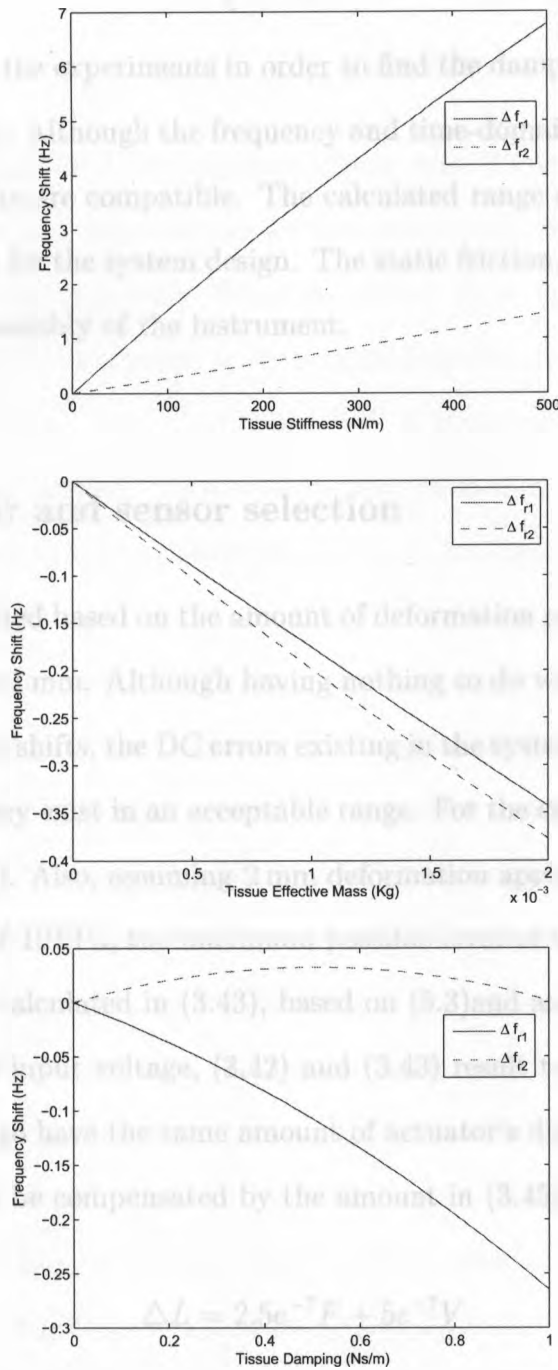


Figure 3.5: Plots of Δf_r with respect to parameters of a mechanical impedance load.

Parameter	Min	Max	Min	Max
Frequency Shift	0.000	0.000	0.000	0.000
Tissue Stiffness	0.000	500.0	0.000	0.000

$$F(x) = b_1 e^{b_2 x} + \begin{cases} b_3 x + b_4 & \text{if } b_3 x + b_4 > 0 \\ 0 & \text{if } b_3 x + b_4 < 0 \end{cases} \quad (3.41)$$

The summary of the experiments in order to find the damping ratio of the springs is shown in Table 3.1. Although the frequency and time-domain results are conducted separately, the results are compatible. The calculated range of the damping ratio is within desired range for the system design. The static friction, however, may increase depending on the assembly of the instrument.

3.3.4 Actuator and sensor selection

The actuator is selected based on the amount of deformation required at the tip mass, selected to be about 1 mm. Although having nothing to do with the principles of detecting the frequency shifts, the DC errors existing in the system have to be calculated to make sure that they exist in an acceptable range. For the chosen actuator, we have (3.42) based on (3.1). Also, assuming 2 mm deformation applied to a soft tissue with elasticity modulus of 10 kPa, the maximum possible error of the applied force on the actuator, ΔF_{max} is calculated in (3.43), based on (5.3) and assuming no friction. For the same amount of input voltage, (3.42) and (3.43) result to (3.44), which is negligible. Equivalently, to have the same amount of actuator's displacement, the applied input voltage has to be compensated by the amount in (3.45).

$$\Delta L = 2.5e^{-7}F + 5e^{-7}V \quad (3.42)$$

Table 3.1: Damping ratio results for 20 experiments

	Mean	SD	Min	Max
Frequency domain	0.025	0.003	0.0099	0.065
Time domain	0.032	0.005	0.0138	0.083

$$\Delta F_{max} = \frac{2 \times 2.5^{mm} \times 10^{kPa}}{0.75} 2^{mm} = 0.13 \text{ N} \quad (3.43)$$

$$\Delta L_{max} |_{\Delta V=0} = 32.5 \text{ nm} \quad (3.44)$$

$$\Delta V_{max} |_{\Delta L=constant} = 0.26 \text{ V} \quad (3.45)$$

A tissue deformation of 2 mm displaces the tip mass for about 0.2 mm. Moreover, in non-contact setup, the design allows for a maximum displacement of the tip mass of about 0.5 mm caused by gravity. When in-contact, these two displacements cancel each other. To keep the instrument in its original position, the maximum compensation input voltage, ΔV_{max} would be about 0.5 V. It should be emphasized that these DC components have nothing to do with the detection of the frequency shifts, and they are not required to be compensated as far as the displaced masses are still in the range of the LVDT's.

The displacement of each LVDT sensor must remain in the sensor's range. This displacement is affected by the actuator, the surgeon's hand when interacting with a tissue, and the force of gravity on the tip and proof mass. The selected sensors, Schaevitz 050-MHR, have a nominal linear displacement range of ± 1.27 mm, with a rated linearity of 0.5% of full scale. The phase and displacement characteristics of the system are mainly affected by the damping of the system, and depend on proper design and fabrication. Therefore, the system parameters are selected in a manner to ensure a satisfactory performance. Two signal conditioning modules, LDM-1000, are used to provide the AC input to the LVDT's and to demodulate their output. They provide analog bipolar voltage outputs with a range of ± 10 V. These modules function based on Amplitude Modulation (AM). Basically, the synchronized input and output of the LVDT are multiplied. The resulting signal is then low-pass filtered. In this case, a three-pole Butterworth low-pass filter with a cutoff frequency of 1000 Hz is used.

Chapter 4

Frequency Shift Detection

To drive the instrument at its resonance modes or near them, a fast and robust approach based on Phase-Locked Loop (PLL) is proposed. One of the most significant advantages of a PLL system is its noise rejection capabilities. A PLL is an example of a feedback system that satisfies a relationship between the phase of the generated and reference signals [54, 81]. A PLL is particularly a circuit which synchronizes an output signal with a reference input signal in frequency and in phase. When two signals are synchronized, it is said that the PLL is locked i.e. the phase error between the oscillator's output signal and the reference signal is zero or remains constant. If a phase error is adding up, a control system acts on a oscillator in such a way that the error is reduced to its minimum. In such a condition, the phase of the output signal is locked to the phase of the input signal. The PLL consists of three basic components:

1. A voltage-controlled oscillator (VCO)
2. A phase detector (PD)
3. A loop controller (LC) most commonly referred to as a loop filter.

The block diagram of a PLL system is shown in Fig. 4.1. Ideally, the VCO output's angular frequency shifts linearly proportional to the VCO input i.e. the LC output.

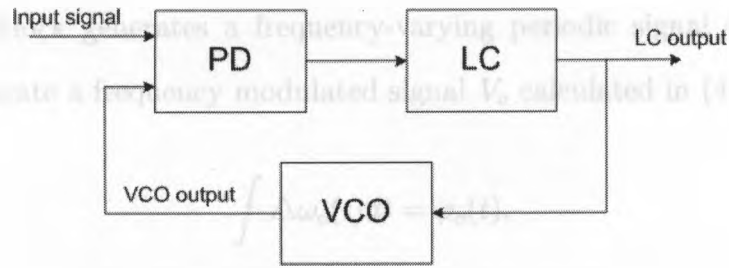


Figure 4.1: Block diagram of a PLL system.

The PD compares the phase of the input signal (reference) with the phase of the VCO output and provides an output signal whose magnitude is linearly proportional to the phase error. The DC component of the PD output, however, is practically of interest; hence the AC component is canceled using the loop filter. The loop filter (or better said loop controller for this case) is also used to improve the behavioral performance of the PLL.

As an example of how these blocks work together, assume that the angular frequency of the input signal is ω_0 the same as the initial (central) angular frequency of VCO, and the phase error is also zero. Note that, since the frequency shift in VCO is zero, LC output must be zero. Assume now that the frequency of the input signal increases. The phase of the input signal, then, starts leading the phase of the VCO output. Therefore, the phase error increases with time, so the PD output increases. The LC output will also increase (obviously LC introduces delay). This causes the VCO's angular frequency to increase. The phase error then becomes smaller as the the angular frequency of VCO increases. This process continues until the phase error reaches zero i.e. when the angular frequency of VCO equals that of the input signal. It should be noted that the amount of the settled phase error depends on the type of the PLL design and its parameters.

For further details on specific PLL designs refer to the literature [96, 97]. The section will continue to introduce the PLL system as the feedback for the proposed instrument.

The VCO block generates a frequency-varying periodic signal satisfying (4.1), which will generate a frequency modulated signal V_o calculated in (4.2).

$$\int \Delta\omega_o(t)dt = \varphi_o(t), \quad (4.1)$$

$$V_o(t) = \sin(\omega_o t + \int \Delta\omega_o(t)dt) = \sin((\omega_o + \Delta\omega_o)t + \varphi_{o0}) \quad (4.2)$$

where φ_o is the cumulative VCO phase lag caused by the frequency shift.

The PD block, which hereby also includes the corresponding averaging filtering, detects the phase difference, φ_e , between its two inputs, i.e., the average output, \bar{V}_d , is proportional to φ_e . Ideally, the relationship between \bar{V}_d and φ_e is linear, crossing the origin when $\varphi_e = 0$. The output of the PD unit usually contains an extra gain, K_d , where

$$\bar{V}_d = K_d \varphi_e \quad (4.3)$$

A common case of a PD unit resembles an exclusive OR (XOR) gate, which is used in this project with minor modifications. A sample result of an XOR gate calculated by (4.4) is shown in Fig. 4.2. As seen in the figure, the DC component of V_d is linearly proportional to the phase difference of the inputs of the PD block.

$$V_d(t) = V_1(t) \otimes V_2(t) \quad (4.4)$$

Another common PD is a multiplier in case the signals are sinusoidal. We have,

$$V_d(t) = V_1(t) \times V_2(t) \quad (4.5)$$

where

$$V_1(t) = \cos(\omega t),$$

$$V_2(t) = \sin(\omega t + \varphi_e)$$

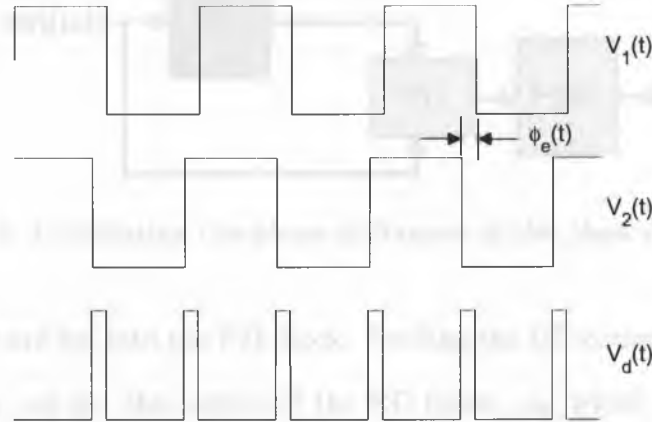


Figure 4.2: Output of an XOR gate.

We get,

$$V_d(t) = \cos(\omega t) \sin(\omega t + \varphi_e) \quad (4.6)$$

$$= \frac{\sin(2\omega t + \varphi_e) + \sin(\varphi_e)}{2} \quad (4.7)$$

After filtering the high-frequency component, we get,

$$\bar{V}_d(t) = \frac{1}{2} \sin(\varphi_e) \quad (4.8)$$

$$\bar{V}_d(t)|_{\varphi_e \approx 0} = \frac{1}{2} \varphi_e \quad (4.9)$$

so it is possible to introduce a linearized PD block for linear system analysis presented later in this and next sections.

Finally, the loop controller defines the type of the PLL and is also used as a compensator.

For the specific case studied in this project, consider the system in Fig. 4.3. Suppose that some sinusoidal input with some angular frequency is applied to the plant actuator, and the output of one of the sensors of the instrument and also the

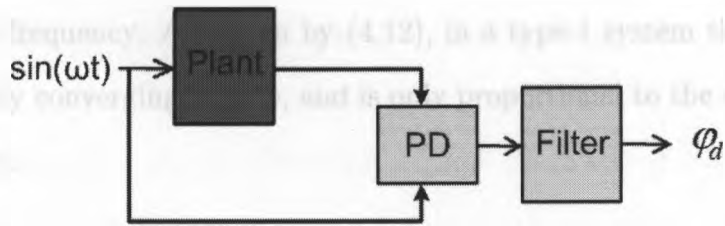


Figure 4.3: Calculating the phase difference of the plant's input/output.

input sine wave are fed into the PD block. Finding the DC component of the V_d using a low-pass filter, we get the output of the PD block, φ_d , which we assume equals φ_e with no loss of generality. If $\omega = \omega_r$, φ_d should converge to the desired angle, ϕ_d . Now assume that the plant suddenly changes behaviour (so that the resonance frequencies shift). We have,

$$\varphi_d|_{\omega=\omega_r^{new}} = \phi_d \quad (4.10)$$

$$\varphi_d|_{\omega=\omega_r^{old}} = \varphi_{d1} \quad (4.11)$$

where ω_r^{new} represents the new resonance frequency of the system, while ω_r^{old} represents the old one. Initially an input excited at ω_r^{old} is applied, which produces the output φ_{d1} from PD. Obviously, converging to ω_r^{new} , PD gives ϕ_d . The amount of phase for specific frequency variations can be, nevertheless, used in order to gain a better understanding of the system for designing the controller system parameters. Having φ_d and knowing that the output should converge to ϕ_d , we close the loop feeding back the phase difference output into the angular frequency applied to the instrument's input. For applying the change to the angular frequency of the input, Frequency Modulation (FM) is required where VCO plays its role.

The PLL-based feedback system for the proposed instrument is shown in Fig. 4.4. If the loop controller does not contain any poles at the origin, the PLL system is called type-1, while if there exists one pole at the origin, it is type-2. A type-2 PLL is required to obtain a zero-error response, while a type-1 PLL provides a phase that satisfies (4.12). Therefore, type-1 PLL can only be used to drive the system in a

near-resonance frequency. As shown by (4.12), in a type-1 system the error $\varphi_d - \phi_d$ is not necessarily converging to zero, and is only proportional to the variations of the input frequency.

$$\text{type - 1 PLL : } \varphi_d|_{f=(f_0+\Delta f)} \times K_o = \Delta f \quad (4.12)$$

$$\text{type - 2 PLL : } \varphi_d|_{f=f_r} = \phi_d, \quad (4.13)$$

where φ_d represents the output of Phase Difference detection unit, ϕ_d is the so-called resonance phase (i.e. the phase difference occurring at resonance), and K_o is the VCO gain.

For this application, the feedback system drives the device at its resonance frequency, near resonance, or the corresponding 3-dB frequencies in either non-contact or in-contact setups. The proposed method also ensures a smooth result and eliminates a risk of unexpected behaviour for the PLL system if one of the displacements gets out of the range of the sensor. For driving the system at its resonance frequency, it is required to set the phase of the system to the resonance phase which ideally happens when input/output signals are in quadrature. In order to capture the bandwidth of the system, the PLL needs to be compared with shifted phases corresponding to the frequencies that offer half-power. This is ideally achieved by considering $\pm \frac{\pi}{4}$ shifted phases around the resonance phase.

In order to obtain an optimized performance, the loop controller of PLL needs to be designed carefully. In order to filter out the disturbances in the system, including PLL and electronic noise and hand tremor of the user, high-pass and low-pass filters are incorporated before and after PD respectively. The most important filter in this system is the loop filter after PD. A second-order Butterworth filter with a cutoff frequency of 50 Hz has been used. It is worth mentioning that a first-order filter does not offer enough attenuation, while a third-order filter will make the system

unstable. The high-pass filters are Chebyshev Type I filters with a cutoff frequency of approximately 15 Hz. The signal conditioning module for LVDT sensors employs a three pole Butterworth low-pass filter with a cutoff frequency of 1000 Hz. This filter introduces extra phase lag to the system, while the high-pass filters and the actuation provide some phase lead. The set point can also be used and the VCO output can be filtered by an equivalent low-pass filter to compensate for these extra phase changes. The system is designed so that the shifts caused by these factors approximately cancel each other. Finally, a strong low-pass filter is used to thoroughly remove the ripples rendering the operating frequency (frequency demodulated signal).

The PLL system is first designed using open-loop setup based on observations on the system noise and the amount of phase difference caused by a frequency shift applied as a set point, and the response of the system in open-loop and closed-loop.

The proposed system can be simplified and linearized as shown in Fig. 4.5, where ρ is the set point, φ_e represents the phase difference between φ_p and φ_o (respectively, cumulative phase of the plant and VCO caused by the frequency shift), and $\Delta\omega = 2\pi\Delta f$ represents the frequency shift. K_d is the gain of PD block, and the PD block is a basic multiplier. $F(s)$ and $G_c(s)$, in the form of (4.14), represent the phase-detector filter and the loop controller respectively. K_φ is the linear representation of the relationship of the changes in the phase lag and the excitation angular frequency from a nominal point of the plant near its resonance frequency. This gain is only reliable near the resonance modes of the instrument, and changes value when working at different resonance modes and different damping ratios for the system when in-contact with a tissue. It should be considered that in this model, two internal loops in the system cancel each other, while this is not the case in the practical nonlinear system. Moreover, the response of the linearized system especially the transient response represents the response of the nonlinear system less accurately. Nevertheless,

the advantages of linear control theory can be used for the design process.

$$G_c(s) = \frac{1 + s\tau_2}{s\tau_1} \quad (4.14)$$

The linear and nonlinear design of the PLL system is continued in the next section accompanied by MATLAB/SIMULINK simulations.

Figure 4.10: A Simulink model of a PLL system with a lead-lag controller.



Figure 4.11: A Simulink model of a PLL system with a lead-lag controller.

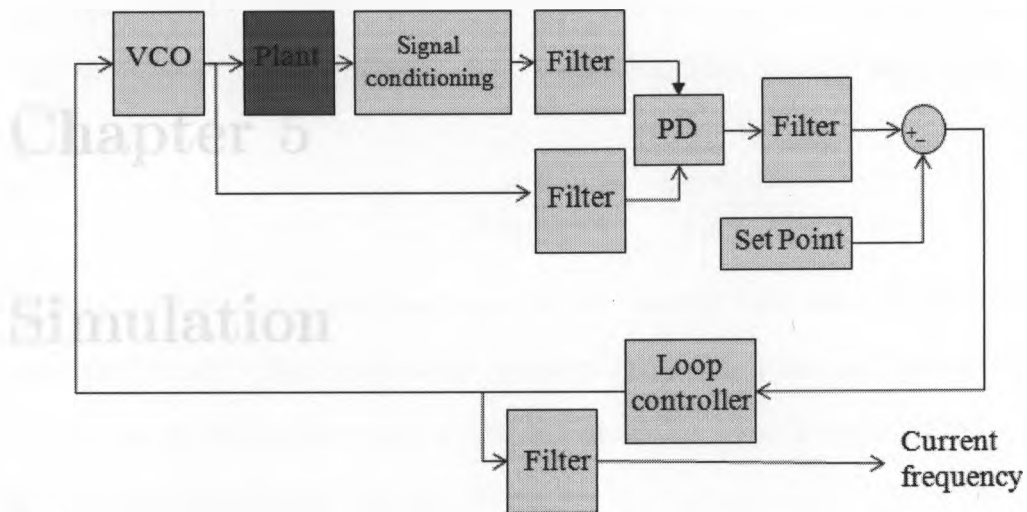


Figure 4.4: A nonlinear PLL-based feedback system for the proposed MIS instrument

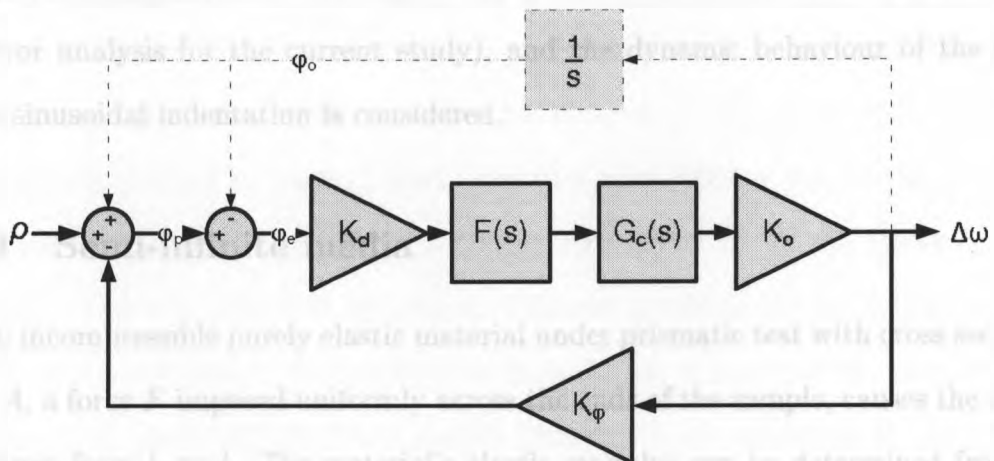


Figure 4.5: A simplified and linearized system model for the instrument

Chapter 5

Simulation

5.1 Finite element analysis

Previously, Young's modulus of the tissues under dynamic indentation held by a quasi-static ring has not been taken into consideration. In this section, an attempt is made to make sure that the modulus of the tissue in such condition would follow a specific pattern. For this purpose, the previous studies on the indentation of semi-infinite material, and also real tissues with specific boundary conditions is confirmed (as error analysis for the current study), and the dynamic behaviour of the tissue under sinusoidal indentation is considered.

5.1.1 Semi-infinite media

For an incompressible purely elastic material under prismatic test with cross sectional area, A , a force F imposed uniformly across the ends of the sample, causes the length to change from l_0 to l . The material's elastic modulus can be determined from the lumped spring constant and the known geometry as follows.

$$E = \frac{\sigma}{\varepsilon} = \frac{f/A}{\Delta l/l} = k \frac{l}{A} \quad (5.1)$$

This expression is valid for static deformations for a purely elastic material; however, it can be extended to the frequency domain through the correspondence principle [2]. The complex modulus is used for this purpose, but it is changed slightly so the aforementioned lumped stiffness and Young's modulus directly exist in the equation.

$$E^* = k \frac{l}{A} \frac{i\omega\tau_c + 1}{i\omega\tau_r + 1} = E \frac{i\omega\tau_c + 1}{i\omega\tau_r + 1} \quad (5.2)$$

Real biological tissues/phantoms do not usually take such convenient forms as presented above. They both have complex surface and internal geometries. Nevertheless, when one applies small deformations within a small region of the organ, some simplifying assumptions can still be made.

Assume there exists a finite deformable body, and it is deformed by an indenter. If the region of contact is magnified and the depth of indentation is reduced, the sample converges to a semi-infinite body, where the surface extends in all directions away from the contact point, and the material extends indefinitely below the surface.

A number of closed form relationships are provided for indenters of specific shape between the applied force, displacement, and material properties of the semi-infinite body. The derivation of these relationships incorporating a correction factor was first made by Hayes et al. [98], extended by Ming et al. [1] and Wellman [91], and is extensively studied in contact mechanics literature [99]. A few of the governing equations is provided in Table 5.1, with indenter radius a . In the aforementioned formulas, Poisson's ratio, ν is undefined. Different methods can be incorporated to exactly determine tissue's Poisson's ratio. Nonetheless, it has been shown to be very close to 0.5 in most biological soft tissues (incompressible material) [1, 16, 98]. In these solutions, the material is assumed to be homogeneous and isotropic. For normal indentation, uniform displacement in the normal direction and friction-free¹ contact

¹The environment inside body is very humid, and all of the tissue surfaces are slick, so a friction-free condition applies.

Table 5.1: Formulation of E for Indentation to semi-infinite bodies

Normal flat-ended cylindrical indenter (slip)	$E = \frac{(1-\nu^2)f}{2ax}$
Normal flat-ended cylindrical indenter (stick)	$E = \frac{(1+\nu)f}{2ax \ln \frac{3-4\nu}{1-2\nu}}$
Normal spherical indenter	$E = \frac{3f(1-\nu^2)}{4\sqrt{ax^3}}$
Tangential shear	$E = \frac{(2+\nu+\nu^2)f}{2\pi ax}$
Rotational shear	$E = \frac{3(1+\nu)\tau}{8a^3\theta}$

are assumed, so that sliding of tissue across the surface is permitted [16].

The aforementioned relationships correctly relate elastic modulus, force, and displacement parameters for a thin layer of tissue and small indentation. They fail to provide correct answers if tissue sample is small or deformations are large. The extended model also includes large deformations, essentially by adding a nonlinear correction factor. For a flat-ended cylindrical punch, we have [91],

$$f = \frac{2axE}{(1-\nu^2)} \kappa\left(\frac{a}{h}, \frac{x}{h}\right) \quad (5.3)$$

where

$$\kappa = \kappa_0\left(\nu, \frac{a}{h}\right) + \kappa_1\left(\nu, \frac{a}{h}\right) \frac{x}{h},$$

h is the thickness of sample, and κ_0 and κ_1 are given in [91].

Having the relationship between the applied force f , indentation depth x , and geometric-independent parameters, e.g. E , we can derive the equivalent geometric-dependent parameters by partial differentiation assuming a sinusoidal excitation. For

a flat-ended cylindrical tip, we have,

$$k_m = \frac{df}{dx} = \frac{2aE}{1 - \nu^2} \kappa \quad (5.4)$$

For a spring-mass system under flat-ended cylindrical indentation, we get [75],

$$m_m = \frac{\rho(\pi a^2)^{3/2}}{10(1 - \nu)} \quad (5.5)$$

where ρ is the density of the tissue under indentation².

5.1.2 Indentation of a semi-infinite medium

Finite element method is used to simulate some of the mechanical aspects of the proposed setup using ABAQUS. The behavior of the tissue under indentation and the frequency shifts of the instrument are investigated when a ring, which also touches the tissue, is present around the indenter. Four examples out of several configurations with cylindrical or spherical indenters, with/without a surrounding ring, and with different dimensions are shown in Fig. 5.1. It should be noted that when the ring is positioned closer to the indenter tip, the tissue behaves more ideally. These simulations are used to analyze the effect of a soft viscoelastic tissue (free and structured mesh types) on the resonance frequency shift of the instrument, and also to consider some nonlinear effects especially the fact that the instrument may not be in full-contact with the tissue.

In this study, Wellman's correction factors in both (5.3) and (5.4) are incorporated, and the tissue behavior is captured using FEM. It is verified that the calculations based on (5.3) and (5.4) using the same correction factor [98, 1, 91] matches. Several examples are provided in Table 5.2 noting that they are also compatible with Wellman [91].

²Wolf [100] calculates the effective mass of tissue, m_m different by a factor of 2.

When a surrounding ring is added, however, it is not possible to apply the same correction factors while only considering the indenter's radius. Obviously, the ring

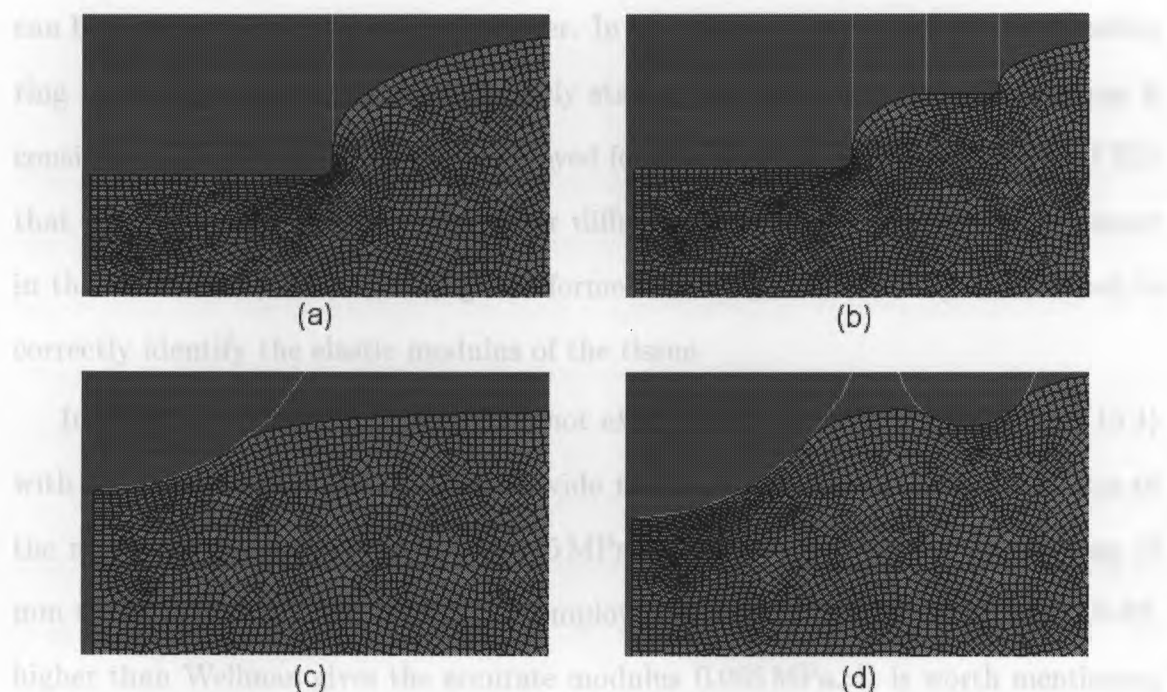


Figure 5.1: Mechanical simulations of applying an indenter on a soft viscoelastic tissue: (a) a cylindrical indenter (b) A cylindrical indenter with a surrounding ring (c) A spherical indenter (d) A spherical indenter with a rounded ring. (both structured and non-structured (shown here) tissue samples have been employed)

Table 5.2: Comparison of κ values for $\nu = 0.5$ obtained by the present model and the data of Ming et al [1].

a/h	Ming [1]		Current study	
	$x/h = 0.1\%$	$x/h = 10\%$	$x/h = 0.1\%$	$x/h = 10\%$
0.2	1.244	1.356	1.244	1.357
0.4	1.698	1.845	1.699	1.847
0.6	2.183	2.450	2.185	2.453

When a surrounding ring is added, however, it is not possible to apply the same correction factors while only considering the indenter's radius. Obviously, the ring can be interpreted as part of the indenter. In this paper, the effect of the surrounding ring moving through the tissue relatively statically while the indenter is oscillating is considered. The equation (5.4) is employed for this purpose. It is verified using FEM that (5.4) with a new correction factor different from [98, 1, 91] (16.8% difference in the tested case, where the ring is deformed the tissue for 0.2 mm) can be used to correctly identify the elastic modulus of the tissue.

In summary, assume the ring does not exist. It is verified using FEM that (5.4) with Wellman's correction factors, provide the pre-determined Young's modulus of the material very accurately (i.e. 0.005 MPa in this case). While when the ring (2 mm thick, indented 2 mm in tissue) is employed, (5.4) with a correction factor 16.8% higher than Wellman gives the accurate modulus 0.005 MPa. It is worth mentioning that the stiffness follows a sinusoidal pattern with the same frequency as applied by the indenter whose average is taken into consideration for the calculation of the Young's modulus. The sinusoidal stiffness for an elastic material has no phase lag to the displacement/force applied to the tissue. The periodic behavior of the tissue under excitation by a resonator is considered in Section 5.2.6.

Furthermore, the resonance frequency shifts have been calculated manually based on the output data from ABAQUS, and it is concluded that the instrument's resonance modes shift approximately linearly when in contact with a tissue in an approximately expected range based on MATLAB/SIMULINK simulations.

5.2 Lumped parameter system simulation

MATLAB/SIMULINK was used for simulation. The feedback-based simulations are also performed in LABVIEW RT, and later used for experiments by replacing the

state-space model of the instrument with the real instrument's input/output. In the next subsections, the lumped parameter system simulations are developed.

5.2.1 Open-loop instrument

The time response of the instrument to a sinusoidal input with a frequency equal to the instrument's resonance frequencies is shown in Fig. 5.2. It should be noted that, experimentally, the instrument's tip mass displacement, x_1 reaches a magnitude of up to 1 mm in non-contact, and that the displacements start to increase in time because of resonance.

The Bode plot of the outputs of the linearized time-invariant system in non-contact and also in-contact with a mechanical impedance is shown in Fig. 5.3. It is illustrated that the frequency response of the system changes because of the presence of the mechanical impedance of the soft tissue. These changes can then be used to determine the tissue parameters. Note that the first resonance occurs when displacements x_1 and x_2 are lagging a phase equal to $\frac{\pi}{2}$, and the second resonance occurs when displacements x_1 and x_2 are lagging a phase equal to $\frac{\pi}{2}$ and $\frac{3\pi}{2}$ (or $-\frac{\pi}{2}$) respectively.

5.2.2 Linear and nonlinear phased-locked loop

Assume a PLL system based on Fig. 4.1 with an ideal PD (i.e. $\varphi_d = \varphi_e$), and an ideal VCO with a transfer function defined by (5.6). Also assume that the loop controller is defined by (5.7). We can now construct a linear model for the PLL system. The closed-loop transfer function for a phase step input and a phase output (equivalently, frequency step input and a frequency output) is calculated by (5.8). The closed-loop transfer function for a phase step input and a frequency output is calculated by multiplying (5.8) by s as in (5.9). Sample responses for H_{CL1} and H_{CL2} are shown in Fig. 5.6 and 5.4. Fig. 5.4 shows that the PLL output, first compensates for the phase error, and then works at the same frequency as the input signal. Note that if

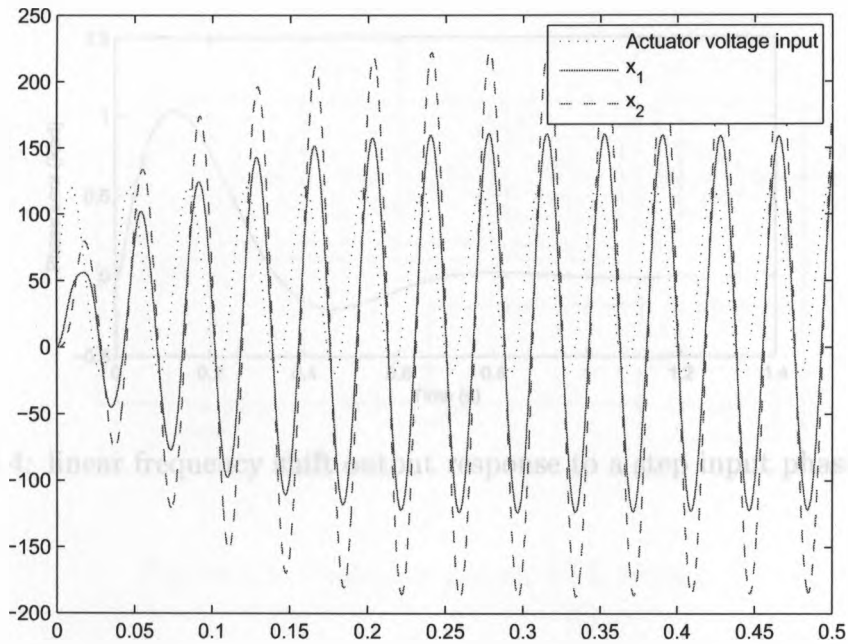


Figure 5.2: Response of the system (x_1 and x_2 measured in μm for a highly damped system) to sinusoidal input voltage. Sample the time-domain response applying a sinusoid with a frequency equal to the first resonance frequency.

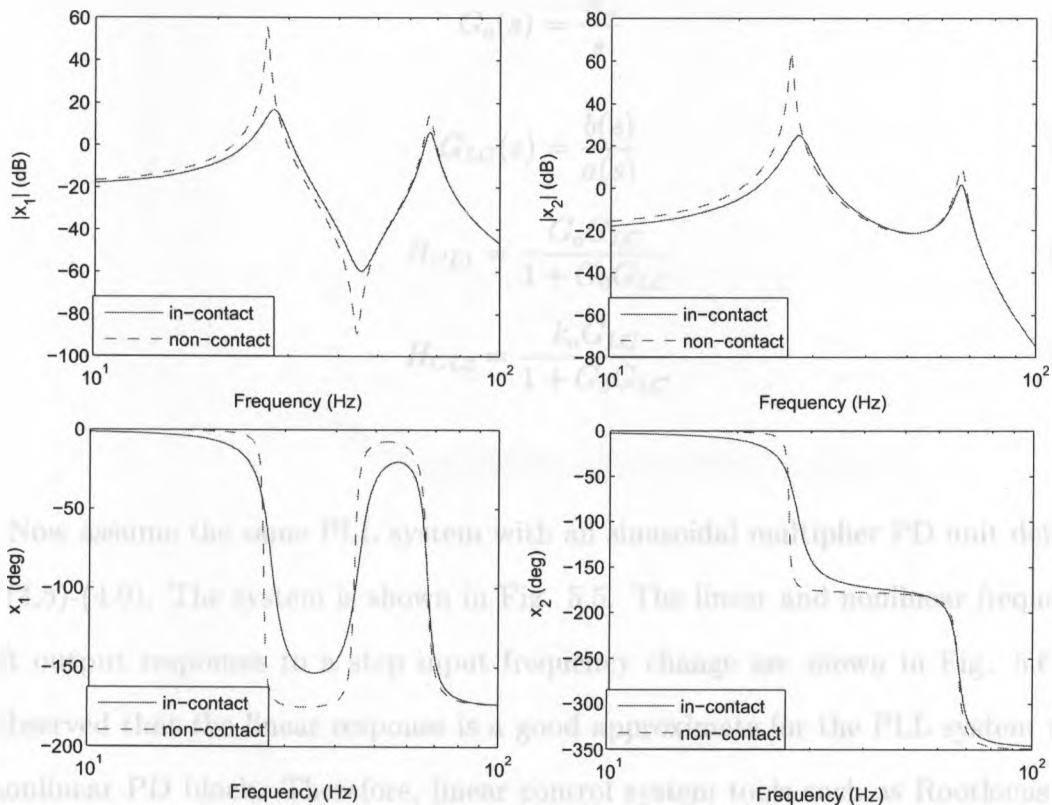


Figure 5.3: Bode plot of the system outputs with/without contacting a material with a mechanical impedance of $k_m = 70\text{N/m}$, $c_m = 0.5\text{N}\cdot\text{s/m}$ and $m_m = 0.02\text{g}$.

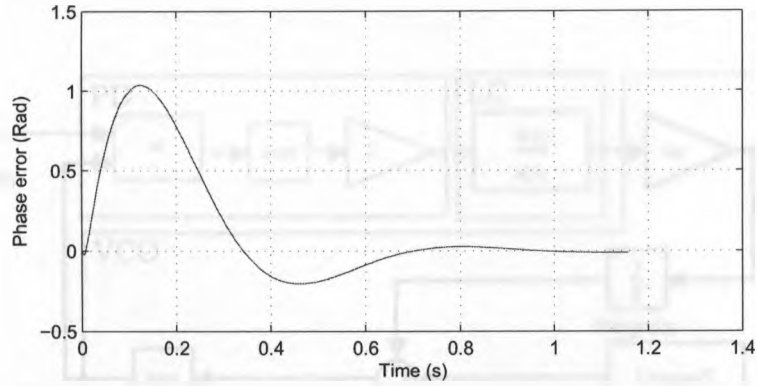


Figure 5.4: linear frequency shift output response to a step input phase change.

G_{LC} is a type-2 function, then the phase error reaches zero.

$$G_o(s) = \frac{K_o}{s} \quad (5.6)$$

$$G_{LC}(s) = \frac{b(s)}{a(s)} \quad (5.7)$$

$$H_{CL1} = \frac{G_o G_{LC}}{1 + G_o G_{LC}} \quad (5.8)$$

$$H_{CL2} = \frac{k_o G_{LC}}{1 + G_o G_{LC}} \quad (5.9)$$

Now assume the same PLL system with an sinusoidal multiplier PD unit defined by (4.5)-(4.9). The system is shown in Fig. 5.5. The linear and nonlinear frequency shift output responses to a step input frequency change are shown in Fig. 5.6. It is observed that the linear response is a good approximate for the PLL system with a nonlinear PD block. Therefore, linear control system tools such as Rootlocus (an example shown in Fig. 5.7) and bode diagrams can be used effectively for design purposes.

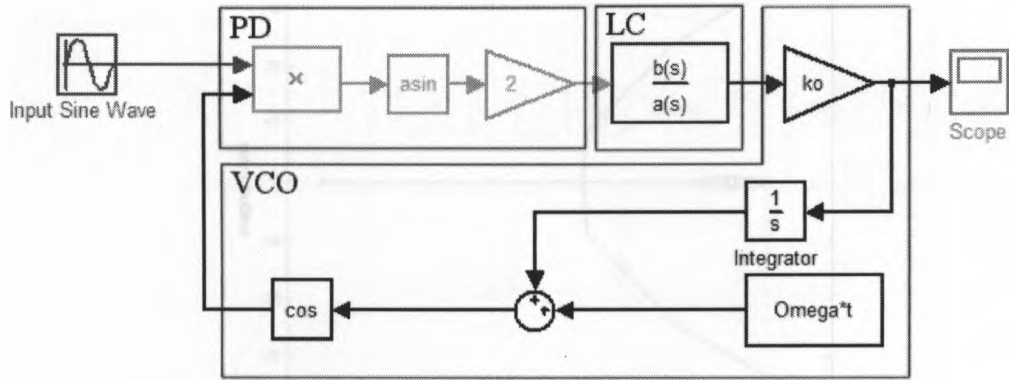


Figure 5.5: Nonlinear generic PLL system.

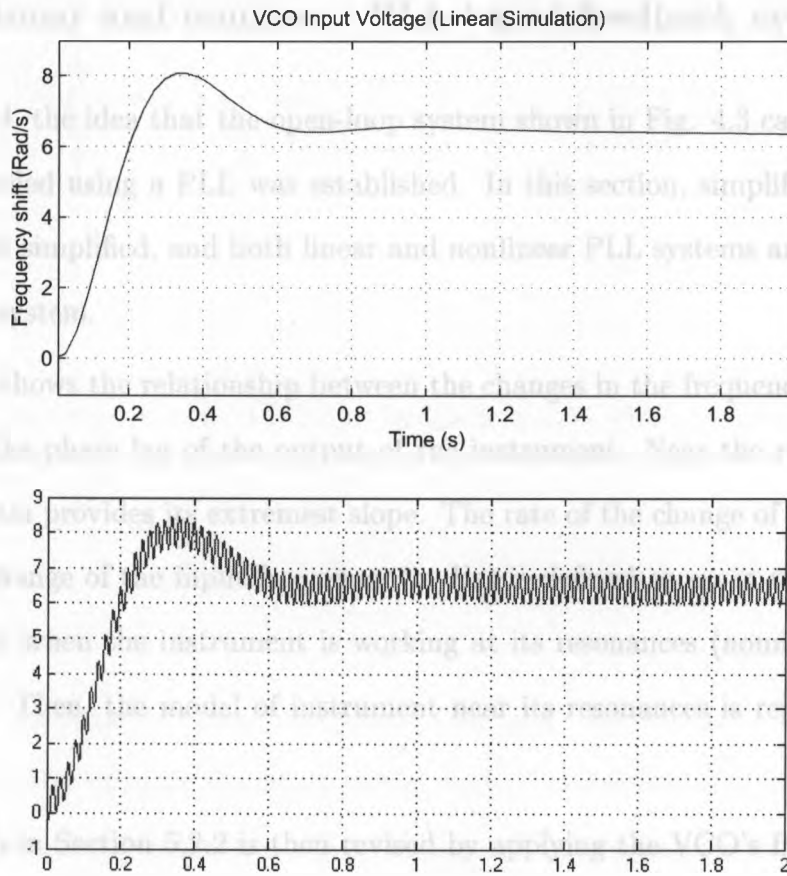


Figure 5.6: Linear (top) and nonlinear (bottom) frequency shift output response to a step input frequency change.

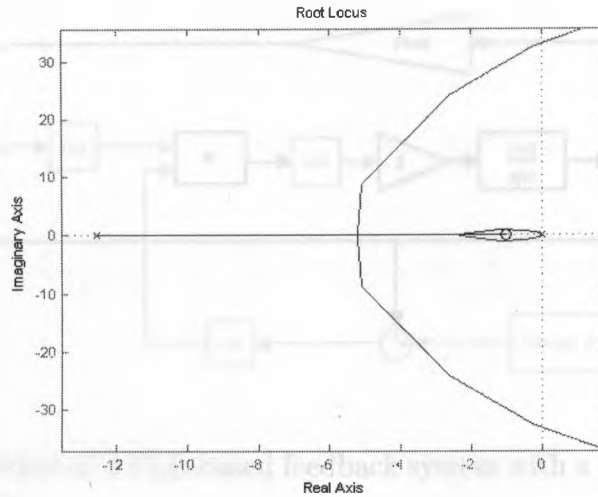


Figure 5.7: The critical area of the Rootlocus diagram for the linear system.

5.2.3 Linear and nonlinear PLL-based feedback system

In Chapter 4, the idea that the open-loop system shown in Fig. 4.3 can be automatically controlled using a PLL was established. In this section, simplify the diagram in Fig. 4.3 is simplified, and both linear and nonlinear PLL systems are employed to control the system.

Fig. 5.3 shows the relationship between the changes in the frequency of the input signal and the phase lag of the output of the instrument. Near the resonances, the phase diagram provides its extremest slope. The rate of the change of this phase lag, φ_d , to the change of the input frequency (in Hz) is defined as α_φ in terms of rad/s.Hz . Assume that when the instrument is working at its resonances (nominal point), α_φ is constant. Then, the model of instrument near its resonances is represented by a constant.

The PLL in Section 5.2.2 is then revised by applying the VCO's frequency shift, $\Delta\omega_o$ to the gain α_φ , and thereby approximating φ_d , where φ_d is added to the input's phase lag. An overview of this system is shown in Fig. 5.8. Assume that the integrators are both neglected as they are added to both input signals, as shown in Fig.5.9.

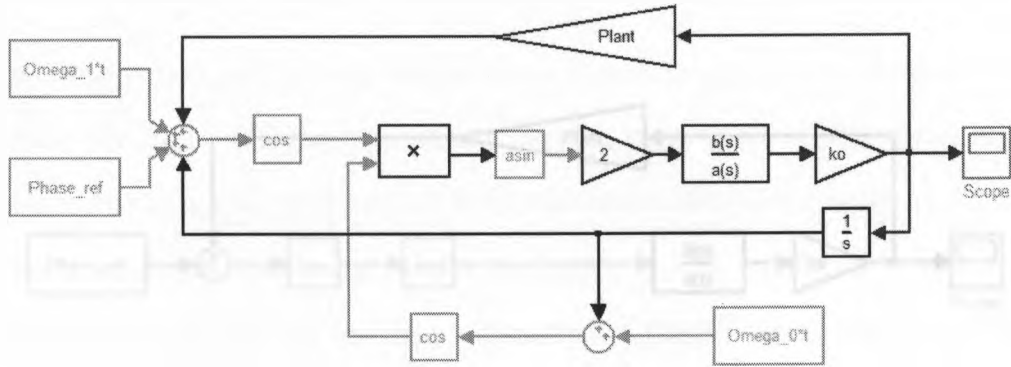


Figure 5.8: An overview of a PLL-based feedback system with a simplified instrument model as a constant.

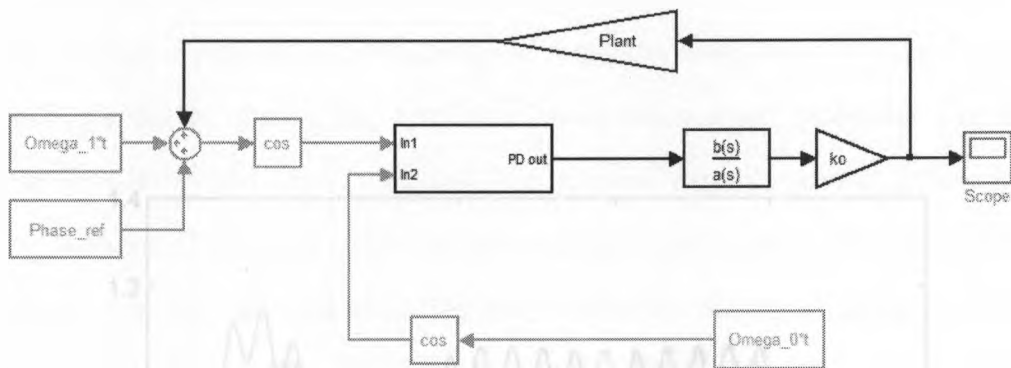


Figure 5.9: An overview of a PLL-based feedback system with a simplified instrument model as a constant and ignoring the integration component from both inputs.

Furthermore, the effect of the high-frequency signal carried by both input signals is neglected, shown in Fig. 5.10.

The step response of these three models and also the response captured by the linearized transfer function are shown in Fig. 5.11. It is observed that all the responses introduce the same steady-state value (average of the periodic signal for nonlinear ones). Also, the response of the system shown in Fig.5.9 introduces a slight amount of delay. The linearized responses, obviously, do not include the sinusoidal component. On the other hand, they are introducing more delay (worse response time).

5.2.3 Nonlinear Instrument and Linear Plant/Controller Linear

The nonlinear instrument is modeled in Simulink by the instrument block of Fig. 5.10. The plant is modeled by the plant block of Fig. 5.10. The gain K_0 is modeled by the gain block of Fig. 5.10. The scope block of Fig. 5.10 is used to observe the system response. The system is simulated using the Simulink software package. The system is simulated using the Simulink software package. The system is simulated using the Simulink software package.

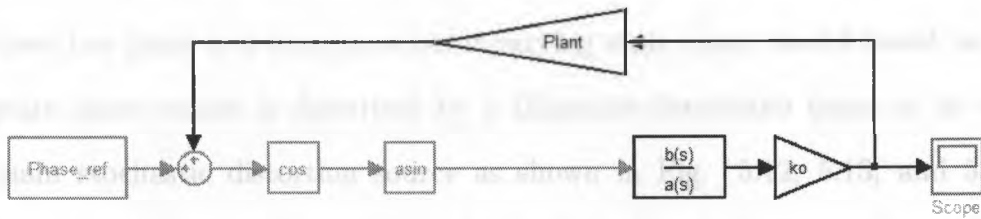


Figure 5.10: A linearized PLL-based feedback system with a simplified instrument model as a constant.

The nonlinear instrument is modeled in Simulink by the instrument block of Fig. 5.10. The plant is modeled by the plant block of Fig. 5.10. The gain K_0 is modeled by the gain block of Fig. 5.10. The scope block of Fig. 5.10 is used to observe the system response. The system is simulated using the Simulink software package.

The nonlinear instrument is modeled in Simulink by the instrument block of Fig. 5.10. The plant is modeled by the plant block of Fig. 5.10. The gain K_0 is modeled by the gain block of Fig. 5.10. The scope block of Fig. 5.10 is used to observe the system response. The system is simulated using the Simulink software package.

The nonlinear instrument is modeled in Simulink by the instrument block of Fig. 5.10. The plant is modeled by the plant block of Fig. 5.10. The gain K_0 is modeled by the gain block of Fig. 5.10. The scope block of Fig. 5.10 is used to observe the system response. The system is simulated using the Simulink software package.

The nonlinear instrument is modeled in Simulink by the instrument block of Fig. 5.10. The plant is modeled by the plant block of Fig. 5.10. The gain K_0 is modeled by the gain block of Fig. 5.10. The scope block of Fig. 5.10 is used to observe the system response. The system is simulated using the Simulink software package.

The nonlinear instrument is modeled in Simulink by the instrument block of Fig. 5.10. The plant is modeled by the plant block of Fig. 5.10. The gain K_0 is modeled by the gain block of Fig. 5.10. The scope block of Fig. 5.10 is used to observe the system response. The system is simulated using the Simulink software package.

The nonlinear instrument is modeled in Simulink by the instrument block of Fig. 5.10. The plant is modeled by the plant block of Fig. 5.10. The gain K_0 is modeled by the gain block of Fig. 5.10. The scope block of Fig. 5.10 is used to observe the system response. The system is simulated using the Simulink software package.

The nonlinear instrument is modeled in Simulink by the instrument block of Fig. 5.10. The plant is modeled by the plant block of Fig. 5.10. The gain K_0 is modeled by the gain block of Fig. 5.10. The scope block of Fig. 5.10 is used to observe the system response. The system is simulated using the Simulink software package.

The nonlinear instrument is modeled in Simulink by the instrument block of Fig. 5.10. The plant is modeled by the plant block of Fig. 5.10. The gain K_0 is modeled by the gain block of Fig. 5.10. The scope block of Fig. 5.10 is used to observe the system response. The system is simulated using the Simulink software package.

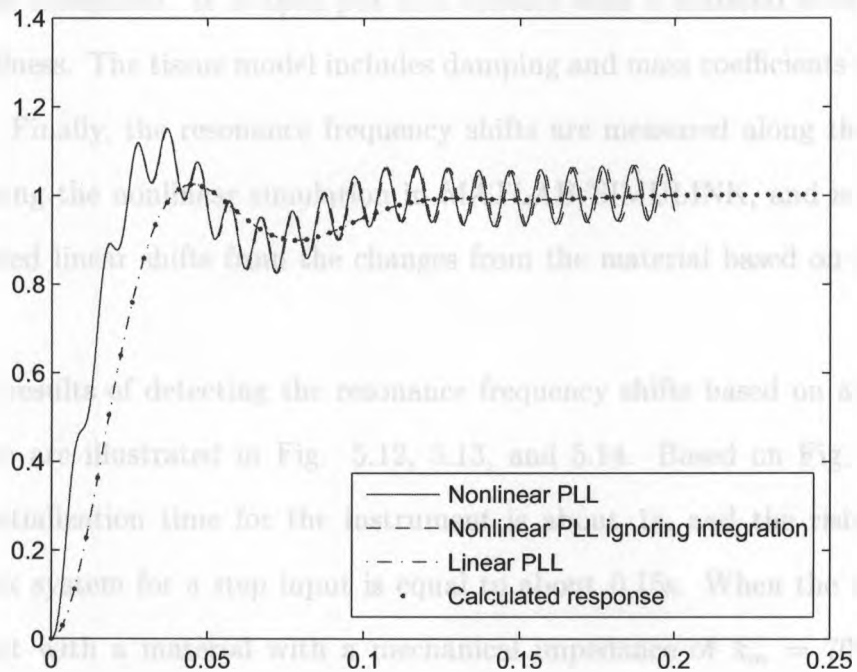


Figure 5.11: Step response of nonlinear and linear PLL-based feedback systems.

5.2.4 Nonlinear instrument and linear time-varying tissue

The nonlinear feedback system simulation is based on the schematic shown in Fig. 4.4 where the plant is a time/parameter-varying state space model based on (3.6). The state space model is disturbed by a Gaussian-distributed noise at its output (the main stochastic distortion source as shown in Fig. 5.12, 5.13, and 5.14), a simulated hand tremor low-frequency disturbance (highly disturbing if not filtered properly), various present constant disturbances, e.g. gravity, and irregularities over the mechanical parameters of the material under investigation (time-varying tissue parameters). LVDT conditioning modules are simulated by an AM modulation and a low-pass filter. The outputs of the sensors are also saturated and quantized.

The resonance frequency shift is detected using the simulated PLL-based nonlinear feedback system by moving the simulated probe along a soft material. The instrument is first initialized. It is then put into contact with a material with a defined varying stiffness. The tissue model includes damping and mass coefficients with small variations. Finally, the resonance frequency shifts are measured along the modeled material using the nonlinear simulation in MATLAB/SIMULINK, and is compared with expected linear shifts from the changes from the material based on (3.32) and (3.33).

Sample results of detecting the resonance frequency shifts based on a simulated PLL system are illustrated in Fig. 5.12, 5.13, and 5.14. Based on Fig. 5.12, the required initialization time for the instrument is about 1s, and the rising time of the feedback system for a step input is equal to about 0.15s. When the instrument is in contact with a material with a mechanical impedance of $k_m = 70\text{N/m}$, $c_m = 0.2\text{N}\cdot\text{s/m}$ and $m_m = 0.02\text{g}$, the first and second resonance frequencies change about 4% and 0.75% respectively. The resolution of the feedback system, however, is much better. Therefore, the frequency shifts in the instrument can be detected both fast and accurately, and it can be used to detect the mechanical impedance of the tissue

under indentation.

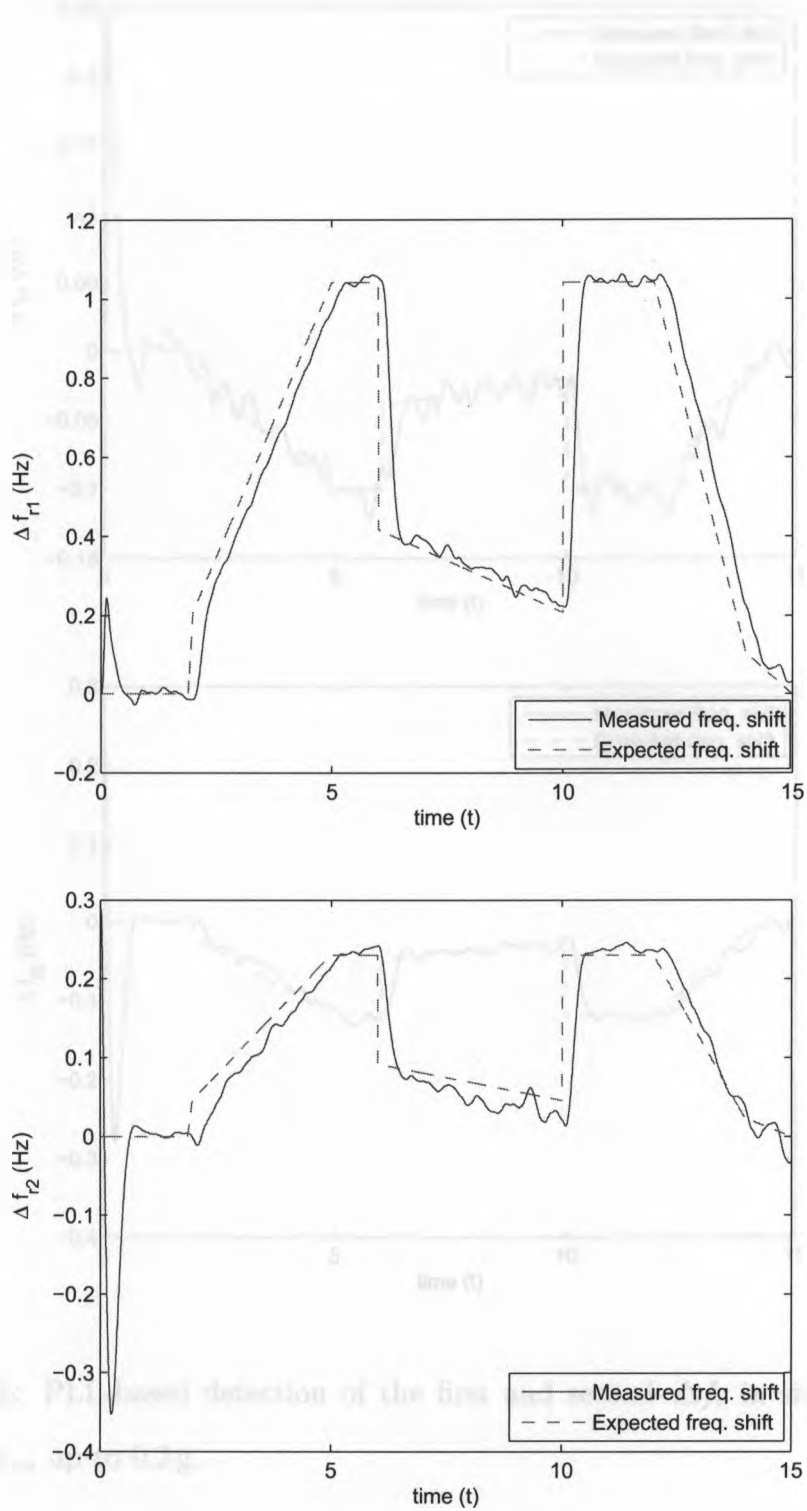


Figure 5.12: PLL-based detection of the first and second Δf_r in simulation while changing k_m up to 70 N/m .

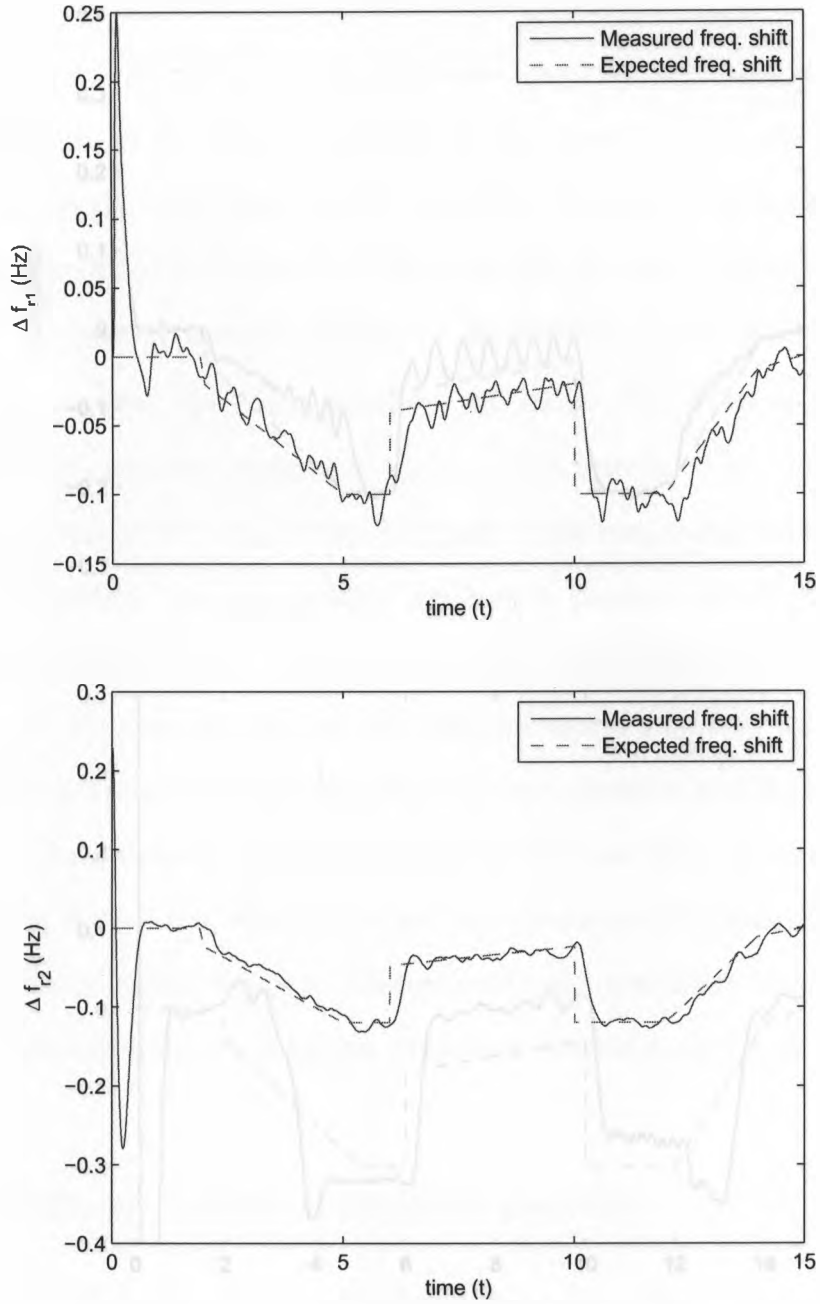


Figure 5.13: PLL-based detection of the first and second Δf_r in simulation while changing m_m up to 0.2 g.

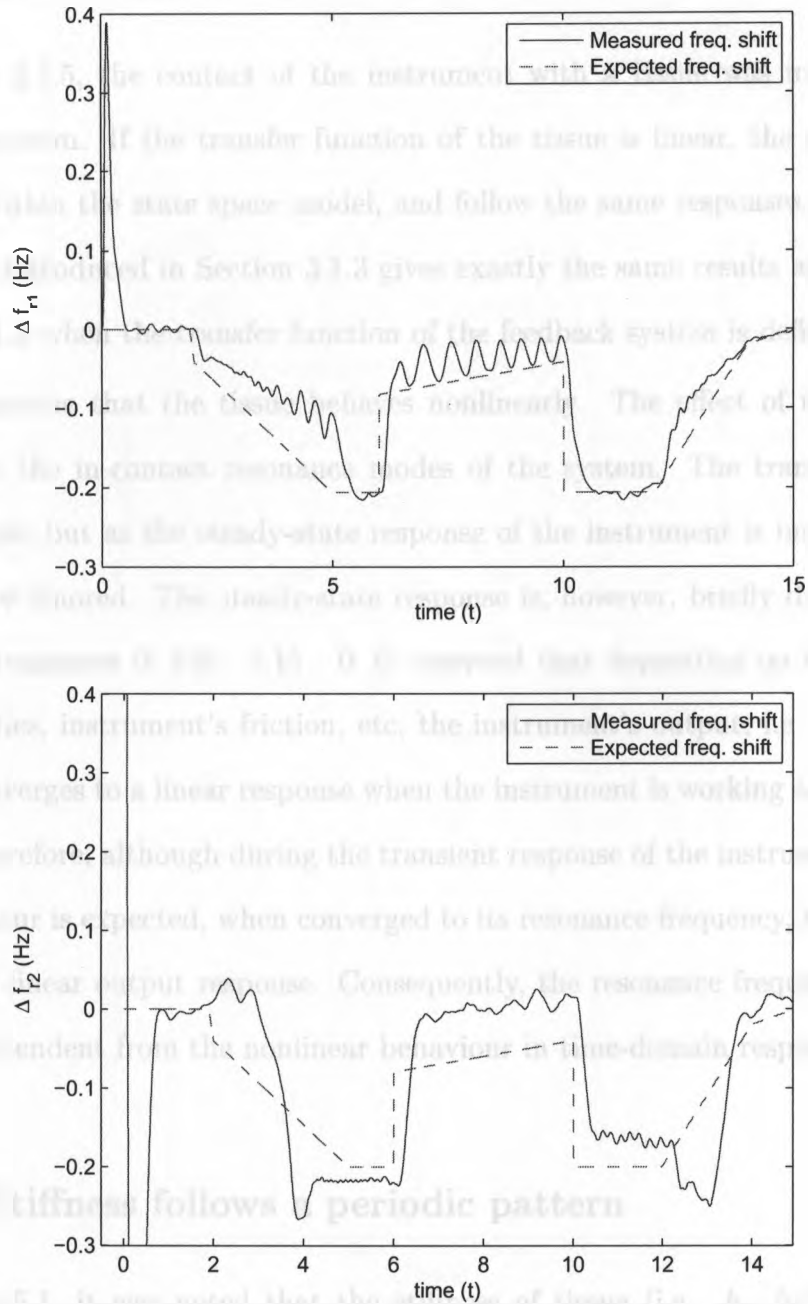


Figure 5.14: PLL-based detection of the first and second Δf_r in simulation while changing c_m up to 0.2 Ns/m .

5.2.5 Tissue dynamic contact as a nonlinear behaviour

In Section 3.1.5, the contact of the instrument with a tissue was introduced as a feedback system. If the transfer function of the tissue is linear, the system can be modeled within the state space model, and follow the same responses. For example, the model introduced in Section 3.1.3 gives exactly the same results as the model in Section 3.1.5 when the transfer function of the feedback system is defined for VMM.

Now assume that the tissue behaves nonlinearly. The effect of the nonlinearities affects the in-contact resonance modes of the system. The transient response also changes, but as the steady-state response of the instrument is important, those changes are ignored. The steady-state response is, however, briefly discussed. Consider the responses in Fig. 5.15. It is observed that depending on the amount of nonlinearities, instrument's friction, etc, the instrument's output, i.e. x_2 in this example, converges to a linear response when the instrument is working at its resonance mode. Therefore, although during the transient response of the instrument, a nonlinear behaviour is expected, when converged to its resonance frequency, the instrument provides a linear output response. Consequently, the resonance frequencies are captured independent from the nonlinear behaviour in time-domain response.

5.2.6 Stiffness follows a periodic pattern

In Section 5.1, it was noted that the stiffness of tissue (i.e. k_m for a mechanical impedance) changes periodically with the same frequency of the oscillations applied to the tissue. The output frequency shift detection in simulation is introduced in Section 5.2.4 for time-varying tissue parameters, k_m , m_m , and c_m which have been varying during the process just like the tissue is changing behaviour. These variations could cause a shift in the resonance frequency, and this shift was desirable because it was connected to the behaviour of the tissue. Now, note that although the Young's

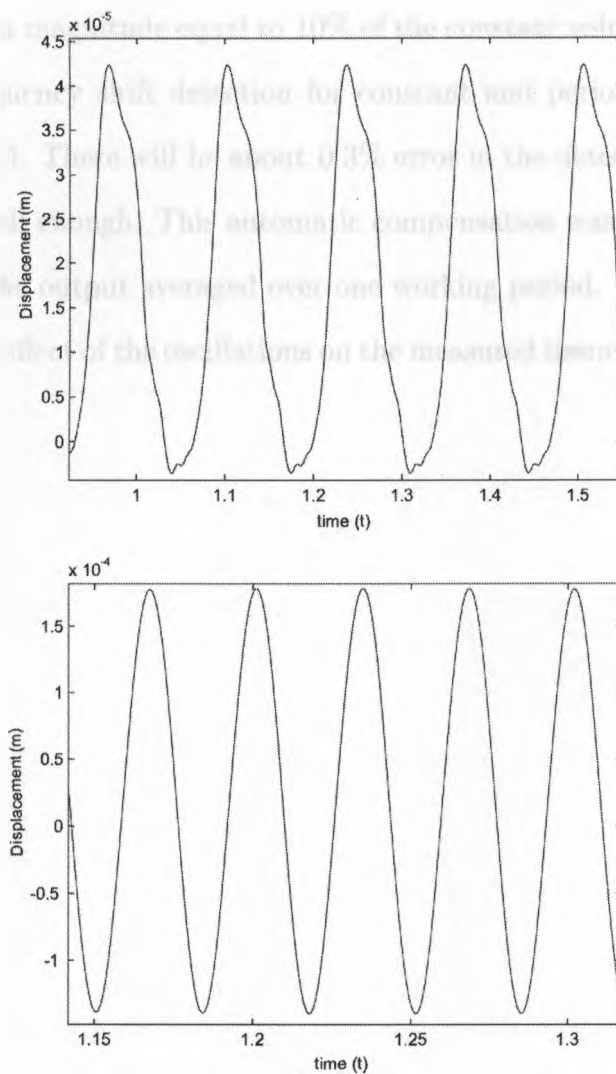


Figure 5.15: The x_2 output of the instrument in-contact with a nonlinear tissue when a sinusoidal input is applied to the actuator. (left) response when working at a frequency far enough from the resonance. (right) response when working at resonance.

modulus of the tissue is kept constant, k_m will introduce slight oscillations with the same period as the instrument's oscillation (based on ABAQUS results). These oscillations are part of the behaviour of the instrument and not the tissue, so in this case a change in the detection of the frequency shifts is undesirable. A sinusoidal signal added to k_m with a magnitude equal to 10% of the constant value of k_m is considered. The result of frequency shift detection for constant and periodic stiffness values is shown in Fig. 5.2.6. There will be about 0.3% error in the detection of the frequency shift, which is small enough. This automatic compensation was expected as the PLL system provides the output averaged over one working period.

Therefore, the effect of the oscillations on the measured tissue stiffness is negligible.



Figure 5.2.6. Frequency shift detection for constant and periodic stiffness values. (Left: Full wave (100Hz) sinusoidal.

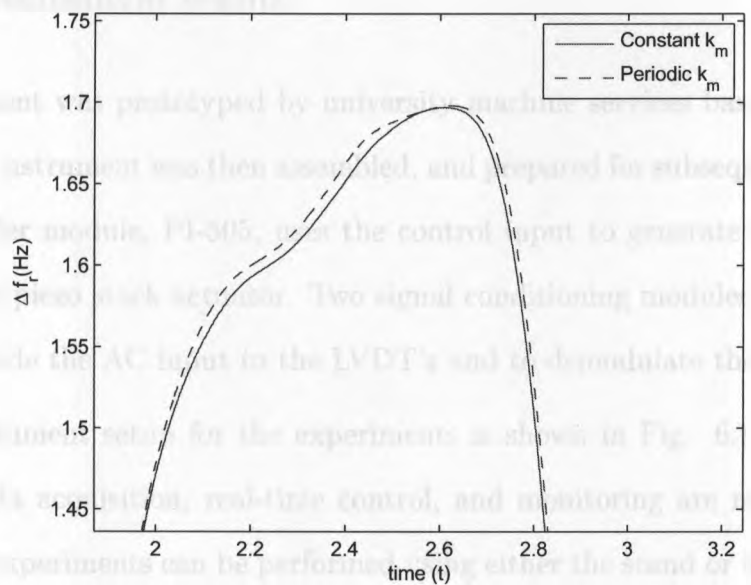
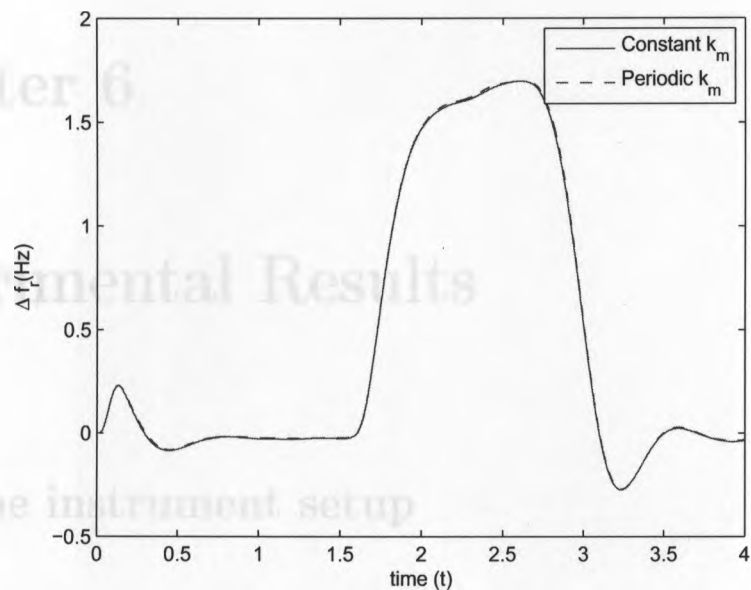


Figure 5.16: Frequency shift detection error for a periodic tissue stiffness value. (Left) full view (right) zoomed-in

Chapter 6

Experimental Results

6.1 The instrument setup

6.1.1 Mechanical setup

The instrument was prototyped by university machine services based on the design layout. The instrument was then assembled, and prepared for subsequent testing. The piezo amplifier module, PI-505, uses the control input to generate the high-voltage input for the piezo stack actuator. Two signal conditioning modules, LDM-1000, are used to provide the AC input to the LVDT's and to demodulate their output.

The instrument setup for the experiments is shown in Fig. 6.1. Extra components for data acquisition, real-time control, and monitoring are not shown in this figure. The experiments can be performed using either the stand or by hand. Experiments using the stand, however, provide better precision. In order to capture reliable calibration and measurement data, the instrument has to be mounted on a stand. The instrument is also tested by being held in hand when employing the PLL-based method. All the final results are based on experiments performed using the stand for the consistency of results unless otherwise stated.

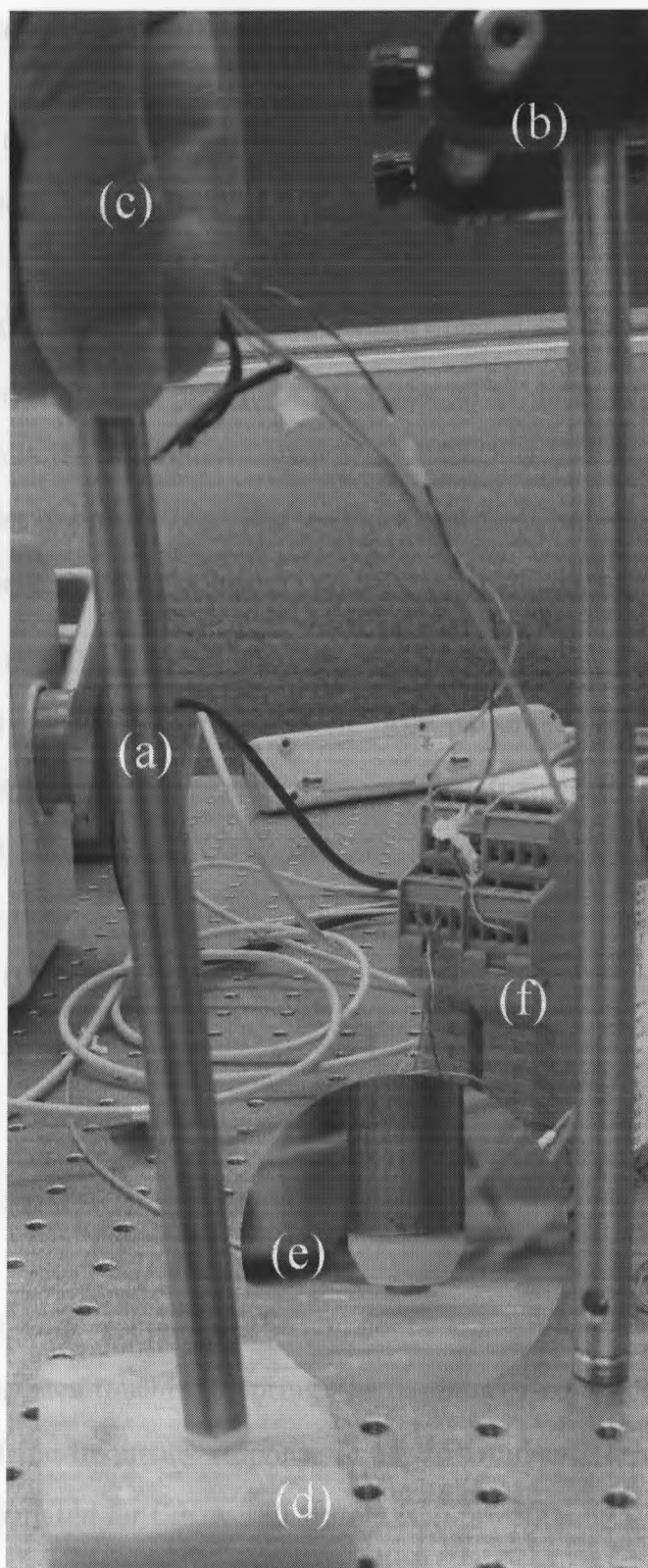


Figure 6.1: Instrument setup: (a) the proposed instrument (b) the stand used for the experiments (c) performing an experiment by hand (d) sample under experiment (e) the sample, the tip, and the surrounding ring are shown (f) conditioning modules

6.1.2 Control and monitoring

NI LABVIEW is used for capturing the outputs of the instrument and generating the control input. The software design of the system and the controller are implemented using LABVIEW Real-Time based on Fig. 4.4 using a continuous communication architecture. In this mode, two loops have been created for deterministic (high priority) and non-deterministic (low priority) tasks. The deterministic loop includes the controller, while the non-deterministic loop is used as user interface between the target and the host desktop PC's. The feedback system is implemented according to Fig. 4.4 inside the deterministic loop.

The system is monitored from the host system based on the data gathered from the non-deterministic loop of the target system. Any parameter involved in the system design can be shown such as resonance frequencies, frequency shifts, phase errors, and displacement magnitudes. Obviously, the main goal of the monitoring system is to provide the resonance frequency shifts to the surgeon as a good measure for evaluating tissue stiffness.

6.2 Non-contact instrument

The acquired frequency response of the non-contact instrument is also shown in Fig. 6.4. It can be seen when touching a spring, the resonance frequencies shift. Measuring the bandwidth of the frequency response of the instrument, the mean value of the damping ratio calculated for the overall system is approximately 0.043 about the first resonance mode and 0.018 about the second resonance mode. The calculated range of the damping ratio is within the desired range and is in harmony with the preliminary results in Section 3.3.3.

Table 6.1: Experimental validation of mass measurements

M (kg)	Δf_{r1} (Hz)	$M _{\Delta f_{r1}}$ (N/m)	Δf_{r2} (Hz)	$M _{\Delta f_{r2}}$ (N/m)
3.30E-05	-0.015	2.90E-05	-0.020	3.50E-05
6.10E-05	-0.040	7.73E-05	-0.045	7.86E-05
8.70E-05	-0.065	1.26E-04	-0.080	1.40E-04
1.54E-04	-0.090	1.74E-04	-0.085	1.48E-04
2.27E-04	-0.110	2.12E-04	-0.145	2.52E-04
2.48E-04	-0.140	2.70E-04	-0.145	2.52E-04

6.3 Validation

6.3.1 Validation of mass measurements

A number of random reference masses are used to measure the resonance frequency shifts, and thereby estimating the employed mass based on (3.32) and (3.33). The masses are also measured using a digital analytical balance.

A summary of the results is shown in Table 6.1. The measured mass values by the analytical balance and also the proposed instrument are shown in Fig. 6.2 where a linear model crossing the origin is fit to the data. The high R^2 values represent the high precision of the estimation, while for all cases, the frequency shift detection introduces sinusoidal ripples and stochastic disturbances varying about 0.02 Hz. The measured resonance values presented as results are, however, the mean values. According to the linear calibration formula, the error in determining the attached mass is about 8% and 6% employing the 1st and 2nd resonance frequency shift detection respectively.

6.3.2 Validation of stiffness measurements

Cantilever beams are used to evaluate the performance of the instrument in estimating the stiffness of the beams. For this purpose, consider aluminum cantilever beams with

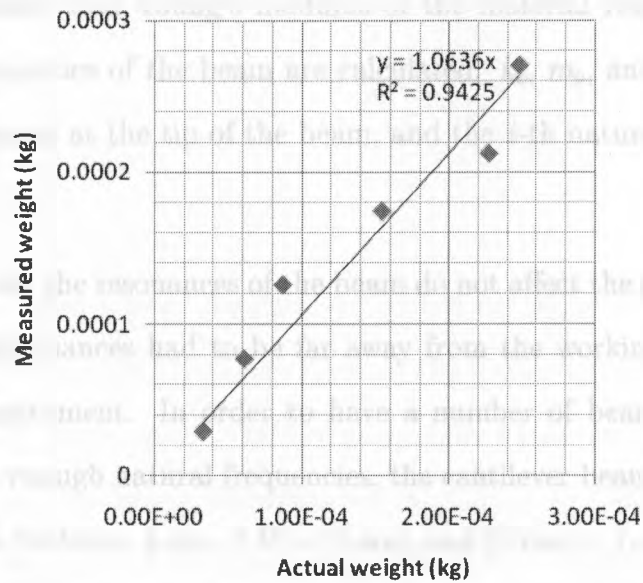
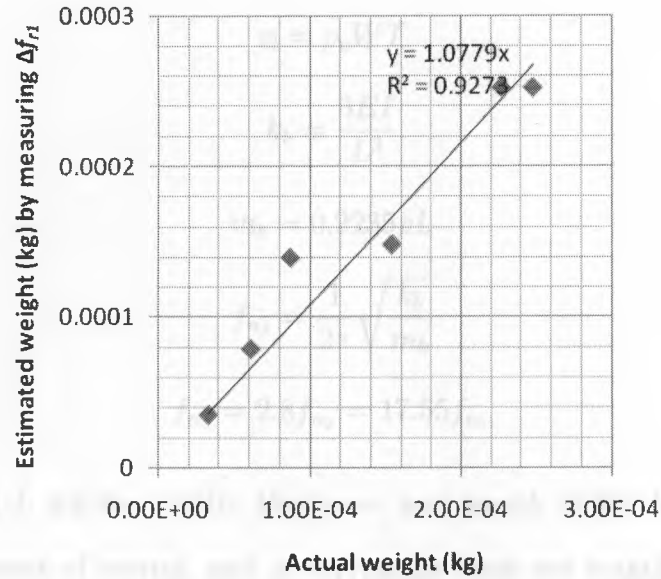


Figure 6.2: Experimental validation of mass measurements

uniform cross section. We have [101],

$$I = \frac{WT^3}{12} \quad (6.1)$$

$$\rho_l = \rho_v WT \quad (6.2)$$

$$k_b = \frac{3EI}{L^3} \quad (6.3)$$

$$m_b = 0.2235\rho_l L \quad (6.4)$$

$$f_{n_1} = \frac{1}{2\pi} \sqrt{\frac{k_b}{m_b}} \quad (6.5)$$

$$f_{n_3} = 2.8f_{n_2} = 17.55f_{n_1} \quad (6.6)$$

where W , T , and L are the width, thickness, and length of the beam respectively. I is the area moment of inertia, and ρ_l represents mass per length of the beam. ρ_v and E are the density and Young's modulus of the material respectively. Finally, the mechanical properties of the beam are calculated: k_b , m_b , and f_{n_i} represent the stiffness, effective mass at the tip of the beam, and the i -th natural frequency of the beam.

To be certain that the resonances of the beam do not affect the calculated stiffness of the beam, the resonances had to be far away from the working frequency range of the proposed instrument. In order to have a number of beams with small m_b , proper k_b and high enough natural frequencies, the cantilever beams have to be quite small-size, i.e. $T = 0.43$ mm, 4 mm $< W < 5$ mm, and 25 mm $< L < 72$ mm. Some of the beams are also tested using a dynamic mechanical analyser at the first resonance frequency.

The numerical values of the calculations and measurements performed on the cantilever beams using the 2nd order approximation (3.32) and (3.33) are shown in Table 6.3. The calculated and measured stiffness values are shown in Fig. 6.3 where a linear

Table 6.2: Experimental validation of stiffness measurement using cantilever beams

$k_b^{(N/m)}$	m_b (kg)	$f_{n_1}^{(Hz)}$	$\Delta f_{r1}^{(Hz)}$	$k_b _{\Delta f_{r1}}^{(N/m)}$	$\Delta f_{r2}^{(Hz)}$	$k_b _{\Delta f_{r2}}^{(N/m)}$
15.37	7.59E-05	71.62	0.17	14.73	-0.05	-3.47
32.14	5.93E-05	117.09	0.43	29.43	0.09	34.16
37.55	5.63E-05	129.96	0.96	61.50	0.10	36.58
46.55	6.14E-05	138.49	1.16	74.07	0.12	43.03
51.97	5.05E-05	161.42	1.21	76.49	0.15	50.04
69.06	5.39E-05	180.13	1.46	92.11	0.21	67.66
70.50	4.56E-05	197.68	1.07	67.61	0.11	37.92
78.76	4.39E-05	212.96	1.31	82.26	0.16	51.96
80.64	5.11E-05	199.74	1.61	101.24	0.25	78.70
99.98	4.76E-05	230.52	1.96	122.82	0.32	98.19
128.39	3.73E-05	294.97	2.41	150.45	0.40	119.58
141.59	3.61E-05	314.85	2.61	163.02	0.42	125.13
155.66	3.50E-05	335.26	2.32	144.65	0.35	104.97
182.15	3.90E-05	343.87	3.26	204.62	0.53	156.96
213.68	3.15E-05	414.25	3.86	242.90	0.83	241.64
251.87	3.50E-05	426.79	4.26	269.18	0.74	216.41
309.41	2.78E-05	530.20	5.01	318.20	1.11	321.16
495.09	2.38E-05	725.20	6.60	425.18	1.71	492.18

model crossing the origin is fit to the data. R^2 values are higher for stiffness measurement than mass measurement, basically because the frequency shifts are higher, and therefore more easily detectable. The frequency shift detection however introduces sinusoidal ripples and stochastic disturbances varying up to 0.06 Hz. According to the linear calibration formula, the error in determining the stiffness of the cantilever beams is about 1% and 4% employing the 1st and 2nd resonance frequency shift detection respectively. It is worth mentioning that estimating the stiffness values based on linear approximations (3.35)-(3.38) may introduce up to 12% error. Therefore, employing the 2nd-order approximation the accuracy of the measurements is highly improved.

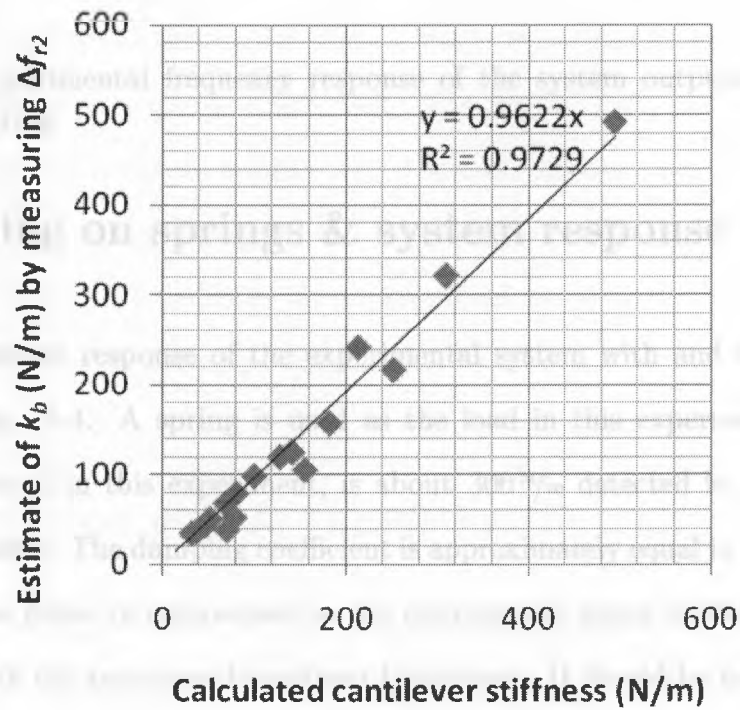
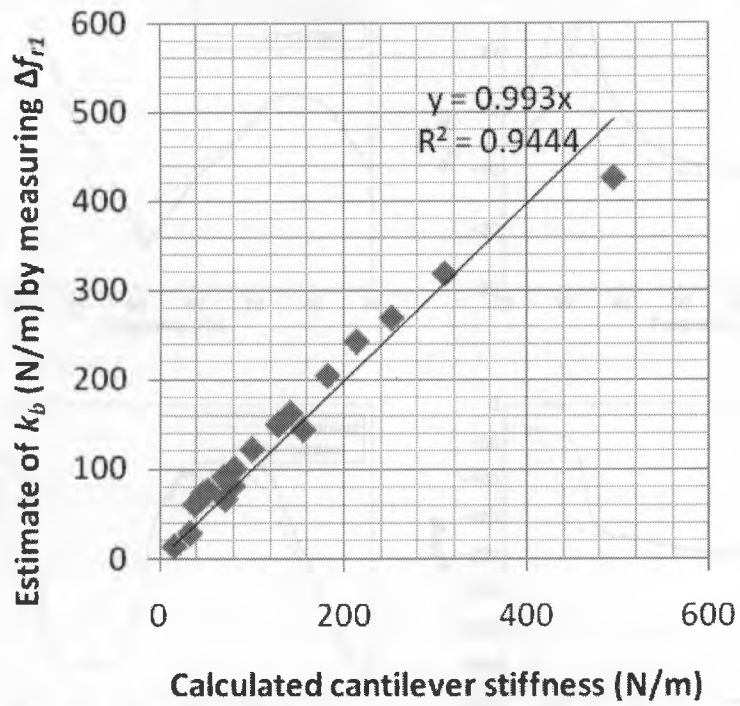


Figure 6.3: Experimental validation of stiffness measurement using cantilever beams

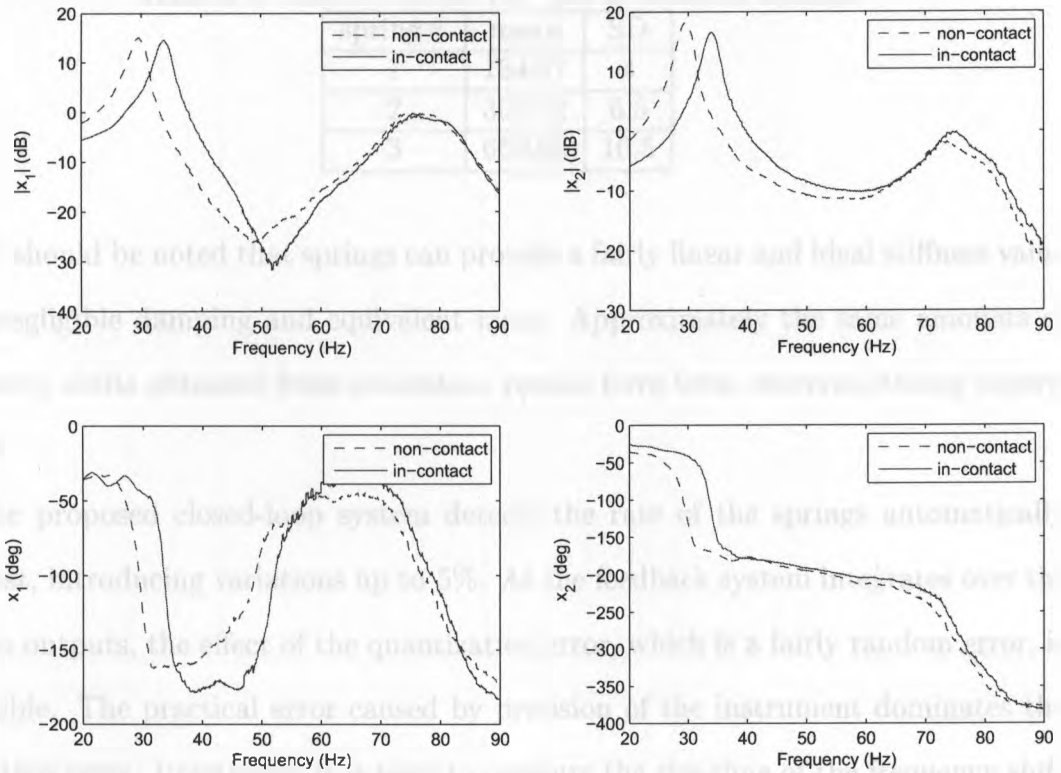


Figure 6.4: Experimental frequency response of the system outputs with/without contacting a spring

6.4 Testing on springs & system response analysis

A sample frequency response of the experimental system with and without a load is shown in Fig. 6.4. A spring is used as the load in this experiment. The rate of the spring, used in this experiment, is about 300 N/m detected by evaluating the frequency response. The damping coefficient is approximately equal to 0.01 N.s/m . The difference in the phase in comparison to the instrument's linear model is mainly due to the filtering in the system and nonlinear behaviours. It should be noted that using a PLL system, these extra behaviours are compensated as mentioned in Chapter 4.

The rate of a set of springs was measured using the proposed instrument. The mean value and Standard Deviation (SD) of the measurements are presented in Table

Table 6.3: Measured rate (in N/m) of different springs

spring#	mean	SD
1	134.97	4
2	302.72	6.5
3	659.96	10.5

6.3. It should be noted that springs can provide a fairly linear and ideal stiffness value with negligible damping and equivalent mass. Approximately the same amounts of frequency shifts obtained from simulation results have been observed during experiments.

The proposed closed-loop system detects the rate of the springs automatically and fast, introducing variations up to 5%. As the feedback system integrates over the system outputs, the effect of the quantization error, which is a fairly random error, is negligible. The practical error caused by precision of the instrument dominates the resolution error. Practically, it is hard to measure the rise time of the frequency shift output from the proposed instrument when a tissue is touched as an ideal step input command, so a new measure is introduced. The rate of Δf_r , instead, is captured when the instrument contacts a fairly stiff material. In this case, the Δf_r rate for both experimental and simulation results is approximately equal to 15 Hz/s . Based on the same rates, it is concluded that the experimental rising time of the instrument is about the same 0.15 s measured by simulation.

6.5 Testing on gels & tumor localization

Measured Δf_{r1} and $\frac{\Delta f_{3db1}}{2f_{r1}}$ for a rubber phantom with an injected tumor using PLL-based method is summarized in Table 6.4. The tumorous tissue is easily distinguishable from the rubber phantom, while the phantom is quite damped. Δf_{r1} is also measured for a gelatin-based phantom with injected tumors. A solution of gelatin and water is made to represent a soft tissue, and peas are regarded as harder tissues

Table 6.4: Measured Δf_r (in Hz) for a phantom with an injected tumor

	soft		tumorous	
$\frac{\Delta f_{3db1}}{2f_{r1}}$	~ 0.121		~ 0.075	
	mean	SD	mean	SD
Δf_{r1} (Hz)	1.13	0.02	4.82	0.06

Table 6.5: Results for different areas of the gelatin-based phantom

area	Dimensions ¹	Δf_{r1} (Hz)		
		Touching ²	~ 2 mm	~ 5 mm
0	N/A	1.08	1.28	2.42
1	$4 \times 7 \times 2.5$	1.25	2.08	3.58
2	$2 \times 6 \times 4$	0.99	2.00	2.90
3	$5.5 \times 7 \times 3$	2.23	2.78	3.57
4	$0 \times 7 \times 4$	1.40	1.55	2.77

¹In the form of $d(\text{mm}) \times D(\text{mm}) \times h(\text{mm})$ where d represents the depth of a stiffer area inside the phantom measured from the surface to the point that area is touched, D and h are the diameter and height of the area.

²The amount of pre-load deformation applied to the surface of phantom.

[102, 103]. The height of the phantom is about 9 mm. Four sample areas, shown in Fig. 6.5, are selected and the closed-loop results, shown in Table 6.5, are captured when the instrument lies in three approximate depths. Standard deviation of all values lies within 0.05 Hz. Except for area 2, it is easily possible to distinguish between the gelatin tissue and the areas with injected peas. This is mostly likely because of the presence of a gap of water between the area 2 and the surface of the gelatin phantom.

Additionally, the performance of the instrument is evaluated by moving the instrument along the rubber phantom by hand. The resonance frequency shift is shown in Fig. 6.6 noting that the ripples are following a low-frequency periodic wave which can be removed using a stronger output low-pass filter. The same result was previously summarized in Table 6.4.

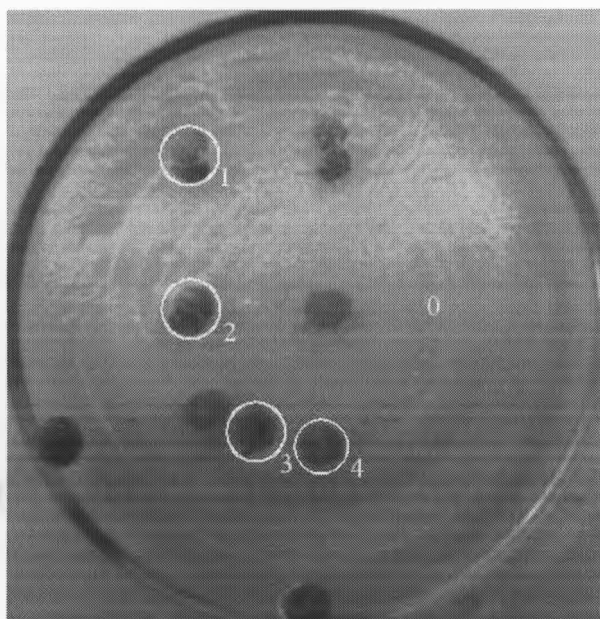


Figure 6.5: A gelatin phantom for tumor localization

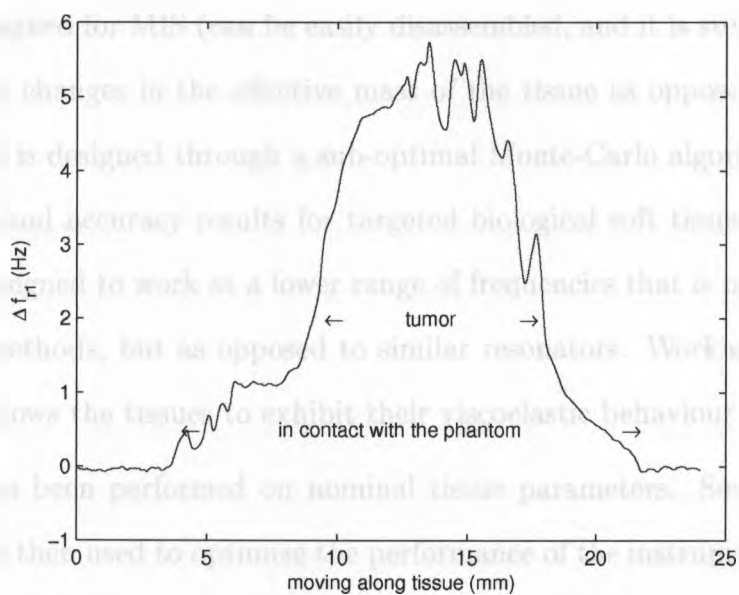


Figure 6.6: A sample experiment on a soft rubber phantom with an injected tumor

Chapter 7

Conclusion and future work

A new dynamic minimally-invasive instrument for evaluating the mechanical properties of biological soft tissues and tumor localization is proposed. The instrument is specifically designed for MIS (can be easily disassembled, and it is sterilizable), is not sensitive to the changes in the effective mass of the tissue as opposed to similar instruments, and is designed through a sub-optimal Monte-Carlo algorithm to provide high precision and accuracy results for targeted biological soft tissues. This instrument is also designed to work at a lower range of frequencies that is more common in conventional methods, but as opposed to similar resonators. Working at this range of frequency allows the tissues to exhibit their viscoelastic behaviour.

A study has been performed on nominal tissue parameters. Several conditions and criteria are then used to optimize the performance of the instrument (mainly targeting the precision and sensitivity to the measurement of tissue stiffness) employing a Monte-Carlo algorithm. Bench-top experiments and basic calculations have been also performed to ensure satisfactory mechanical design.

A PLL-Based feedback system, incorporating an extra feedback loop (comparing to common PLL systems) is employed to detect the resonance or near-resonance frequency shifts of the dynamic low-frequency instrument. This method is robust

to noise, does not require accurate displacement information, and can determine the stiffness of a soft tissue both accurately and fast enough for MIS purposes. A generalized feedback system is introduced and described. Equivalent and linearized PLL-based models are also presented that are used for design purposes based on linear control theory. Simulations are then provided for both nonlinear and linear designs and the results are compared.

Several finite-element analyses are also performed before prototyping the instrument. In these simulations, the capabilities of the proposed instrument in measuring Young's modulus of an ideal and also a practical semi-infinite material have been evaluated. Moreover, the behavior of the tissue under indentation and the frequency shifts of the instrument are investigated when a ring, which also touches the tissue, is present around the indenter. It should be noted that in the proposed instrument, the indenter oscillates while the ring is statically touching the tissue.

A novel numerical method for correlating the tissue parameters and the changes in eigenvalues of the system is also presented. This formulation can consider for an n th-order approximation. It is shown that the 2nd-order approximation improves the accuracy of the measurements up to 12%, while all other studies consider a linear correlation.

Employing the proposed method, It is shown that the instrument satisfactorily evaluates the mechanical impedance of a soft tissue modeled by a mechanical impedance. The behaviour of the instrument when touching a mechanical impedance is considered in simulation, and the equivalent stiffness, mass, and damping of the load is calculated satisfactorily. Experimentally, the evaluation of the stiffness and mass of reference masses and cantilever beam has been verified. The damping (viscosity) measurement, however, is not verified due to lack of facilities, and is thereby left to future work.

Finally, the instrument is used to localize tumors hidden inside a soft phantom, as

the stiffness values evaluated in this case are easily distinguishable. Several examples are presented in experimental results that employ the instrument held either by a stand or hand.

The possibility of the design of a similar low-frequency instrument in MEMS is going to be studied. A number of nonlinear mechanical behaviours should also be compensated that was not expected during the first prototype. The proposed instrument also opens up research topics on system identification in both time and frequency domains, stochastic and deterministic estimation and filtering, and the correlations between conventional methods on measuring mechanical properties of tissues.

- [1] V. Girosi, *Introduction to Mechanical Measurements* (Springer, New York, 2004).
- [2] OIML, *Class 1 Test Weighing Scales* (International Union of Pure and Applied Chemistry, 2003).
- [3] V. Girosi, M. P. Girosi, and G. Girosi, "Nonlinear system identification for the measurement of the elastic properties of biological tissues," *Journal of Biomechanics*, vol. 37, no. 5, pp. 511-518, 2004.
- [4] V. Girosi, M. P. Girosi, G. Girosi, H. Khatami, and F. Girosi, "Nonlinear system identification for the measurement of the elastic properties of biological tissues," *Journal of Biomechanics*, vol. 37, no. 5, pp. 511-518, 2004.
- [5] J. Girosi, M. P. Girosi, G. Girosi, F. Girosi, M. P. Girosi, F. Girosi, F. Girosi, and G. Girosi, "Nonlinear system identification for the measurement of the elastic properties of biological tissues," *Journal of Biomechanics*, vol. 37, no. 5, pp. 511-518, 2004.
- [6] D. Girosi, M. P. Girosi, G. Girosi, F. Girosi, M. P. Girosi, F. Girosi, F. Girosi, and G. Girosi, "Nonlinear system identification for the measurement of the elastic properties of biological tissues," *Journal of Biomechanics*, vol. 37, no. 5, pp. 511-518, 2004.

Bibliography

- [1] Z. Ming, Y. P. Zheng, and A. F. T. Mak, "Estimating the effective young's modulus of soft tissues from indentation tests—nonlinear finite element analysis of effects of friction and large deformation," *Medical Engineering and Physics*, vol. 19, no. 6, pp. 512–517, 1997.
- [2] Y. Fung, *Biomechanics: Mechanical Properties of Living Tissues*, 2nd ed. New York: Springer-Verlag, 1993.
- [3] WHO, "Cancer," *Fact sheets, World Health Organization*, 2004. [Online]. Available: <http://www.who.int/mediacentre/factsheets/fs297/en/index.html>
- [4] Y. Murayama, C. E. Constantinou, and S. Omata, "Micro-mechanical sensing platform for the characterization of the elastic properties of the ovum via uni-axial measurement," *Journal of Biomechanics*, vol. 37, no. 1, pp. 67–72, Jan 2004.
- [5] Y. Murayama, S. Omata, T. Yajima, Q. Peng, K. Shishido, D. M. Peehl, and C. E. Constantinou, "High resolution regional elasticity mapping of the human prostate," *Annual International Conference of the IEEE Engineering in Medicine and Biology Society*, pp. 5803–5806, 2007.
- [6] Y. Murayama, M. Haruta, Y. Hatakeyama, T. Shiina, H. Sakuma, S. Takenoshita, S. Omata, and C. E. Constantinou, "Development of a new instrument for examination of stiffness in the breast using haptic sensor technology," *Sensors and Actuators A: Physical*, vol. 143, no. 2, pp. 430 – 438, 2008.
- [7] K. Takashima, S. Horie, T. Mukai, K. Ishida, and K. Matsushige, "Piezoelectric properties of vinylidene fluoride oligomer for use in medical tactile sensor applications," *Sensors and Actuators A: Physical*, vol. 144, no. 1, pp. 90–96, 2008.

- [8] S. Omata, Y. Murayama, and C. E. Constantinou, "Real time robotic tactile sensor system for the determination of the physical properties of biomaterials," *Sensors and Actuators A: Physical*, vol. 112, no. 2-3, pp. 278–285, May 2004.
- [9] K. Hechtenberg, D. Bosch, and H. Hermeking, *Device for modeling or simulating the sense of touch in a surgical instrument*. US patents, March 1997, no. 5609607.
- [10] M. P. Ottensmeyer, A. E. Kerdok, R. D. Howe, and S. L. Dawson, *Medical Simulation*, ser. lecture notes in computer science. Springer Berlin/Heidelberg, 2004, vol. 3078, ch. The Effects of Testing Environment on the Viscoelastic Properties of Soft Tissues, pp. 9–18.
- [11] M. H. Lee and H. R. Nicholls, "Review article tactile sensing for mechatronics—a state of the art survey," *Mechatronics*, vol. 9, no. 1, pp. 1–31, 1999.
- [12] M. Vierra, M.D, "Minimally invasive surgery," *Annual Review of Medicine*, vol. 46, no. 1, pp. 147–158, 1995.
- [13] J. Dargahi, M. Parameswaran, and S. Payandeh, "A micromachined piezoelectric tactile sensor for an endoscopic grasper—theory, fabrication and experiments," *Journal of Microelectromechanical Systems*, vol. 9, no. 3, pp. 329–335, 2000.
- [14] NCBI, "National center for biotechnology information," NCBI, MeSH, Medical SubHeadings, NLM, National Library of Medicine, Tech. Rep.
- [15] A. Bicchi, G. Canepa, D. D. Rossi, P. Lacconi, and E. P. Scilingo, "A sensorized minimally invasive surgery tool for detecting tissue elastic properties," in *IEEE Int. Conf. on Robotics and Automation*, 1996, pp. 884–888.
- [16] M. P. Ottensmeyer, "Minimal invasive instrument for in vivo measurement of solid organ mechanical impedance," PhD thesis, Department of Mechanical Engineering, MIT, 2001.
- [17] M. E. H. Eltaib and J. R. Hewit, "Tactile sensing technology for minimal access surgery— a review," *Mechatronics*, vol. 13, pp. 1163–1177, 2003.
- [18] P. R. Dhar and J. W. Zu, "Design of a resonator device for in vivo measurement of regional tissue viscoelasticity," *Sensors and Actuators A: Physical*, vol. 133, no. 1, pp. 45 – 54, 2007.

- [19] T. Aoki, T. Ohashi, T. Matsumoto, and M. Sato, "The pipette aspiration applied to the local stiffness measurement of soft tissues," *Annals of Biomedical Engineering*, vol. 25, no. 3, pp. 581–587, May 1997.
- [20] E. Samur, M. Sedef, C. Basdogan, L. Avtan, and O. Duzgun, "A robotic indenter for minimally invasive measurement and characterization of soft tissue response," *Medical Image Analysis*, vol. 11, no. 4, pp. 361–373, August 2007.
- [21] J. F. Greenleaf, M. Fatermi, and M. Insana, "Selected methods for imaging elastic properties of biological tissues," *Annu. Rev. Biomed. Eng.*, vol. 5, pp. 57–58, 2003.
- [22] A. Manduca, T. E. Oliphant, M. A. Dresner, J. L. Mahowald, S. A. Kruse, E. Amromin, J. P. Felmlee, J. F. Greenleaf, and R. L. Ehman, "Magnetic resonance elastography: Non-invasive mapping of tissue elasticity," *Medical Image Analysis*, vol. 5, no. 4, pp. 237–254, 2001.
- [23] K. J. Parker and R. M. Lerner, "Sonoelasticity of organs: shear waves ring a bell," *J Ultrasound Med*, vol. 11, no. 8, pp. 387–392, 1992.
- [24] C. Sumi, "Fine elasticity imaging utilizing the iterative rf-echo phasematching method," *IEEE Transactions on Ultrasonics, Ferroelectrics and Frequency Control*, vol. 46, no. 1, pp. 158–166, Jan 1999.
- [25] C. Sumi, A. Suzuki, and K. Nakayama, "Estimation of shear modulus distribution in soft tissue from strain distribution," *IEEE Transactions on Biomedical Engineering*, vol. 42, no. 2, pp. 193–202, Feb 1995.
- [26] F. Kallel and M. Bertrand, "Tissue elasticity reconstruction using linear perturbation method," *IEEE Transactions on Medical Imaging*, vol. 15, no. 3, pp. 299–313, Jun 1996.
- [27] M. Naish, G. McCreery, A. Trejos, R. Patel, and R. Malthaner, "Effect of velocity control on kinesthetic lung tumour localization," in *Canadian Conference on Electrical and Computer Engineering*, May 2008, pp. 001 337–001 340.
- [28] A. Trejos, J. Jayender, M. Perri, M. Naish, R. Patel, and R. Malthaner, "Robot-assisted tactile sensing for minimally invasive tumor localization," *The International Journal of Robotics Research*, vol. 28, pp. 1118–1133, 2009.

- [29] —, “Experimental evaluation of robot-assisted tactile sensing for minimally invasive surgery,” in *2nd IEEE RAS and EMBS International Conference on Biomedical Robotics and Biomechatronics*, Oct 2008, pp. 971–976.
- [30] P. Puangmali, K. Althoefer, L. Seneviratne, D. Murphy, and P. Dasgupta, “State-of-the-art in force and tactile sensing for minimally invasive surgery,” *Sensors Journal, IEEE*, vol. 8, no. 4, pp. 371–381, April 2008.
- [31] L. D. Harmon, “Automated tactile sensing,” *Int. J. of Robotics Research*, vol. 1, no. 2, pp. 3–32, 1982.
- [32] J. L. Leveque, G. G. Montfermeil, and J. S. Aulney-Sous-Bois, *Apparatus for measuring the consistency or harness of a material*. US patents, Jul 1979, no. 4159640.
- [33] J. Dargahi, “A piezoelectric tactile sensor with three sensing elements for robotic, endoscopic and prosthetic applications,” *Sensors and Actuators A: Physical*, vol. 80, no. 1, pp. 23 – 30, 2000.
- [34] J. N. Zemel and P. Jenkintown, *Impedance tomographic tactile sensor*. US patents, Dec 1990, no. 4980646.
- [35] S. Omata and Y. Terunuma, “New tactile sensor like the human hand and its applications,” *Sensors and Actuators A: Physical*, vol. 35, no. 1, pp. 9–15, October 1992.
- [36] E. Scilingo, D. De Rossi, A. Bicchi, and P. Iacconi, “Sensors and devices to enhance the performances of a minimally invasive surgery tool for replicating surgeon’s haptic perception of the manipulated tissues,” in *19th Annual International IEEE Conference on Engineering in Medicine and Biology Society*, vol. 3, Oct/Nov 1997, pp. 961–9643.
- [37] T. Hu, A. E. Castellanos, G. Tholey, and J. P. Desai, “In-vivo and in-situ compressive properties of porcine abdominal soft tissues,” *Medical Image Computing and Computer-Assisted Intervention (MICCAI)*, vol. 2488, pp. 66–74, 2002.
- [38] D. T. V. Pawluk, J. S. Son, P. S. Wellman, W. J. Peine, and R. D. Howe, “A distributed pressure sensor for biomechanical measurements,” *Journal of Biomechanical Engineering*, vol. 120, no. 2, pp. 302–305, 1998.

- [39] J. Rosen, B. Hannaford, M. MacFarlane, and M. Sinanan, "Force controlled and teleoperated endoscopic grasper for minimally invasive surgery-experimental performance evaluation," *IEEE Transactions on Biomedical Engineering*, vol. 46, no. 10, pp. 1212–1221, Oct 1999.
- [40] V. Munoz, C. Vara-Thorbeck, J. DeGabriel, J. Lozano, E. Sanchez-Badajoz, A. Garcia-Cerezo, R. Toscano, and A. Jimenez-Garrido, "A medical robotic assistant for minimally invasive surgery," in *IEEE International Conference on Robotics and Automation*, vol. 3, 2000, pp. 2901–2906.
- [41] R. Taylor, J. Funda, B. Eldridge, S. Gomory, K. Gruben, D. LaRose, M. Talamini, L. Kavoussi, and J. Anderson, "A telerobotic assistant for laparoscopic surgery," *Engineering in Medicine and Biology Magazine, IEEE*, vol. 14, no. 3, pp. 279–288, May/June 1995.
- [42] G. Tholey, A. Pillarisettei, and J. P. Desai, "On-site three dimensional force sensing capability in a laparoscopic grasper," *The International Journal of Industrial Robot*, vol. 31, pp. 509–518, 2004.
- [43] G. Tholey, J. P. Desai, and A. E. Castellanos, "Force feedback plays a significant role in minimally invasive surgery: Results and analysis," *Annals of Surgery*, vol. 241, pp. 102–109, 2005.
- [44] G. Tholey and J. P. Desai, "A modular, automated laparoscopic grasper with three-dimensional force measurement capability," in *IEEE International Conference on Robotics and Automation*, 2007, pp. 250–255.
- [45] S. K. Prasad, M. Kitagawa, G. S. Fischer, M. A. Talamini, and R. H. Taylor, "A modular 2-dof force-sensing instrument for laparoscopic surgery," in *Medical Image Computing and Computer-Assisted Intervention*, 2003, pp. 279–286.
- [46] S. Schostek, C.-N. Ho, D. Kalanovic, and M. O. Schurr, "Artificial tactile sensing in minimally invasive surgery - a new technical approach," *Minimally Invasive Therapy and Allied Technologies*, vol. 15, pp. 296–304, 2006.
- [47] S. Sokhanvar, M. Packirisamy, and J. Dargahi, "A multifunctional pvdf-based tactile sensor for minimally invasive surgery," *Smart Materials and Structures*, vol. 16, pp. 989–998, 2007.
- [48] S. Najarian, J. Dargahi, and X. Z. Zheng, "A novel method in measuring the stiffness of sensed objects with applications for biomedical robotic systems,"

- The International Journal of Medical Robotics and Computer Assisted Surgery*, vol. 2, pp. 84–90, 2006.
- [49] Kattavenos, N., Lawrenson, B., Frank, T.G., M. Pridham, R. Keatch, and A. Cuschieri, “Force sensitive tactile sensor for minimal access surgery,” *Minimally Invasive Therapy and Allied Technologies*, vol. 13, no. 1, pp. 42–46, 2004.
- [50] J. D. Brown, J. Rosen, M. Moreyra, M. Sinanan, and B. Hannaford, “Computer-controlled motorized endoscopic grasper for in vivo measurement of soft tissue biomechanical characteristic,” *Studies in Health Technology and Informatics*, vol. 85, pp. 71–73, 2002.
- [51] D. Kalanovic, M. P. Ottensmeyer, J. Groß, and S. L. Dawson, “Independent testing of soft tissue visco-elasticity using indentation and rotary shear deformations,” in *11th Annual Medicine Meets Virtual Reality Conference*, 2003.
- [52] F. J. Carter, T. G. Frank, P. J. Davies, D. McLean, and A. Cuschieri, “Measurements and modelling of the compliance of human and porcine organs,” *Medical Image Analysis*, vol. 5, no. 4, pp. 231–236, Dec 2001.
- [53] M. Vidic, S. M. Harb, and S. T. Smith, “Observations of contact measurements using a resonance-based touch sensor,” *Precision Engineering*, vol. 22, no. 1, pp. 19 – 36, 1998.
- [54] M. H. Araghi and S. P. Salisbury, “A feedback-based dynamic instrument for measuring mechanical properties of soft tissues for minimally-invasive surgery,” in *International workshop on smart materials and structures*, Montreal, Canada, Oct 2009.
- [55] T. Kanda, T. Morita, M. K. Kurosawa, and T. Higuchi, “A flat type touch probe sensor using pzt thin film vibrator,” *Sensors and Actuators A: Physical*, vol. 83, no. 1-3, pp. 67–75, 2000.
- [56] S. Muraoka, “Application of a quartz resonator to a force sensor built in a robot finger for use in a grasp or recognition environment,” *Measurement*, vol. 34, no. 3, pp. 229 – 244, 2003.
- [57] C. Barthod, Y. Teisseyre, C. Géhin, and G. Gautier, “Resonant force sensor using a pll electronic,” *Sensors and Actuators A: Physical*, vol. 104, no. 2, pp. 143 – 150, 2003.

- [58] S. M. Harb and M. Vidic, "Resonator-based touch-sensitive probe," *Sensors and Actuators A: Physical*, vol. 50, pp. 23–29, 1995.
- [59] D. Valtorta and E. Mazza, "Measurement of rheological properties of soft biological tissue with a novel torsional resonator device," *Rheologica Acta*, vol. 45, no. 5, pp. 677–692, 2006.
- [60] V. Jalkanen, "Tactile sensing of prostate cancer -a resonance sensor method evaluated using human prostate tissue in vitro," Ph.D. dissertation, Department of Applied Physics and Electronics, Centre for Biomedical Engineering and Physics, Umeå University, 2007.
- [61] A. E. Kerdok, M. P. Ottensmeyer, and R. D. Howe, "Effects of perfusion on the viscoelastic characteristics of liver," *Journal of Biomechanics*, vol. 39, no. 12, pp. 2221 – 2231, 2006.
- [62] T. Ohashi, H. Abe, T. Matsumoto, and M. Sato, "Pipette aspiration technique for the measurement of nonlinear and anisotropic mechanical properties of blood vessel walls under biaxial stretch," *Journal of Biomechanics*, vol. 38, no. 11, pp. 2248–2256, Nov 2005.
- [63] T. Boudou, J. Ohayon, Y. Arntz, G. Finet, C. Picart, and P. Tracqui, "An extended modeling of the micropipette aspiration experiment for the characterization of the young's modulus and poisson's ratio of adherent thin biological samples: Numerical and experimental studies," *Journal of Biomechanics*, vol. 39, no. 9, pp. 1677–1685, 2006.
- [64] M. Kauer, "Inverse finite element characterization of soft tissues with aspiration experiments," Ph.D. dissertation, Institute of Mechanical Systems, Diss No: 14233, ETH, Zurich, 2001.
- [65] K. Miller, K. Chinzei, G. Orssengo, and P. Bednarz, "Mechanical properties of brain tissue in-vivo: experiment and computer simulation," *Journal of biomechanics*, vol. 33, no. 11, pp. 1369–1376, Nov 2000.
- [66] S. Kassner, J. Rausch, A. Kohlstedt, and R. Werthschützky, *Analysis of mechanical properties of liver tissue as a design criterion for the development of a haptic laparoscopic tool*, 2009, pp. 2248–2251.

- [67] A. Sarvazyan, M. E. Schafer, and V. Ponomarev, *Method and device for measuring anisotropic mechanical properties of tissue*. US Patents, Jan 1998, no. 5706815.
- [68] O. A. Lindahl, C. E. Constantinou, A. Eklund, Y. Murayama, P. Hallberg, and S. Omata, "Tactile resonance sensors in medicine," *Journal of medical engineering and technology*, vol. 33, no. 4, pp. 263–273, 2009.
- [69] R. S. Lakes, *Viscoelastic solids*. CRC Press LLC, 1999.
- [70] P. Michaels, "Water, inertial damping, and the complex shear modulus," *Geotechnical earthquake Engineering and Soil Dynamics IV*, pp. 1–10, 2008.
- [71] T. Ohtsuka, A. Furuse, T. Kohno, J. Nakajima, K. Yagyu, and S. Omata, "Application of a new tactile sensor to thoracoscopic surgery: Experimental and clinical study," *Ann Thorac Surg*, vol. 60, no. 3, pp. 610–613, 1995.
- [72] Y. Hasegawa, M. Shikida, H. Sasaki, K. Itoigawa, and K. Sato, "An active tactile sensor for detecting mechanical characteristics of contacted objects," *Journal of Micromechanics and Microengineering*, vol. 16, no. 8, pp. 1625–1632, Aug 2006.
- [73] S. Matsumoto, R. Ooshima, K. Kobayashi, N. Kawabe, T. Shiraishi, Y. Mizuno, H. Suzuki, and S. Umemoto, "A tactile sensor for laparoscopic cholecystectomy," *Surgical Endoscopy*, vol. 11, no. 9, pp. 939–941, 1997.
- [74] J. Wang, B. Teng, and Y. Yu, "The firmness detection by excitation dynamic characteristics for peach," *Food Control*, vol. 17, no. 5, pp. 353–358, 2006.
- [75] Y. Murayama, C. E. Constantinou, and S. Omata, "Remote sensing of mechanical properties of materials using a novel ultrasound transducer and signal processing," *IEEE transactions on ultrasonics, ferroelectrics, and frequency control*, vol. 52, no. 3, pp. 439–444, Mar 2005.
- [76] S. Omata, Y. Murayama, and C. E. Constantinou, "Multi-sensory surgical support system incorporating, tactile, visual and auditory perception modalities," *Studies in health technology and informatics*, vol. 111, pp. 369–371, 2005.
- [77] —, "Development of a novel surgical support instrument and virtual system incorporating new tactile sensor technology," *Studies in health technology and informatics*, vol. 98, pp. 288–290, 2004.

- [78] Y. Murayama and S. Omata, "Considerations in the design and sensitivity optimization of the micro tactile sensor," *IEEE transactions on ultrasonics, ferroelectrics, and frequency control*, vol. 52, no. 3, pp. 434–438, Mar 2005.
- [79] D. Valtorta and E. Mazza, "Dynamic measurement of soft tissue viscoelastic properties with a torsional resonator device," *Medical Image Analysis*, vol. 9, no. 5, pp. 481–490, Oct 2005.
- [80] A. M. Dollar and R. D. Howe, "A robust compliant grasper via shape deposition manufacturing," *IEEE/ASME Transactions on Mechatronics*, vol. 11, no. 2, Apr 2006.
- [81] F. M. Gardner, *Phaselock techniques*, 3rd ed. Hoboken, New Jersey: John Wiley & Sons, Inc., 2005.
- [82] J. D. Brown, J. Rosen, Y. S. Kim, L. Chang, M. N. Sinanan, and B. Hannaford, "In-vivo and in-situ compressive properties of porcine abdominal soft tissues," *Medicine Meets Virtual Reality*, vol. 94, pp. 26–32, 2003.
- [83] A. Arnau, *Piezoelectric Transducers and Applications*, 2nd ed. Springer, 2004.
- [84] D. Klatt, U. Hamhaber, P. Asbach, J. Braun, and I. Sack, "Noninvasive assessment of the rheological behavior of human organs using multifrequency mr elastography: a study of brain and liver viscoelasticity," *Physics in Medicine and Biology*, vol. 52, no. 24, pp. 7281–7294, 2007.
- [85] K. Ogata, *Discrete-Time Control Systems*, 2nd ed. Prentice-hall International Edition, 1995.
- [86] S. S. Rao, *Mechanical Vibrations*, 4th ed. Prentice Hall, 2003.
- [87] M. Ottermo, O. Stavdahl, and T. Johansen, "Palpation instrument for augmented minimally invasive surgery," in *IEEE/RSJ International Conference on Intelligent Robots and Systems*, vol. 4, Sep 2004, pp. 3960–3964.
- [88] M. V. Ottermo, M. Øvstedal, T. Langø, y. Stavdahl, Y. Yavuz, T. A. Johansen, and R. Mårvik, "The role of tactile feedback in laparoscopic surgery," *Surgical Laparoscopy, Endoscopy and Percutaneous Techniques*, vol. 16, pp. 390–400, 2006.

- [89] B. M. Ahn, "Characterization of viscoelastic properties of intra-abdominal organs from in vitro indentation experiments and inverse finite element parameter optimization," Master's thesis, School of Mechanical, Aerospace & Systems Engineering, Department of Mechanical Engineering, Korea Advanced Institute of Science and Technology, 2007.
- [90] B. K. Tay, J. Kim, and M. A. Srinivasan, "In vivo mechanical behavior of intra-abdominal organs," *IEEE Trans. on Biomed. Eng.*, vol. 53, no. 11, pp. 2129–2138, 2006.
- [91] P. S. Wellman, R. D. Howe, E. Dalton, and K. A. Kern, "Breast tissue stiffness in compression is correlated to historical diagnosis," Harvard University, Tech. Rep., 1999.
- [92] A. P. Sarvazyan, A. R. Akovoroda, S. Y. Emelianov, J. B. Fowlkes, J. G. Pipe, R. S. Adler, R. B. Buston, and P. L. Carson, "Biophysics bases of elasticity imaging," *acoustical imaging*, vol. 21, 1995.
- [93] T. Cook, H. Alexander, and M. L. Cohen, "Experimental method for determining the 2-dimensional mechanical properties of living human skin," *Med. Biol. Eng. Comput.*, pp. 381–390, 1977.
- [94] R. N. Stiles, "Frequency and displacement amplitude relations for normal hand tremor," *J appl Physiol*, vol. 40, no. 1, pp. 44–54, 1976.
- [95] A. Samani and D. Plewes, "An inverse problem solution for measuring the elastic modulus of intact ex vivo breast tissue tumours," *Physics in Medicine and Biology*, vol. 52, no. 5, p. 1247, 2007.
- [96] R. E. Best, *Phase-locked loops: design, simulation, and applications*. McGraw-Hill, 2007.
- [97] J. A. Crawford, *Advanced phase-lock techniques*. Artech house, 2008.
- [98] W. C. Hayes, L. M. Keer, G. Herrmann, and L. F. Mockros, "A mathematical analysis for indentation tests of articular cartilage," *J Biomech.*, vol. 5, no. 5, pp. 541–551, Sep 1972.
- [99] A. C. Fischer-Cripps, *Introduction to Contact Mechanics*, 2nd ed. Springer-Verlag, 2007.

- [100] J. P. Wolf, "Spring-dashpot-mass models for foundation vibrations," *Earthquake Engineering and Structural Dynamics*, vol. 26, no. 9, pp. 931–949, 1997.
- [101] T. Irvin, *Application of the Newton-Raphson Method to Vibration Problems*. Vibrationdata Publications, 1999.
- [102] G. A. Sisney and K. A. Hunt, "A low-cost gelatin phantom for learning sonographically guided interventional breast radiology techniques," American Roentgen Ray Society, technical report, jan 1998.
- [103] D. Sorbi, E. Vazquez-Sequeiros, and M. J. Wiersema, "A simple phantom for learning eus-guided fna," *Gastrointestinal Endoscopy*, vol. 57, no. 4, pp. 580–583, 2003.